UNIVERSITY of OULU
OULUN YLIOPISTO

X-RAYING COMPACT STARS

IN THE GALAXY AND BEYOND

JARI J.E. KAJAVA

REPORT SERIES IN PHYSICAL SCIENCES
Report No. 79 (2012)

X-RAYING COMPACT STARS

IN THE GALAXY AND BEYOND

JARI J.E. KAJAVA

Astronomy Division
Department of Physics
University of Oulu
Finland

Academic dissertation to be presented with the assent of the Doctoral Training Committee of Technology and Natural Sciences of the University of Oulu for public defence in the Auditorium Anttilansali, Linnanmaa, on December 14, 2012, at 12 o'clock noon.

REPORT SERIES IN PHYSICAL SCIENCES Report No. 79

OULU 2012 ● UNIVERSITY OF OULU

Supervisor
Prof. Juri Poutanen, University of Oulu, Oulu, Finland

Opponent
Prof. Chris Done, Durham University, Durham, UK

Reviewers
Dr. Tod Strohmayer, NASA/GSFC, Greenbelt, MD, USA
Dr. Didier Barret, IRAP, Toulouse, France

Custos
Prof. Juri Poutanen, University of Oulu, Oulu, Finland

ISBN 978-952-62-0027-9
ISBN 978-952-62-0028-6 (PDF)
ISSN 1239-4327

JUVENES PRINT
Oulu 2012

Abstract

This thesis focuses on observational study of a variety of phenomena that occur in the vicinity of two types of compact stars: neutron stars (NS) and black holes (BH). These two compact star types are characterized by their enormous densities. The densities in NS cores exceed the normal nuclear density in heavy atomic nuclei. Therefore, by studying neutron stars, we can infer what happens to atomic nuclei when they are compressed. BHs are the densest stars in the universe: in fact, they are so dense that even light cannot escape from their surfaces. The entire mass of a BH is concentrated into an infinitely dense point called a singularity, which is shrouded from view by the event horizon.

NSs and BHs display a large variety of observational phenomena when they are members in interactive binary star systems. In these binary systems, the compact star accretes matter from a companion star and a fraction of the available gravitational potential energy of the in-falling gas is converted into X-ray light. In this thesis, I have studied two different types of compact star systems using data from satellite instruments that can detect these X-rays. I have studied a class of accreting NSs called Accreting Millisecond Pulsars (AMP) and luminous extragalactic systems called Ultra-Luminous X-ray sources (ULX) that are thought to be powered by accretion onto BHs. In this thesis, I will demonstrate how we can infer physical properties of compact stars through X-ray spectroscopy and timing analysis, and I will also show how we have applied these methods to study the properties of AMPs and ULXs.

The results we have obtained improve our understanding of these systems. We have discovered that spectra of AMPs vary strongly below the energy band that is commonly used to study these sources. We also found that this new phenomenon in AMPs is related to variations in the observed pulse shapes, which in our interpretation shows that the accretion disc–magnetosphere interaction region in AMPs is highly dynamic. In future studies, this finding will help us to utilize AMP pulsations to constrain NS masses and radii more accurately than before. We have also obtained evidence that the majority of ULXs are not powered by accretion onto intermediate-mass BHs, which had been suggested by numerous previous studies. Our analysis instead supports the view that the extreme luminosities of a majority of ULXs are a result of very high mass accretion rate onto “typical” BHs having no more than a few tens of solar masses.

Acknowledgements

The work presented in this PhD thesis was carried out between 2008–2012 in the high energy astrophysics group at the Department of Physics of the University of Oulu. I would first like to thank my supervisor Prof. Juri Poutanen for giving me the opportunity to work in his group and his guidance during these years.

I acknowledge the Finnish Graduate School in Astronomy and Space Physics for funding during 2008–2011. I also acknowledge the Emil Aaltonen Foundation (Emil Aaltosen Säätiö) for funding during the year 2012. In addition, I would like to thank the Department of Physics, especially the head of the department, Prof. Matti Weckström, for the generous motivational stipend awarded in 2012.

I would also like to thank Tod Strohmayer from NASA/GSFC and Didier Barret from IRAP, Toulouse, for their careful pre-examination of this thesis and for their valuable comments.

I had the pleasure of collaborating with several people during my PhD. I would like to first thank two of my fellow PhD students and co-authors, Askar Ibragimov and Marja Annala, for their help and friendship, but I am also equally grateful to have had the opportunity to work with Sean Farrell, Phil Kaaret, Alessandro Patruno, Fabien Grisé and Hua Feng during these years. Without your help the process of completing this thesis would not have been so pleasurable.

I also warmly thank the other (current and past) members of the high energy astrophysics group: Andrew Gosling, Vitaly Neustroev, Indrek Vurm, Alexey Medvedev, Sergey Tsygankov, Alexandra Veledina, Tuulia Pennanen, Alexander Mushtukov, Outi-Marja Latvala and Joonas Nättilä, for creating a nice working environment in the group. Also, I want to thank Pertti Rautiainen for his help and for his witty jokes that gave me good laughs on a weekly basis. In addition, I would like to thank Mike Revnivtsev and Marat Gilfanov for their hospitality during my short, but highly productive visit to Garching.

I am glad for the support from my friends, especially from the lunch time company, for the refreshing midday break that gave the energy to muddle through the rest of the day. Also, I want to thank my family for all the help, support and encouragement you have given me. Finally I would like to give my

deepest gratitude to my wife, Junkal, for standing by me throughout this long process and for reminding me every day what is truly important in life.

List of original papers

The present thesis contains an introductory part and five papers, which will be referred in the text by their Roman numbers:

I. Ibragimov A., Kajava J. J. E. and Poutanen J. (2011), "The 2009 outburst of accreting millisecond pulsar IGR J17511–3057 as observed by *Swift* and *RXTE*," MNRAS, 415, 1864

II. Kajava J. J. E., Ibragimov A., Annala M., Patruno A. and Poutanen J. (2011), "Varying disc-magnetosphere coupling as the origin of pulse profile variability in SAX J1808.4–3658," MNRAS, 417, 1454

III. Kajava J. J. E. and Poutanen J. (2009), "Spectral variability of ultraluminous X-ray sources," MNRAS, 398, 1450

IV. Grisé F., Kaaret P., Feng H., Kajava J. J. E. and Farrell S. A. (2010), "X-ray spectral state is not correlated with luminosity in Holmberg II X-1," ApJ, 724, 148L

V. Kajava J. J. E., Poutanen J., Farrell S. A., Grisé F. and Kaaret P. (2012), "Evolution of the spectral curvature in the ULX Holmberg II X-1," MNRAS, 422, 990

Author contributions

In Paper I, I reduced the *Swift*/XRT data and helped with the data analysis and modelling. I also contributed significantly in the preparation of the manuscript. A. Ibragimov performed the modelling, data analysis and wrote the manuscript. J. Poutanen provided help with the interpretation of the results and participated in the preparation of the manuscript before submission to MNRAS.

In Paper II, I reduced the *Swift*/XRT data, performed all the data analysis, did all the modelling and wrote the manuscript. I also provided the physical interpretation of the results. A. Ibragimov provided the *RXTE* spectral- and

timing data, and pulse profiles. M. Annala provided help with the pulse profile modelling and made graphical illustrations. The idea to look into the dataset came from A. Patruno. The code to model the pulse profiles was provided by J. Poutanen; I modified the code to allow simultaneous fitting of arbitrary number of pulse profiles and I also added other small functionalities that was needed for the project. Everyone participated in improving and commenting on the manuscript before submission to MNRAS.

In Paper III, I performed all the data analysis and wrote the manuscript. The idea for the project came from J. Poutanen, who also provided close supervision in the preparation of the manuscript (as this was the first manuscript I submitted).

In Paper IV, P. Kaaret and H. Feng designed the study and were the proposers of the project which included the writing of the proposal to get *Swift* observing time. F. Grisé reduced and analysed the Swift data. S. Farrell and I were mainly involved in the interpretation of the results. Everyone provided comments and insights on the manuscript before submitting it to ApJL.

In Paper V, S. Farrell and I wrote the *XMM-Newton* observation proposal that was triggered as target of opportunity observation. After obtaining the *XMM-Newton* data, I performed all the data analysis and wrote the manuscript. Everyone participated in the interpretation and discussion of the results, and provided improvements to the manuscript before submitting it to MNRAS.

Contents

1 Introduction to compact stars **1**
1.1 Neutron stars as probes of ultra-dense matter 1
1.2 Mass range of black holes 3
1.3 Compact stars as sources of X-ray radiation 6
1.4 Aim and scope of the thesis 7

2 X-ray observatories **9**
2.1 Rossi X-ray Timing Explorer 10
2.1.1 Proportional Counter Array (PCA) 10
2.1.2 High Energy X-ray Timing Experiment (HEXTE) 12
2.2 Chandra 14
2.2.1 Focusing optics and Charged Coupled Devices in X-ray astronomy 15
2.2.2 Advanced CCD Imaging Spectrometer (ACIS) 17
2.3 XMM-Newton 18
2.3.1 EPIC-pn 19
2.3.2 EPIC mos-1 and EPIC mos-2 20
2.4 Swift 20
2.5 X-ray spectroscopy and spectral modelling 22

3 Accreting millisecond pulsars **25**
3.1 Discovery of accreting millisecond pulsars 25
3.2 Origin of pulsations 26
3.3 Energy spectra of AMPs 30
3.4 Timing noise in AMPs 31
3.5 Neutron star masses and radii from AMP pulse profiles 35
3.6 Discovery of simultaneous spectral and pulse profile transition 37
3.7 Discussion 44

4 Ultraluminous X-ray sources **51**
4.1 Nature of ULXs: is black hole mass the key factor? 51
4.2 Optical observations of the ULX population 55
4.2.1 Optical counterparts of ULXs 55
4.2.2 Emission line nebulae around ULX 56
4.2.3 Population studies link ULXs to star formation 57
4.3 X-ray mass scaling methods for ULXs 59
4.3.1 Mass scaling from ULX timing analysis 59

4.3.2 Mass scaling from spectral properties 60
4.4 Results 64
4.4.1 Spectral variability of ULXs 64
4.4.2 Spectral variability in the ULX Holmberg II X-1 68
4.5 Discussion 71

5 Summary and future prospects **75**
5.1 Summary and future prospects 75

Chapter 1

Introduction to compact stars

The research field of compact stars was born from the grand discoveries and advances that were made in the 1930's. That decade saw the discovery of neutrons (Chadwick, 1932), the emergence of the first ideas of stars consisting of neutrons (Baade & Zwicky, 1934), and computations of maximum masses of white dwarfs (WD; Chandrasekhar 1931, 1935) and neutron stars (NS; Tolman 1939; Oppenheimer & Volkoff 1939). Because these two compact star types were found to have maximum masses,[1] a debate started over the existence of the third compact star type: the black hole (BH), the most massive and the most exotic of all compact stars. Our research goals can be traced back to the first paper that (correctly) describes the formation of neutron stars (Baade & Zwicky, 1934):

> "With all reserve we advance the view that a super-nova represents the transition of an ordinary star into a neutron star, consisting mainly of neutrons. Such a star may possess a very small radius and an extremely high density."

These two sentences are highly relevant in modern astronomy, as we are still attempting to determine the densities and the composition of neutron stars by accurately measuring their masses and radii.

1.1 Neutron stars as probes of ultra-dense matter

The reason why astronomers want to measure NS masses and radii can be illustrated with the following argument. We can infer the (mean) densities of

[1] Note that the initial maximum NS mass was incorrectly estimated to be ~ 0.7 solar masses. Modern NS models predict maximum masses of ~ 2.5 solar masses, while the heaviest known NS has a mass of ≈ 2 solar masses (Demorest et al., 2010).

stars (assuming they are spherical) by measuring their masses M and radii R through

$$\bar{\rho} = 3M/(4\pi R^3). \tag{1.1}$$

The reason why we still do not know NS densities is that it is tremendously difficult to measure their masses and radii accurately.[2] We do, however, know the order of magnitude of NS masses and radii. Using these so called "canonical" NS parameters, mass $M_{\rm ns} \sim 1.4\,{\rm M}_\odot$ (${\rm M}_\odot \approx 2\times10^{33}$ g is the solar mass) and radius $R_{\rm ns} \sim 10$ km, we find that the mean density of a typical NS is

$$\bar{\rho}_{\rm ns} \sim 7 \times 10^{14}\,{\rm g\,cm^{-3}} \sim (2-3)\rho_0, \tag{1.2}$$

where $\rho_0 \approx 2.8\times10^{14}\,{\rm g\,cm^{-3}}$ is the normal nuclear density, i.e. the mass density of heavy atomic nuclei (Haensel et al., 2007). This means that, on average, the NS matter is denser than nucleons. This is why we can infer what happens to matter when it is compressed to supra-nuclear densities through measurements of NS masses and radii. I must emphasise that these densities are very difficult to produce in laboratories; only very recently heavy ion collision experiments have been performed that probe dense matter physics (see Lattimer & Prakash 2007, for review). Therefore, this open fundamental question of physics must be answered by astronomers.

In reality, stars are never uniform and Equation (1.1) is in fact a very poor description of the radial density profile within the star. We know that the density must increase towards the core of the star, where the conditions are so extreme ($\rho \gtrsim \rho_0$) that the theory (quantum chromodynamics) cannot be applied to describe the structure of the star (Haensel et al., 2007). This makes the density computations very challenging, and to tackle this issue, theorists have developed several NS equation of state (EOS) models that describe what happens to matter in these conditions (e.g. Lattimer & Prakash 2001, 2007). All these NS EOS models predict how pressure P depends on density ρ and temperature T within the star and, in addition, some EOS models predict the emergence of exotic particles in the cores of NSs. Therefore, the word EOS also refers to the composition of NS matter. Once the NS EOS is specified, a NS model can be computed.

Because different NS EOS models predict different mass-radius (M–R) relationships (see Figure 1.1), these models allow us to make comparisons between observational data and theoretical predictions. The problem is that one needs to measure both mass and radius to an accuracy of about a few per cent in order to distinguish the correct model. Such accuracy has not been achieved yet, although the massive NS found by Demorest et al. (2010) excludes some EOSs

[2]Note that NS masses can be measured very accurately from observations of radio-pulsars (e.g. Demorest et al. 2010), but the NS radii cannot be determined because the radio emission does not come from the NS surface.

already (see Figure 1.1). This is why the problem remains unresolved and why Haensel et al. (2007) writes:

> "The fundamental problem of the EOS of superdense matter constitutes the main mystery of neutron stars."

In this thesis, I will present our results that aim to solve this mystery: we have studied an observational class of NSs called accreting millisecond pulsars (AMP), for which NS masses and radii can be measured simultaneously.

Once we have achieved the goal of determining the correct NS model, we can infer the maximum masses of NSs from the models. If the mass exceeds this maximum value, the star collapses onto itself. This would create the ultimate type of compact star; a star so dense that even light cannot escape its gravitational pull. This is why John Wheeler invented the name "black hole" to describe such stars. Therefore, by obtaining the correct NS model we have an additional "bonus"; we do not only find the maximum masses of NSs, but we can also infer the minimum masses of stellar black holes.

1.2 Mass range of black holes

Black holes (BH) are thought to be extremely simple objects. The "no hair conjecture" states that the properties of a BH are determined only by three parameters; its mass, its spin (the amount of angular momentum it contains) and its charge (Misner et al., 1973). In an astrophysical context, however, the charge of a BH is not relevant, because if such BH is formed it would immediately accrete oppositely charged particles to reach charge neutrality. So, in order to characterise the properties of a BH observationally, we need only to measure its mass and its radius (which allow to compute its spin). However, in reality this task is also very difficult, because it is challenging to measure the radius of something that does not emit light.

We know from Einstein's formulation of gravity (general relativity) how the radius of a BH can be computed if we know the mass and the spin of the BH. Already in 1915 Karl Schwarzschild found the first such solution for Einstein's field equations for a non-spinning BH. His result was that the event horizon (the mathematical surface where light can still escape the gravitational pull of the BH) is located at the Schwarzschild radius

$$R_{\rm s} = 2GM_{\rm bh}/c^2 \approx 2.95\, M/{\rm M}_\odot\,{\rm km}, \tag{1.3}$$

where $G \approx 6.67\times10^{-8}\,{\rm cm^3\,g^{-1}\,s^{-2}}$ is the gravitational constant, $M_{\rm bh}$ is the mass of the BH and $c = 2.99792458\times10^{10}\,{\rm cm\,s^{-1}}$ is the speed of light in vacuum. This type of non-spinning Schwarzschild BH is therefore an extremely simple star

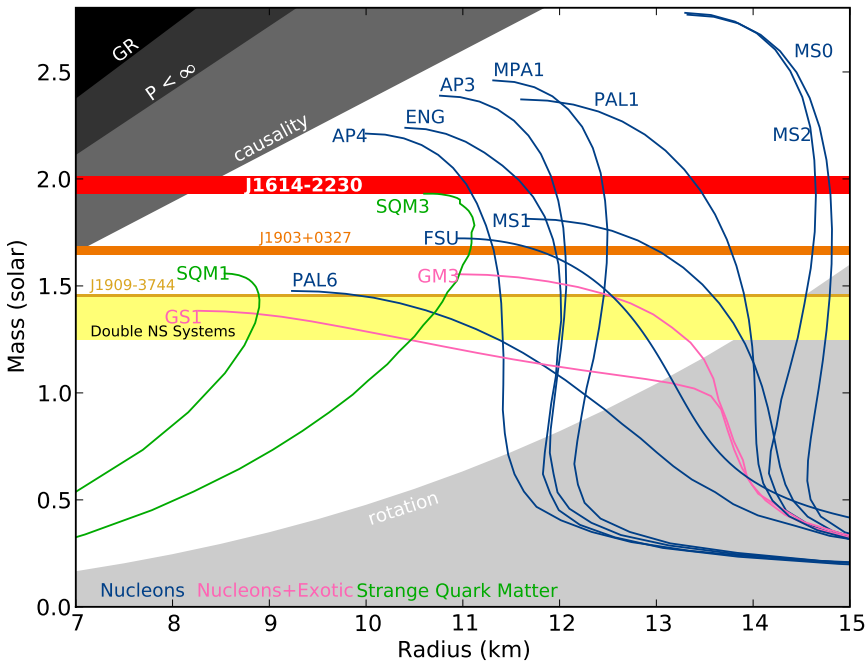

Figure 1.1. Neutron star mass-radius diagram, showing the different model predictions for various EOSs (see Lattimer & Prakash 2001). The top horizontal band shows the mass measurement constraint from Demorest et al. (2010) $M_{\rm ns} = 1.97 \pm 0.04\,{\rm M}_{\odot}$ and the bottom band shows the range of observed NS masses from NS binaries (Lattimer & Prakash, 2007). Although the discovery of the massive NS by Demorest et al. (2010) excludes the EOS that predict the formation of kaon condensates or hyperons (marked as "nucleons+exotic") and even NS EOS with "strange quark matter" composition in the NS core (see Haensel et al. 2007; Lattimer & Prakash 2007), the correct NS model cannot be determined from these observations because the NS radius cannot be measured from radio-pulsars (one exception is through observations of double-pulsars, for which NS radii can be estimated by measuring the moment of inertia of the NSs, see Kramer et al. 2006). Figure credit: Demorest et al. (2010).

from observational perspective. We only need to measure its radius (or mass) and we know exactly all the properties of the star.

A more general solution for the Einstein's field equations of space-time curvature around a spinning star was found by Roy Kerr in 1964. It was quickly realised that this solution is also valid for every BH; the result for non-spinning Schwarzschild BHs is just a special case of this general solution (see Thorne 1994, for historical review). The difference between the non-spinning Schwarzschild BHs and the spinning Kerr BHs is that in the Kerr BHs the spinning causes the BH event horizon to become oblate. Perhaps more importantly from observational perspective, this spinning also allows orbiting particles to have stable orbits closer to the event horizon, unlike in the Schwarzschild BHs where orbiting particles that are closer than $3R_{\rm s}$ from the BH plunge into the hole (see e.g. Frank et al. 2002). These stable orbits allow to extract more gravitational potential energy from the orbiting particles, which allows a higher fraction of the rest mass energy to be emitted.

There are two types of BHs that we know of in the universe. The stellar-mass black holes (StMBH) and the super-massive black holes (SMBH). The former types of BHs are formed when massive stars collapse at the end of their evolution. The latter are found in the centres of galaxies and they must have been formed in the very early universe.

When a StMBH forms during a gravitational collapse of a massive progenitor star, its mass must be below $\lesssim 100\,{\rm M}_\odot$ for the following reason. The more massive progenitor star you have, the higher the temperature and the pressure are in its core and this causes the thermonuclear processes that produce the observed radiation to be more efficient per unit stellar mass. At some point the luminosity exceeds the limiting luminosity, the so called Eddington luminosity (see e.g. Frank et al. 2002)

$$L_{\rm Edd} = \frac{4\pi GMc}{\kappa} = \frac{4\pi GMm_{\rm p}c}{\sigma_{\rm T}} \approx 1.3\times10^{38}\left(\frac{M}{{\rm M}_\odot}\right){\rm erg\,s^{-1}}, \qquad (1.4)$$

where κ is the opacity, $\sigma_{\rm T}=6.65\times10^{-25}\,{\rm cm}^2$ is the Thomson cross section and $m_{\rm p}=1.67\times10^{-24}$ g is the proton mass. In Equation (1.4) the opacity is assumed to be $\kappa=\sigma_{\rm T}/m_{\rm p}$ (which is accurate for fully ionised hydrogen gas). Note that the Eddington luminosity is directly proportional to the mass of the star. If the stars luminosity would exceed this Eddington value, the radiation pressure would blow off the outer envelope to the interstellar medium (ISM; i.e. the gas and dust that fills the space between stars) thus acting as a mass self-regulation mechanism. This is why stars more massive than $\sim 100\,{\rm M}_\odot$ do not exist and, therefore, stellar BHs must have masses below this value when they are formed (Belczynski et al., 2010).

The only way to grow the BH mass from its initial value is through accretion. This is also the reason why BHs – and similarly NSs – emit light: compact stars

"come to life" when they accrete gas. The energy reservoir is the gravitational potential energy of the in-falling gas and this energy is partly converted into electromagnetic radiation that we can observe with our instruments. Therefore, in order to study BHs, they must be accreting matter (note that NSs can emit light through other mechanisms). There are two ways to accrete; 1) directly from the ISM or 2) the compact star is in a binary star system and the gas is supplied from the outer envelope of the companion star. In this thesis, I will present our results that aim to answer what are the maximum masses of BHs that can be produced from evolution of stars. The best candidates to look for these massive BHs are the extragalactic Ultra-Luminous X-ray sources (ULX), some of which may be powered by accreting $\sim 1000\,\mathrm{M}_\odot$ intermediate-mass black holes (IMBH; Colbert & Mushotzky 1999).

In the next section of this chapter I will shortly explain why compact stars emit X-ray and gamma-ray radiation. Because NS surfaces and regions close to BH event horizons emit X-ray light, we can estimate their masses and radii by studying this high-energy radiation.

1.3 Compact stars as sources of X-ray radiation

The reason why accreting compact stars are strong X-ray and gamma-ray emitting sources can be seen from the following argument (Frank et al., 2002). If we consider a star of mass M_* and radius R_* and let it accrete a particle of a mass m from a large distance (infinity) to its surface, the gravitational potential energy that is released by this accreting particle is given by $\Delta E_{\rm acc} = \frac{GM_*m}{R_*}$. If we consider further that instead of accreting a single particle, the star accretes a steady flow of particles at a rate of $\dot{M}$ ($\mathrm{g\,s^{-1}}$) and all the released gravitational potential energy is converted into electromagnetic radiation at the stellar surface, we obtain the accretion luminosity

$$L_{\rm acc} = \frac{GM_*\dot{M}}{R_*}. \tag{1.5}$$

We can ask ourselves, what are the typical energies of photons $E_{\rm phot} = h\bar{\nu}$ that correspond to the accretion luminosity (here $h \approx 6.6\times10^{-27}\,\mathrm{erg\,s}$ is the Planck constant, and $\bar{\nu}$ is a typical photon frequency)? Or, analogously, if the emitting gas is thermal, what is the temperature? We can consider two limiting cases.

In the first case, let us assume that the emission region covers the entire stellar surface – having total surface area of $4\pi R_*^2$ – and the emission region is optically thick, so that the gas and the radiation are in thermal equilibrium. In this case the emission is released in the form of a black body spectrum and we can define the corresponding black body temperature from the Stefan–Boltzmann

law

$$T_{\rm bb} = \left(\frac{L_{\rm acc}}{4\pi R_*^2 \sigma_{\rm sb}} \right)^{1/4}, \tag{1.6}$$

where $\sigma_{\rm sb} \approx 5.67 \times 10^{-5} {\rm erg\,cm^{-2}\,s^{-1}\,K^{-4}}$ is the Stefan–Boltzmann constant. In the second case, let us now assume that the emission region is optically thin, so that the gas and radiation do not interact. Let us further assume that the gas consists of ionised hydrogen and the entire gravitational potential energy of the accreting plasma [$GM_*(m_{\rm p}+m_{\rm e})/R_* \simeq GM_* m_{\rm p}/R_*$] is converted into thermal energy ($E_{\rm th} = 2 \times \frac{3}{2} kT$). In this case the temperature will be

$$T_{\rm th} = \frac{GM_* m_{\rm p}}{3kR_*}. \tag{1.7}$$

If we now put our canonical NS parameters into Equations (1.6) and (1.7), we obtain order of magnitude estimates for our expected photon energies (and temperatures). This exercise results in $kT_{\rm bb} \sim 1$ keV and $kT_{\rm th} \sim 50$ MeV, if we use typical luminosities $L_{\rm acc} \sim 10^{36}\,{\rm erg\,s^{-1}}$ and, therefore, we expect that emission from a NS surface is released primarily in X-rays and gamma-rays. Equations (1.6) and (1.7) also indicate that gas near the event horizons of StMBHs – with masses around $10\,{\rm M}_\odot$ and comparable sizes to NSs – have, to an order of magnitude, very similar temperatures than NSs. On the other hand, if we consider accreting white dwarfs that have typical radii of about $5 \times 10^8\,{\rm cm}$ and typical luminosities of about $L_{\rm acc} \sim 10^{33}\,{\rm erg\,s^{-1}}$, we find that $6\,{\rm eV} \lesssim h\bar{\nu} \lesssim 100$ keV. Thus, the larger sizes and typically lower luminosities of accreting white dwarf stars result in lower characteristic photon energies. Also, because of larger sizes of white dwarf stars, the gas densities around accreting white dwarfs (polars and intermediate polars) are very low and, therefore, the gas emits Bremsstrahlung with a temperature closer to $T_{\rm th} \sim 100$ keV (see e.g. Warner 1995). On the contrary, the small stellar radii of NSs (and analogously BHs) causes the emitting gas to be very dense and, therefore, in most cases the gas temperature is close to $T_{\rm bb} \sim 1$ keV. This is the key for compact star radius and mass estimations from X-ray measurements: as can be seen from Equation (1.6), the radii can be measured because luminosity and temperature can be obtained from modelling the observed X-ray spectrum. The X-ray telescopes we have used – being sensitive to X-rays from ~ 0.1 keV to ~ 100 keV (described in detail in the next Chapter) – are therefore perfectly suited to study thermal emission from all types of compact stars.

1.4 Aim and scope of the thesis

In this thesis, I have studied two types of binary star systems that contain an accreting compact star. The accreting millisecond pulsars (AMP) are NSs

that are powered by accretion from low-mass companion stars, and the ultra-luminous X-ray sources (ULX) are thought to be accreting BHs. There are 15 known AMPs detected in our Milky Way galaxy (hereafter Galaxy with capital G). In the last 10-30 years, hundreds of ULXs have been discovered in nearby galaxies (these discoveries were made possible with the improvements in focusing optics of X-ray telescopes, see Chapter 2), but there are no ULXs in the Galaxy.

The ultimate goal of my PhD work has been to study the properties of the compact stars in these systems through X-ray spectroscopic and timing analysis methods and to make estimations of their masses and radii. By studying pulsations and spectral variations of AMPs, we can probe properties of ultra-dense matter in NS cores and determine the correct NS EOS. From the NS EOS we can then indirectly infer maximum NS masses, and hence minimum masses of BHs. On the other hand, some ULX can be powered by accretion onto intermediate-mass black holes and, therefore, ULXs can be used to infer maximum BH masses that can be formed from stars. The estimations depend on various assumptions that are made on the nature of the X-ray emission that we observe with our instruments. Therefore, the immediate aim of this thesis is to investigate spectral- and timing variability patterns in these sources. Because various physical interpretations tend to predict different variability patterns, we can infer the nature of these sources by understanding their variability through careful analysis of the observational data.

The following Chapters are organized as follows. In Chapter 2, I review the instruments that we have used in our research and I will also shortly describe the methods that are used to analyse these data. In Chapter 3, I will discuss the AMP phenomena in great detail and I will present the results that we have obtained in our work. Then in Chapter 4, I discuss the ULX phenomena and our results in this field. I will then summarise the results we have obtained in Chapter 5.

Chapter 2

X-ray observatories

Theories – no matter how convincing they may seem – are meaningless without observational (or experimental) confirmation. For example, the existence of neutron stars – that was proposed by Baade and Zwicky in the 1930's – was only accepted in the late 1960's after the discovery of radio pulsars (i.e. the Crab pulsar, Comella et al. 1969) that could only be explained as rapidly spinning neutron stars.[1] Similarly, a theory was developed that the millisecond pulsars – discovered later by Backer et al. (1982) – have such short periods ($P < 10$ ms) because the NSs have been "spun-up" by accreting matter (see e.g. Alpar et al. 1982). This "pulsar recycling scenario" was neither fully accepted until the discovery of the first accreting millisecond pulsar (AMP) SAX J1808.4–3658 in 1998 using the *Rossi X-ray Timing Explorer* (*RXTE*, see Section 2.1) satellite (Wijnands & van der Klis, 1998; Chakrabarty & Morgan, 1998). In both of these cases, the discoveries and subsequent confirmation of the underlying theories were the results of new observing techniques or technical improvements in instrumentation.

Each of the satellites that we have used have unique capabilities. For example, the very high timing resolution and large effective area of one of the instruments on-board *RXTE* allowed the discovery AMPs. Similarly, technical improvements in focusing X-ray optics have allowed for similar advancements to be made in the field of ULXs. ULXs – although intrinsically extremely luminous – are very faint objects in the X-ray sky: the brightest ULX has flux of about $F_{\rm x} \approx 10^{-10}\,{\rm erg\,cm^{-2}\,s^{-1}}$ in the 0.2–10 keV band (Kaaret et al., 2001). The improved angular resolution and sensitivity of current X-ray telescopes like *XMM-Newton*, *Chandra*, *Swift* and *Suzaku* has allowed for several advancements in the past decade in this field.

In this chapter, I will introduce the X-ray and gamma-ray instrumentation

[1] Note that "ordinary" ~ 1 second period radio pulsars could have also be explained by oscillations of white dwarfs (Hewish et al., 1968; Staelin & Reifenstein, 1968), while the short 33 ms period of Crab pulsar cannot.

that I have used in this PhD thesis work. All instruments are on-board ESA and NASA operated satellites because the Earth's atmosphere is opaque to X-ray and gamma-ray radiation. In Sections 2.1–2.4, I will present the properties and capabilities of the satellites that host the instruments. Then, in Section 2.5, I will introduce the common techniques that we have used to analyse and model these data.

2.1 Rossi X-ray Timing Explorer

The *Rossi X-ray Timing Explorer* (*RXTE*, Bradt et al. 1993) was an X-ray observatory operated by NASA. It was launched into a low-earth orbit (altitude ~ 600 km, Bradt et al. 1993) on December 30, 1995 and the mission ended on January 4, 2012 (Shaposhnikov et al., 2012). The observing schedule of *RXTE* was designed to be highly flexible and, therefore, it was a very productive satellite to observe several transient phenomena. Besides the discovery of AMPs, *RXTE* also discovered several other new phenomena, including kilohertz (kHz) quasi-periodic oscillations (QPO) and X-ray burst oscillations (see Strohmayer et al. 1996; van der Klis et al. 1996 and van der Klis 2000 for review). We have used data from this satellite in Paper I and in Paper II for both timing analysis and spectroscopy of AMPs.

RXTE hosts three instruments (see Figure 2.1). The two principal instruments – PCA and HEXTE, which are described in more detail in the Sections 2.1.1 and 2.1.2 – were specifically designed for timing studies and low-resolution spectroscopy of relatively bright X-ray sources in a broad 2–250 keV band. The third instrument on-board *RXTE* is the All-Sky Monitor (ASM). Because we have not used the data from this instrument in this thesis, I will only refer the reader to Bradt et al. (1993) and Levine et al. (1996) for an overview of its properties and capabilities.

2.1.1 Proportional Counter Array (PCA)

The primary instrument on-board the *RXTE* is the Proportional Counter Array (PCA; Jahoda et al. 2006), which is sensitive to X-ray radiation in the 2–60 keV band. Similar proportional counters were used already in the *Uhuru* mission (Giacconi et al., 1971) and they have many advantages when observing bright X-ray objects. The PCA consists of five Proportional Counter Units (PCU0 to PCU4, see Figure 2.2 for a schematic illustration of a PCU). These PCUs do not have focusing optics. Instead, the X-ray light from the target object reaches the detector "volume" through a collimator that is housed on top of the main detector. The PCU collimators provide a field of view (FOV) of $\sim 1^{\circ}$.

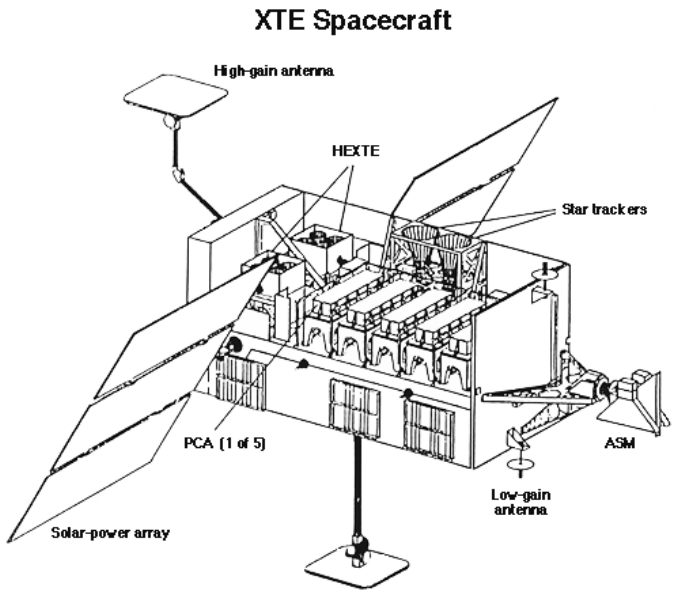

Figure 2.1. Schematic view of *RXTE*. The PCA and the HEXTE clusters are housed within the body of the satellite, whereas the three Scanning Shadow Cameras of the ASM are attached to an extended rotating boom. Credit: NASA.

The PCUs consist of three layers of xenon gas giving a collecting area of $\sim 1600\,\mathrm{cm}^2$ per PCU. Each detector layer is further divided in half by connecting alternate detector anode cells to either left or right amplifier chains (named 1L, 1R, 2L, 2R, 3L, 3R). These three xenon layers are surrounded by two "veto" layers to reject non-X-ray induced "events"; 1) the propane layer that is located between the collimator and the top xenon layer and 2) a xenon veto layer located below the third detector layer. Furthermore, the outermost anode on each of the three main detector layers is also connected to the bottom veto layer. Each event that is simultaneously detected in more than one layer of the PCU consist mostly of energetic cosmic rays, which are rejected as background (Jahoda et al., 2006). Below the bottom veto layer there is a radioactive source ^{241}Am (americium), which produces emission lines in the 13–60 keV range. These emission lines are used for photon energy calibration purposes.

The X-ray detection mechanism of the PCA is rather straight forward (see Jahoda et al. 2006; Arnaud et al. 2011). When an X-ray photon passes through the collimator it will photo-ionise a xenon atom in the detector volume, thus producing a photo-electron. This photo-electron can then ionise other xenon atoms, thus producing a population of secondary electrons. This electron cloud drifts to the anode, where the resulting Pulse Height Amplitude (PHA, i.e. the height of the voltage pulse) is proportional to the number of elec-

trons hitting the anode. Therefore, as the number of produced electrons is proportional to the incident X-ray energy, the PCA is a low resolution spectrograph. The key feature of the PCA is that readout times of X-ray events are very fast (approximately 10 μs) and, therefore, it can be used to observe X-ray sources from the flux limit of $F \approx 4 \times 10^{-12}\,\mathrm{erg\,cm^{-2}\,s^{-1}}$ (which corresponds to about $0.3\,\mathrm{cts\,s^{-1}\,PCU^{-1}}$) in the 2–10 keV band to extreme count rates up to $20000\,\mathrm{cts\,s^{-1}\,PCU^{-1}}$.

2.1.2 High Energy X-ray Timing Experiment (HEXTE)

High Energy X-ray Timing Experiment (HEXTE; Gruber et al. 1996; Rothschild et al. 1998) operates in the 15–250 keV band. The instrument consists of two independent clusters (clusters A and B), each holding 4 NaI/CsI "phoswich" scintillation detectors, which are coupled to photo-multipliers (see Figure 2.2). The effective area of each cluster is approximately 800 cm^2 in the 20–80 keV range. The effective area drops below 20 keV due to photoelectric absorption in the housing above the detector and the reduction above 80 keV is caused by the finite thickness of the NaI(Tl) crystals (sodium iodide doped with thallium). In addition, at about 30 keV, there is a sharp drop in the effective area (to about 600 cm^2) because of a change in the photo-electric cross section at the K edge of iodine. In principle, the detectors can detect X-rays with energies above 5 keV, but a lower energy threshold of 15 keV was set to reduce the background rate and also to reserve telemetry capacity to PCA. Also, in practice, the PCA has far larger effective area than HEXTE below 25 keV and, therefore, a lower threshold of 25 keV is usually used when analysing and modelling data from this instrument.

The structure of a HEXTE detector phoswich is shown in Figure 2.2 (see also Bradt et al. 1993; Rothschild et al. 1998). The 0.3 cm thick NaI(Tl) crystals are located right below the lead honeycomb collimators that provide a 1$^\mathrm{o}$ FOV. The 5.69 cm thick CsI(Na) (cesium iodide doped with sodium) crystals are located below the NaI(Tl) crystals. The CsI(Na) crystals are connected to the photomultiplier tube's photo-cathode. The detector works in the following way. After the high energy X-ray light passes through the lead collimator, the NaI(Tl) crystals absorb the photons causing them to scintillate (i.e. to produce optical light). The generated optical light is then absorbed in the photo-cathode which, in turn, causes emission of electrons in a photoelectric effect. The created photo-electrons are then "multiplied" by colliding them with a series of 10 dynodes, providing an avalanche of secondary electrons in the photomultiplier (each electron collision with a dynode produces more electrons). Finally, the electron cloud is absorbed in the anode and the PHA is measured, which is proportional to the energy of the initial X-ray photon. The pulse heights are calibrated (i.e. gain is measured) using a ^{241}Am calibration X-ray source that is

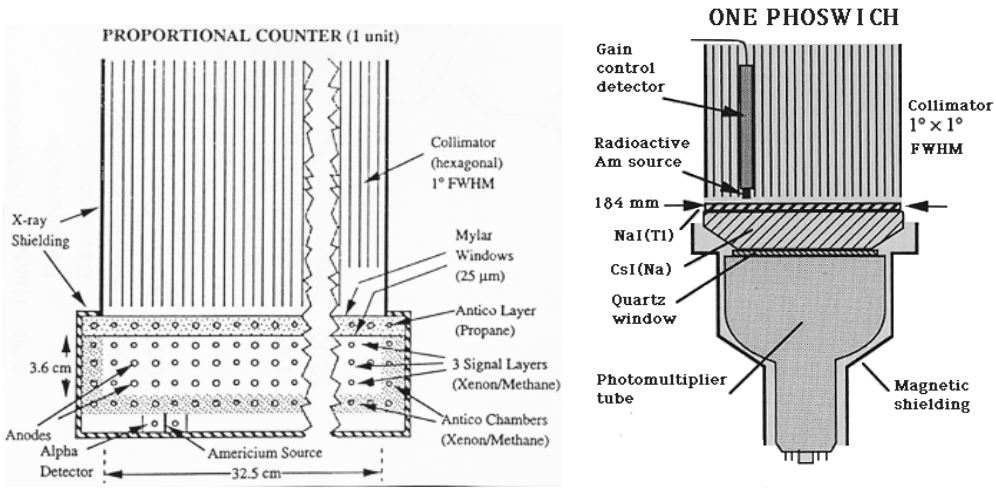

Figure 2.2. Left: A diagram of a PCU. Right: A diagram of a HEXTE phoswich. Both diagrams are courtesy of Hale Bradt, M. Halverson, and students.

embedded in the collimator. The gain is automatically adjusted to maintain a constant PHA for the 60 keV emission line. This procedure guarantees that the each PHA can be assigned to a specific X-ray photon energy.

The role of the CsI(Na) crystals is to reject events (scintillation) caused by charged particles. Charged (energetic) particles can cause both NaI(Tl) and CsI(Na) crystals to scintillate whereas X-rays that pass through the collimator should be absorbed in the NaI(Tl) crystal. Because the characteristic decay times of the scintillation are different in these crystals (0.25 μs and 0.63 μs for NaI(Tl) and CsI(Na), respectively), particle events can be distinguished by analysing the time-evolution of the PHA. The pulses that have longer decay times are caused by CsI(Na) and those events are rejected as particle background. The background is also comprised of cosmic-ray induced events, which can be identified by having five sides of the main HEXTE detectors surrounded by anti-coincidence shield detectors. When a cosmic ray passes through the satellite an event can be registered simultaneously in both detectors, whereas X-rays from the target are only registered in the main HEXTE detector. A large fraction of such cosmic ray events can be detected and rejected as background.

The cosmic rays produce several radioactive isotopes of iodine – which can then decay to tellurium – producing several emission lines because of electron capture induced K-alpha emission (at 30 keV, 55 keV and 190keV from Te, ^{121}I and ^{123}I, respectively). On top of the cosmic ray induced lines there is a featureless continuum caused mainly by beta-decays of the same radioactive species. Also, the lead collimator can produce a strong fluorescence line at about 80 keV when impacted with cosmic rays or when absorbing X-rays. Curi-

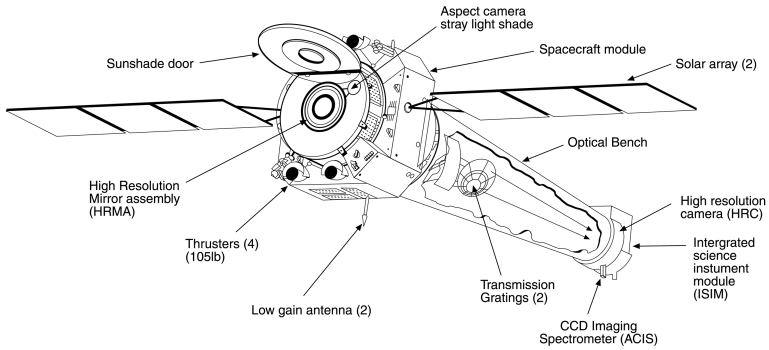

Figure 2.3. Schematic view of the *Chandra* satellite. Credit: NASA/CXC/NGST.

ously, the cosmic X-ray and gamma-ray background (from unresolved sources) only contributes less than 5 per cent to the total background. This can be removed by switching ("rocking") the HEXTE clusters in 16 second intervals between the source position and empty sky (1.5^{o}–3^{o} away). The two clusters rock in a manner such that one cluster is observing the source, while the other is observing a blank sky field. Because of the high detector background and the modest collecting area of HEXTE, only the brightest Galactic X-ray sources can be observed with this instrument.

2.2 Chandra

The *Chandra X-ray observatory* (CXO; hereafter *Chandra*) is a NASA operated X-ray satellite and it was launched on July 23, 1999 (Weisskopf et al., 2002). It was placed into a highly elliptical orbit (10000 km perigee and 140000 km apogee) with 63.5 hour period, so uninterrupted observations for more than 2 days are possible. *Chandra* can detect photons in the soft X-ray range between 0.1–10 keV. What makes *Chandra* stand out from all other X-ray satellites, is its point spread function (PSF) of less than $1''$ (Full With at Half Maximum, FWHM). This property of *Chandra* is irreplaceable when analysing data from crowded regions like star-burst galaxies. In the famous examples M82 and the Antennae galaxies, there are so many ULXs and other X-ray sources that only *Chandra* can resolve individual sources. We have used *Chandra* data in Paper III for spectroscopy of ULXs.

2.2.1 Focusing optics and Charged Coupled Devices in X-ray astronomy

Chandra has a focusing X-ray telescope and it has two focal plane instruments. The more commonly used instrument is the Advanced CCD Imaging Spectrometer (ACIS, Garmire et al. 2003), to which I reserve a separate section below. The other focal plane instrument of *Chandra* is the High Resolution Camera (HRC). But again, as we have not used HRC data in this thesis, I refer the reader to Murray et al. (2000) for details of this instrument.

From the name of the ACIS instrument one sees that the detector is a Charged Coupled Device (CCD). CCDs are currently very common detectors in X-ray astronomy. In fact, all the rest of the instruments discussed in this Chapter are CCDs, some of which are identical to each other. Therefore, instead of describing the details of each instrument separately, I will first describe how focusing optics and CCDs provide imaging- and imaging-spectroscopic capabilities in the X-ray band of ~ 0.1–10 keV.

The mirrors of X-rays telescopes differ from their traditional optical cousins. The main reason for the differences in design has to do with the difficulty to reflect X-rays. In the traditional optical reflectors, the light is first reflected from the primary mirror to the secondary mirror, which is located above the primary. Then, the secondary mirror reflects the light to a focal plane (in Nasmyth/coudé telescopes a tertiary mirror is used as well). The key point here is that when the optical light is reflected, the reflection angles (angle between the incident photon and the mirror surface normal) are small. Such reflection angles are impossible for X-rays. Instead of being reflected, the X-rays are absorbed in the material or they penetrate the telescope altogether. This problem can be overcome by designing the mirrors so that the X-ray photons hit the mirror at a very large reflection angle, called a grazing angle (which is $90^{\rm o}$ minus the reflection angle, i.e. the X-rays reflect almost along the surface tangent). When the grazing angle is smaller than a certain critical angle $\theta_{\rm c}$, even X-rays can be reflected. The critical angle is proportional to $\theta_{\rm c} \propto \sqrt{Z}/E_\nu$, where Z is the atomic number and E_ν is the photon energy (Arnaud et al., 2011). Therefore, by using high-Z materials such as gold or iridium, one can design grazing incidence mirrors with $\sim 1^{\rm o}$ grazing angles to reflect X-rays. The most common of such grazing incidence mirror configurations is the Wolter-I design (Wolter, 1952a,b). In this type of mirror, the X-rays are first reflected off the concave surface of a paraboloid mirror and then off the concave surface of a hyperboloid mirror (see Figure 2.4). This configuration provides the largest aperture-to-focal length ratio, coma-free imaging of the different Wolter mirrors (see Arnaud et al. 2011). It is easy to imagine that if the X-rays hit the mirrors with only $\sim 1^{\rm o}$ grazing angles, then the mirror area is very small compared to traditional optical mirrors. Therefore, to increase the effective telescope area, many Wolter mirrors should

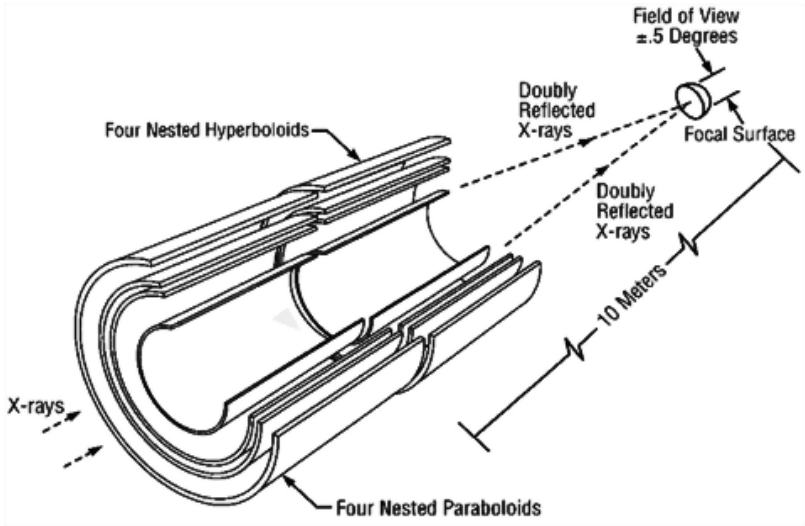

Figure 2.4. Illustration of the four nested Wolter-I telescopes of the *Chandra* HRMA. The celestial X-rays are doubly reflected into the focal plane, where the instruments are located. Credit: NASA/CXC.

be nested in one telescope, much like in the Russian Matryoshka dolls.

CCD cameras are ideal focal plane detectors of soft X-rays because of their high sensitivity and linear response to X-ray radiation. In essence, a CCD is a collection of capacitors, which are linked to each other as a 2-dimensional pixelised grid. The detector material is typically made of silicon, with deliberately added impurities to increase the semiconducting properties. When a few silicon atoms (which have 4 valence electrons) are replaced with phosphorous atoms (5 valence electrons), this is called an n-type semiconductor having excess of free electrons. When a few silicon atoms are replaced with boron atoms (3 valence electrons) a p-type semiconductor is created with excess of free holes. Combining both types of semiconductor materials in one detector creates a p-n CCD (used in *XMM-Newton* EPIC-pn, described in Section 2.3.1). This type of CCD schematic is illustrated in Figure 2.5. The other type of X-ray CCD is the metal-oxide semiconductor (MOS) design that utilises only p-type semiconducting silicon. The MOS design is used in *Chandra*/ACIS CCDs, *XMM-Newton*/EPIC-mos CCDs and also in *Swift*/XRT.

The X-ray detection technique of a CCD is very elegant. When an X-ray is absorbed in the semiconducting detector material it creates electron-hole pairs. The number of produced electrons is linearly proportional to the incident X-ray photon energy and the electrons are collected in the potential wells under the metal gates by applying a voltage to the gates. As each pixel is connected to its neighbours, the collected charge can be transferred by altering the voltages

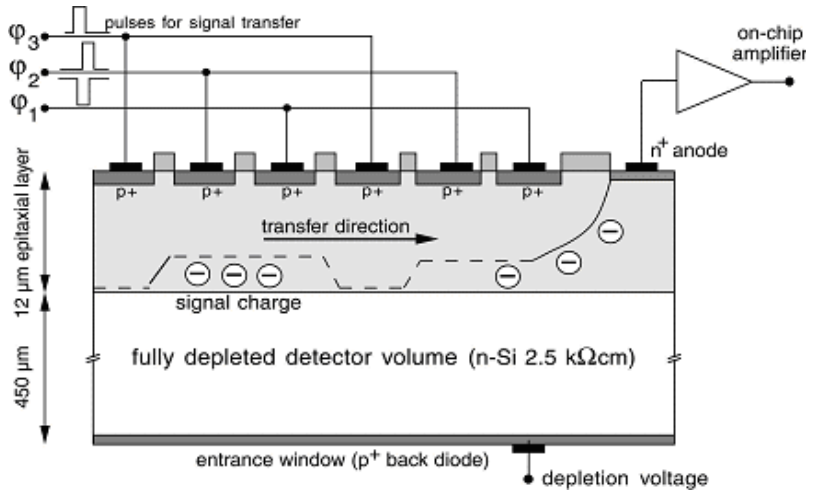

Figure 2.5. Illustration of a p-n CCD that is used in the EPIC-pn instrument (see Section 2.3.1). Image courtesy of PNSensor GmbH.

on adjacent gates subsequently. Entire pixel columns can be transferred simultaneously in one direction and the charge is either; 1) "read out" directly in a readout amplifier (as in *XMM-Newton* EPIC-pn) or 2) the charge is carried to a separate frame store region (as in *Chandra* ACIS), where the pixel columns are read out one-by-one in an amplifier node during one readout cycle (see Arnaud et al. 2011). Because a single X-ray can generate tens to thousands of electron-hole pairs, the signal is sufficiently strong so that individual X-ray photons can be detected. This is done by adjusting the CCDs readout cycle to be much higher than the average X-ray count rate in order to prevent two (or more) X-rays to impact the detector within one readout cycle. Therefore, focusing telescopes equipped with X-ray CCDs are imaging spectrographs. Various effects can cause problems when the photon energies are measured using CCDs. One example is charge transfer inefficiency, which is particularly severe in CCDs with fast readout cycles. These issues are described in better detail in Section 2.5.

2.2.2 Advanced CCD Imaging Spectrometer (ACIS)

The Advanced CCD Imaging Spectrometer (ACIS) on-board *Chandra* has 10 CCDs that are arranged in two configurations (see Garmire et al. 2003, for ACIS properties). The ACIS-I is optimised for imaging observations and it consists of 4 CCDs that are arranged in a square array. The other configuration is the ACIS-S that consists of 6 CCDs, which are arranged in a linear array. ACIS-S is typically used together with the High-Energy Transmission Grating

(HETG), but it is also used for imaging observations because one of the ACIS-S CCDs has a better response to low-energy X-rays below ~ 1 keV than in ACIS-I (see Weisskopf et al. 2002; Garmire et al. 2003). The four nested Wolter-I mirrors of the High-Resolution Mirror Assembly (HRMA), and almost 100 per cent quantum efficiency of the ACIS CCDs, provide an effective area of approximately $800\,\mathrm{cm}^2$ at energies below 2 keV and $400\,\mathrm{cm}^2$ in the 2–5 keV band (Weisskopf et al., 2002).

The PSF of HRMA is better than 1″ FWHM for on-axis targets (for off-axis target PSF quickly worsens). The ACIS CCDs are designed to match this PSF, as the $24\,\mu\mathrm{m}$ pixel width corresponds to $0\farcs492$ at the focal surface. All CCDs have $8\farcm4 \times 8\farcm4$ FOV. They consist of 1024×1026 pixels and a separate frame store region, where the image is transferred in 41 milliseconds for readout. Most typical CCD readout cycle is 3.24 seconds for the imaging mode, although modes with shorter readout times can be used to increase time resolution of the instrument.

2.3 XMM-Newton

European Space Agency launched the *XMM-Newton* space observatory on December 10, 1999 and the mission is still operational (see Jansen et al. 2001 for *XMM-Newton* properties). *XMM-Newton* hosts three X-ray telescopes, each of them consisting of 58 nested, gold coated, Wolter-I mirrors. Each telescope mirror provides an effective area of approximately $1500\,\mathrm{cm}^2$. Three European Photon Imaging Cameras (EPIC) are located in the focal planes of the X-ray telescopes; EPIC-pn (see Section 2.3.1), EPIC-mos1 and EPIC-mos2 (see Section 2.3.2). In addition, the two X-ray telescopes that are fitted with EPIC-mos instruments have X-ray gratings (called Reflection Grating Arrays, RGA), which divert almost half of the incoming X-rays to the Reflection Grating Spectrometer (RGS) instruments (den Herder et al., 2001). The RGSs provide very high energy resolution and can register photons at energies in the range of 0.33–2.5 keV. Also, *XMM-Newton* has a 30 cm diameter optical telescope, the Optical Monitor (OM, see Mason et al. 2001 for its properties).

XMM-Newton was placed in a highly elliptical 48 hour orbit that allows long continuous observations of celestial targets. The drawback is that the targets are not always observable and the telescope scheduling is less flexible than for missions like *RXTE*, which influenced our observations of an ULX in the Holmberg II galaxy (see Paper V). *XMM-Newton* has been a phenomenal success and is the main workhorse for current ULX spectral studies. We have used *XMM-Newton* in Paper III and Paper V for spectroscopy of ULXs.

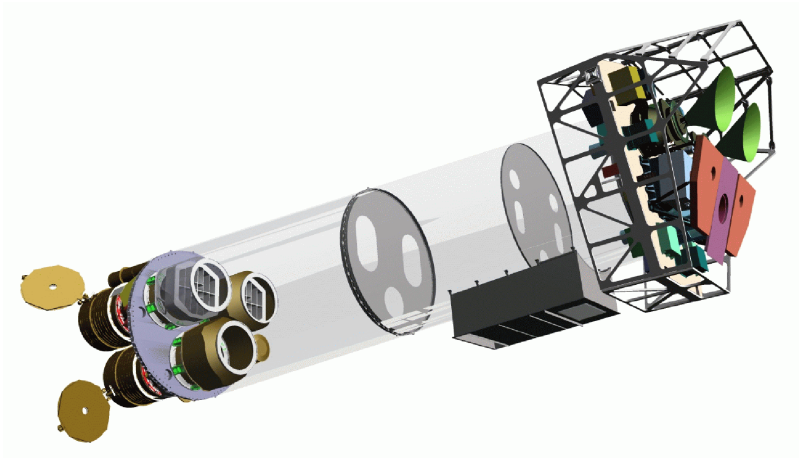

Figure 2.6. Schematic view of the *XMM-Newton* satellite. The bottom X-ray telescope focuses X-ray to the EPIC-pn camera (violet). The two top X-ray telescopes feed the EPIC-mos detectors (located below the green "horn-like" radiators) and also about half of the X-ray light is reflected in the RGAs (located below the X-ray telescopes) to the RGSs (red detectors next to the EPIC-pn camera). A small part of the optical monitor is also be seen behind the bottom X-ray telescope for EPIC-pn. Image courtesy of Dornier Satellitensysteme GmbH and ESA.

2.3.1 EPIC-pn

The EPIC-pn (Strüder et al., 2001) is an array of 12 CCDs, that have a combined geometric area of $6 \times 6\,\mathrm{cm}^2$. Each of the CCDs consist of 64×198 pixels, that have $150\mu\mathrm{m} \times 150\mu\mathrm{m}$ pixel size, which corresponds to $4\farcs1$. This is well suited for the $6\farcs6$ PSF of the telescope. EPIC-pn is sensitive to photon energies up to 15 keV, but typically 10 keV (and sometimes 12 keV) upper energy bounds are used. The lower energy bound is determined mostly by the optical blocking filters (see Strüder et al. 2001, table 2) and well calibrated lower energy bounds are 0.3–0.6 keV, depending on the readout modes of the instrument.

The most common readout mode for low flux sources such as ULXs is the full frame mode, which has a 73.3 ms readout cycle over a $27\farcm2 \times 26\farcm2$ FOV. The time resolution can be increased to $30\mu\mathrm{s}$ in the timing mode (see Strüder et al. 2001, table 1 for other readout modes). The timing mode is very useful to study AMP pulsations below the ~ 3 keV sensitivity of *RXTE*/PCA, where accretion disc emission is clearly detected for SAX J1808.4–3658 (Patruno et al., 2009a). In the full frame mode, it takes 4.6 ms for the readout itself and because there are no shutters in the camera (the CCD is exposed continuously), 6.2 per cent of photons come "out-of-time" during readout. These events should be removed in principle, as they can cause spectral lines to become broader. However, for ULX

spectroscopy, these out-of-time events have no practical effect on the observed spectra as ULXs tend to show no lines and the number of detected photons is very low.

The fast readout of EPIC-pn is achieved by having a readout node for each pixel column. This gives much shorter readout cycle comparing to the 3.24 second cycle of *Chandra*/ACIS. EPIC-pn, therefore, has better time resolution but perhaps more importantly the faster readout time helps to mitigate a problem called photon pile-up (discussed in Section 2.5). But a major drawback of *XMM-Newton* (compared to *Chandra*) is observations of crowded regions like nearby star-burst galaxies. For example, in M82 and the Antennae galaxies, *XMM-Newton* cannot resolve individual ULXs. However, when crowding is not an issue *XMM-Newton*/EPIC-pn is far superior to *Chandra*/ACIS. It has a larger effective area (more photons are detected per second), better time resolution and broader spectral range, all of which turn out to be crucial for ULXs spectroscopy and timing analysis.

2.3.2 EPIC mos-1 and EPIC mos-2

The focal plane instruments of the other two X-ray telescopes of *XMM-Newton* are EPIC-mos1 and EPIC-mos2 (see Turner et al. 2001 for EPIC mos properties). As mentioned earlier, 44 per cent of the light passing through the X-ray telescopes reaches these cameras (the rest is reflected to the RGSs). The EPIC-mos instruments consist of 7 p-type CCDs. They are arranged in a mosaic, where 6 CCDs surround the central CCD in a hexagonal pattern. The combined CCD mosaic provide a $28\farcm4$ diameter FOV. The imaging section has 600×600 pixels and each pixel covers a $1\farcs1 \times 1\farcs1$ FOV. The two EPIC-MOS cameras are placed at a $45^{\rm o}$ angle with respect to the EPIC-pn to prevent any celestial object to fall in a CCD chip gap in all the three EPIC cameras. The readout cycle of the MOS CCDs is 2.6 seconds in the standard full frame mode but (as in EPIC-pn) faster modes are also possible.

2.4 Swift

Swift is a NASA operated mission that was launched on November 20, 2004. The primary mission purpose of *Swift* is to detect and localise gamma-ray bursts (Gehrels et al., 2004). The operation of *Swift* to observe gamma-ray bursts is autonomous. The Burst Alert Telescope (BAT; see Barthelmy 2004) is a coded mask instrument and it has a very large (half-coded) FOV of $100^{\rm o} \times 60^{\rm o}$. When a gamma-ray burst occurs in the BAT FOV, the burst position can be determined with an accuracy of $4'$ (Gehrels et al., 2004). If the gamma-ray burst location does not coincide with a known X-ray burster, the telescope then automatically

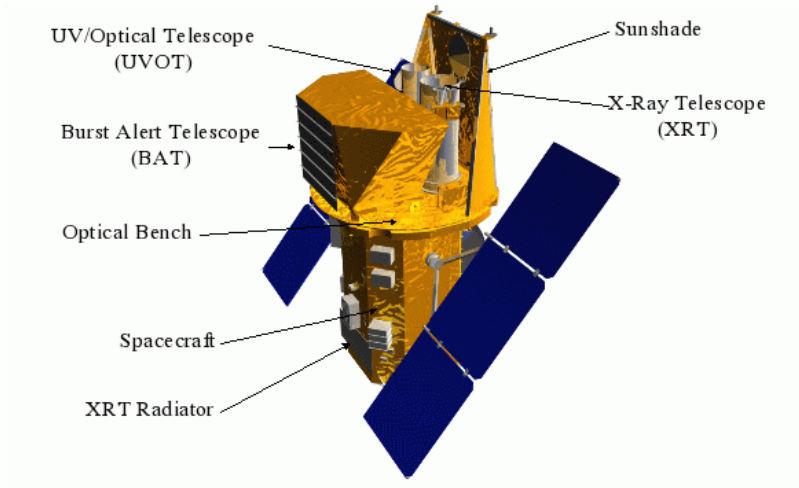

Figure 2.7. Schematic view of the *Swift* satellite. Image credit: NASA.

slews to observe the target with two narrow FOV instruments: the X-Ray Telescope (XRT, Burrows et al. 2005) and the UltraViolet/Optical Telescope (UVOT, Roming et al. 2004). The narrow field instruments of *Swift* use recycled parts from other missions. The UVOT, which is a mock-up of the *XMM-Newton*/OM (Mason et al., 2001), was not used in this thesis.

The gamma-ray burst rate is less than one per day. Often times the burst location is such that it is not visible during most of the satellite orbit (*Swift* was placed to a low earth orbit with a 600 km altitude and, for example, for most of the orbit the target is behind the Earth). Therefore, these gaps are filled with other targets that can be observed with the XRT (or UVOT). We have used *Swift* XRT data in Papers I, II, IV and V for spectral analysis and long term flux variation monitoring of both AMPs and ULXs.

The 12 gold coated, nested Wolter-I mirrors of *Swift*/XRT were originally designed and built for the JET-X instrument on the *Spectrum X-Gamma* mission, which was never launched (see Burrows et al. 2005). The mirrors provide an effective area of $110\,\mathrm{cm}^2$ and a FOV of $23'$. The focal plane instrument is a single CCD that is similar to those used in the EPIC-mos cameras. The time resolution is 2.5 seconds in the "photon counting" (PC) mode (imaging mode), or it can be increased to 1.8 ms in the Windowed Timing (WT) mode. In ULX observations, where target fluxes are very low, the PC mode is used, whereas for AMPs the WT mode is more appropriate. However, the time resolution even in the WT mode is not adequate for analysing the pulsations of AMPs such as IGR J17511–3057 or SAX J1808.4–3658. Therefore, in Paper I and Paper II, *Swift*/XRT data was only used for time-averaged spectroscopy.

2.5 X-ray spectroscopy and spectral modelling

The data from all these observatories must be calibrated and treated before they can be used for scientific analysis. It is common that during an observation the satellite encounters a "cloud" of energetic particles, which cause the instrumental background to increase substantially. In addition, many different instrumental effects can influence the data quality. In X-ray CCDs photon pile-up – i.e. when instead of one X-ray photon, two or more photons hits the detector during one readout cycle – can distort the observed spectrum. One effect of pile-up is an artificial increase of the observed photon energies (instead of two low energy photons, one photon with double the energy is detected). Another effect is the so-called pattern pile-up where two photons hit adjacent pixels and are discarded as cosmic-ray induced background. A similar effect to pile-up in proportional counters, such as the *RXTE*/PCA, is dead-time. When the electron cloud (produced by the X-ray photon) hits the detector anodes, they go "off-line" for a short period of time (microseconds) during which further photons cannot be detected. All these kind of instrumental effects must be eliminated (or mitigated) from the raw data that is sent down to the ground by the satellite.

There are several data manipulation tools available to "reduce" the raw data. Some of them are common for all satellites like the HEASOFT FTOOLS (Blackburn, 1995). However, some of the tools are designed to manipulate data files from specific observatories, such as the CIAO package for *Chandra* data (Fruscione et al., 2006) and the XMM-SAS for *XMM-Newton* data (Gabriel et al., 2004). These software packages can be used to create clean, calibrated science data products out of the raw data. For example, if we want to determine the X-ray spectrum of a celestial source, contrary to intuition, the data we receive from the spectrograph is not the spectrum of the source. Instead, what is observed is the number of photon detections in a specific detector channel

$$C(PI) = T_{\rm obs} \int \mathrm{RMF}(PI, E) \times \mathrm{ARF}(E) \times S(E) \times \mathrm{dE}. \qquad (2.1)$$

Here $S(E)$ is the source flux at energy E (which we want to measure), $T_{\rm obs}$ is the observing time, $\mathrm{ARF}(E)$ (Ancillary Response File) is the energy-dependent effective area of the telescope and $\mathrm{RMF}(PI, E)$ (Response Matrix File) gives the probability to detect a photon of energy E in a detector channel PI (Arnaud et al., 2011). The ARF has units of cm^2 and it is essentially the combination of the geometric surface area of the telescope mirrors and the quantum efficiency of the detector. Current X-ray CCDs reach close to 100 per cent quantum efficiencies, except around ionisation edges of detector materials (mainly silicon at 1.84 keV). Similarly, the xenon L-edge in the *RXTE*/PCA creates a large discontinuity in the effective detector area around 4.78 keV, which can cause

large effects if not considered carefully (compare Miller et al. 2006 and Done & Diaz Trigo 2010). The RMF, which describes the relation between the observed pulse height amplitudes (PHAs) and the photon energies, can be combined with the ARF and this combination is generally called the instrument response. The RMF and ARF are problematic properties to quantify, as they tend to change during the lifetime of a given telescope. For example, the charge transfer efficiency (CTE) of a CCD might have suddenly dropped because one malfunctioning "hot pixel" had appeared in the readout column where the celestial target photons are being readout during the observation. Changes in CTE can affect the energy redistribution and thus the RMF is incorrect, causing photon energies to be slightly wrong. Such effect can be particularly nasty around the instrumental edges where the instrument response changes rapidly (like at the silicon 1.84 keV edge, see Paper II). Therefore, telescope teams are constantly doing calibration observations and they are regularly updating and improving the responses (see e.g. Shaposhnikov et al. 2012, for a post-mission *RXTE*/PCA response update).

In principle, the source spectrum $S(E)$ can be obtained from the observed "count spectrum" ($C(PI)$) by solving Equation (2.1). However, such inversion is typically non-unique and it is very sensitive to small changes in the response, which is not always accurate. Therefore, instead of solving Equation (2.1), we "guess" a model $S_{\rm M}(E, p_i)$ with some parameters p_i. We then convolve the model spectrum with the response and compare the model count spectrum $C_{\rm M}(PI)$ to the observed $C(PI)$. We find the best fitting parameters p_i and evaluate the goodness-of-fit of the model. Almost exclusively, χ^2 minimization is used in astronomy (see Arnaud et al. 2011) and the most common software package for spectral modelling is XSPEC (Arnaud, 1996). With respect to AMP pulse profile modelling (described in the following Chapter), very similar techniques are used for spectral analysis: the observational time-series data is folded with the NS spin period and the resulting pulse profile is compared to a simulated pulse profile. The code that I have used to compute and model the pulsations has been developed by J. Poutanen.

Chapter 3

Accreting millisecond pulsars

3.1 Discovery of accreting millisecond pulsars

The first Accreting Millisecond Pulsar (AMP)[1] SAX J1808.4–3658 was discovered in 1998 (Wijnands & van der Klis, 1998; Chakrabarty & Morgan, 1998). This exciting discovery was important for a multitude of reasons. First, the discovery of a new type of binary star system is always an interesting and rare event on its own. But the initial excitement was related to the importance of AMPs to radio astronomy, specifically to the evolutionary origin of radio millisecond pulsars. These millisecond pulsars were discovered by Backer et al. (1982) after "ordinary" radio pulsars which have longer spin periods (see Hewish et al. 1968; Staelin & Reifenstein 1968; Comella et al. 1969). It was proposed that the millisecond pulsars had been spun-up by accreting matter from a binary companion (see e.g. Alpar et al. 1982). This "pulsar recycling scenario" remained unconfirmed as one would expect accretion episodes to produce strong X-ray emission and, therefore, they should be seen as AMPs. The discovery of SAX J1808.4–3658 thus "confirmed" the evolutionary track of formation of millisecond pulsars.

However, simply by detecting an AMP, we do not yet confirm that the NS is actually being spun-up by accretion torques. For a definite confirmation of the pulsar recycling scenario, we need to measure the spin-frequency derivative of the NS during an X-ray outburst. However, this is far from being a trivial measurement. There are many phenomena that can cause the observed pulse frequency (and its derivative) to deviate from the NS spin frequency (and its derivative). In this Chapter I will discuss our results that address some of the complications with these measurements (see also Papers I and II).

[1] There is no well-established name for Accreting Millisecond Pulsars. Other alternatives include Accretion-Powered Millisecond Pulsar (Galloway & Cumming, 2006), Accreting X-ray Millisecond Pulsar (Tauris, 2012), Accreting Millisecond X-ray Pulsar (Wijnands, 2006b) and Accretion-Driven Millisecond X-ray Pulsar (Wijnands, 2006a).

Although the initial excitement of AMPs was related to the recycling scenario and the spin frequency derivative measurements, it was quickly realised that even more important measurements can be made. As was alluded to in the introduction, it is possible to measure NS masses (M) and radii (R) by observing AMPs. This way, the EOS of NS matter can be determined, which tells us how matter behaves at supra-nuclear densities (Haensel et al., 2007). The mass and radius measurements are, however, hidden behind a forest of poorly understood factors that need to be considered before we can make progress in this respect. Because of these unknown factors, current M–R constraints derived for AMPs are very loose (see Poutanen & Gierliński (2003); Leahy et al. (2008); Morsink & Leahy (2011) for SAX J1808.4–3658, Leahy et al. (2009) for XTE J1814–338 and Leahy et al. (2011) for XTE J1807–294) and they cannot be used to distinguish between various NS models. However, the main advantage of AMPs is that the M–R estimations do not depend strongly on distances, which is the source of greatest uncertainty in other M–R measurements approaches like in the case of X-ray bursts (e.g. Suleimanov et al. 2011).

In this Chapter I will argue that the interaction between the NS magnetic field and the accretion disc can be variable during X-ray outbursts of AMPs. More specifically I claim that *variations in the size of the disc-magnetosphere interaction region can occur independently of changes in the mass accretion rate $\dot{M}$ onto the NS*. I will then argue how this physical picture can explain

I. the simultaneous spectral- and pulse profile transition that was detected in the 2008 outburst of SAX J1808.4–3658 (reported in Paper II),

II. the $\dot{M}$-independent variations of pulse profiles in SAX J1808.4–3658 (reported in Paper II)

III. the $\dot{M}$-independent X-ray timing noise in AMPs (including IGR J17511–3057, see Paper I and SAX J1808.4–3658, see Paper II),

IV. pulse profile changes as variations in the size of the X-ray emitting hotspots.

These points are very important for accurate M–R determinations and spin-up torque measurements in future studies for reasons that will be outlined in the following Sections of this Chapter.

3.2 Origin of pulsations

As has been mentioned already in the introduction, AMPs are accreting NSs. They are all low-mass X-ray binaries (LMXB) meaning that the companion star, which is the mass reservoir for the accreting gas, has low mass (typically below

$\sim 1\mathrm{M}_\odot$). During the binary evolution, the NS and the companion star can come so close to each other (or the companion star radius can increase), that the outer envelope of the companion star starts to "leak" onto the more massive NS. In this case, it is said that the companion star fills its Roche lobe and the matter is accreted through the inner Lagrangian point (Frank et al., 2002).

Because the two stars orbit each other, the in-falling gas will not fall directly towards the NS. Instead, the gas settles into a nearly circular orbit around the NS forming an accretion disc. As the gas in the accretion disc contains significant amount of angular momentum, it must be "lost" (or redistributed outwards) in order for accretion to be possible. The mechanism for the angular momentum redistribution and resulting mass accretion is not yet entirely certain but the most likely mechanism is the Magneto-Rotational Instability (MRI; see Balbus & Hawley 1998, for review).

Once the gas reaches the vicinity of the NS, the NS magnetic field starts to play a role in the accretion flow (magnetic accretion has been studied since the early seventies, see Pringle & Rees 1972; Lamb et al. 1973). The inflowing gas can be considered to be highly conducting plasma and thus, the magnetic field and gas are interconnected. The magnetic field can be considered to be "frozen" into the plasma and the gas motion depends on relative fraction of the magnetic energy density ($E_\mathrm{B} = B^2/8\pi$) to the energy density of the in-falling gas (E_g). Although the gas in the disc follows roughly circular (Keplerian) orbits with an orbital frequency

$$\nu_\phi \simeq \nu_\mathrm{K} = \frac{1}{2\pi}\sqrt{\frac{GM}{r^3}}, \tag{3.1}$$

the radial (accretion) velocity can approach the free fall velocity $v(r) = \sqrt{2GM/r}$ near the NS. One can estimate the so called Alfvén radius r_A where $E_\mathrm{B} \sim E_\mathrm{g}$ through

$$\frac{B^2(r_\mathrm{A})}{8\pi} \simeq \frac{1}{2}\rho(R_\mathrm{A})v^2(R_\mathrm{A}). \tag{3.2}$$

The magnetic field of the NS becomes dynamically important within the Alfvén radius ($r < R_\mathrm{A}$). If we further assume that the NS magnetic field is a dipole, we can write the magnetic field as $B = \mu/r^3$, where $\mu = B_\mathrm{S}R_\mathrm{ns}^3$ is the magnetic dipole moment and B_S is the magnetic field strength on the NS surface. Therefore, by requiring mass conservation, the density can be written in terms of mass accretion rate and velocity as $\dot{M} = 4\pi v(r) r^2 \rho$ (the continuity equation) and by combining the above equations we can derive the truncation radius

$$R_\mathrm{t} = k_\mathrm{A} r_\mathrm{A} = k_\mathrm{A}\left(\frac{\mu^4}{2GM\dot{M}^2}\right)^{1/7}, \tag{3.3}$$

where the "fudge factor" k_A takes into account the uncertainties in accretion geometry and it has a value of $k_\mathrm{A} \approx 0.5$ (Long et al., 2005). The truncation

radius is essentially the innermost radius where the accreting gas is lifted out of the disc plane by the magnetic field. In AMPs the mass accretion rates are such that the magnetic field strengths of NSs are strong enough to influence the accretion flow close to the stellar surface (i.e. $R_{\rm t} > R_{\rm ns}$). Therefore, the gas in AMPs is channelled onto the magnetic poles of the NS creating X-ray emitting hotspots. If the magnetic pole is misaligned from the rotational axis, we see X-ray pulsations with a period corresponding to the spin period of the NS.

Another key radius in this consideration is the co-rotation radius $R_{\rm co}$ and specifically its location with respect to the truncation radius $R_{\rm t}$. $R_{\rm co}$ is the radius where the Keplerian orbital frequency in the accretion disc equals the spin frequency of the NS, i.e. the radius where $\nu_{\rm s} = \nu_{\rm K}$ in Equation (3.1). For the ≈ 401 Hz spin frequency of SAX J1808.4–3658 (and assuming $M_{\rm ns} = 1.4\,{\rm M}_{\odot}$) we obtain roughly $R_{\rm co} \approx 31$ km. The truncation radius must be $R_{\rm t} \lesssim 1.3\,R_{\rm co}$ (Rappaport et al., 2004) or otherwise the AMP enters the "propeller" regime (Illarionov & Sunyaev, 1975), where accretion onto the NS ceases and the X-ray outburst ends.

In the most simplified picture, the angular momentum in the (assumed) Keplerian disc at $R_{\rm t}$ is transferred to the NS. As the specific angular momentum of a particle at $R_{\rm t}$ is $l = \sqrt{GMR_{\rm t}}$, by accreting mass at a rate of $\dot{M}$ onto the NS, the accretion torque can be written as

$$\tau = 2\pi I \dot{\nu}_{\rm s} = \dot{M}\sqrt{GMR_{\rm t}}, \tag{3.4}$$

where $I \approx 10^{45}$ g cm^2 is the NS moment of inertia and $\dot{\nu}_{\rm s}$ is the NS spin frequency derivative (see e.g. Pringle & Rees 1972). The accretion torque given by Equation (3.4) can be used to make estimates of the magnitude of spin-up that the NS experiences during an outburst (see e.g. Papitto et al. 2012) but there are other components that also contribute to the total torque. The magnetic field that threads the accretion disc has the largest effect (see e.g. Ghosh & Lamb 1979b; Wang 1987) and it must be taken into account as otherwise the important spin frequency derivative estimation $\dot{\nu}_{\rm s}$ is incorrect. There is still no theoretical consensus as to what is the exact magnitude of this "magnetic torque" but in general it can be computed by integrating over the magnetic stresses in the interaction region

$$\tau_{\rm m} = \int_{R_{\rm t}}^{\infty} B_{\phi} B_{\rm z} r^2 {\rm d}r, \tag{3.5}$$

where B_{ϕ} and $B_{\rm z}$ are the poloidal and toroidal field components, respectively (Wang, 1987). However, it must be kept in mind that the exact radial dependencies of B_{ϕ} and $B_{\rm z}$ are still under investigation (see e.g. Naso & Miller 2010, 2011), which makes the magnetic torque estimation challenging. Furthermore, as the radial extent of the disc-magnetosphere coupling region is

most likely limited, the integration up to infinity in Equation (3.5) is therefore a poor choice.

Earlier theoretical investigations indicated that the interaction region between the NS magnetic field and the accretion disc is large (Ghosh et al. 1977; Ghosh & Lamb 1978, 1979a,b, hereafter GL). However, Wang (1987) showed that the earlier GL models had a critical flaw in the sense that the form of toroidal field component B_ϕ assumed by GL would have caused the magnetic field pressure to completely disrupt the accretion disc beyond the co-rotation radius. Thus, Wang (1987) proposed a different expression of B_ϕ and modified the expression for the magnetic torque term acting on the NS by the gas beyond the co-rotation radius. However, the magnetic breaking term had to be further modified by the realisation that the disc-magnetosphere coupling region cannot far exceed the co-rotation radius. The rationale for this was proposed by Lovelace et al. (1995), who suggested the following scenario. As the NS magnetic field is frozen into the disc plasma, the further out from co-rotation $R_{\rm co}$ the field lines are connected to the disc, the higher the relative angular frequency difference between the field and the gas (assuming that the gas follows Keplerian orbits). Therefore, this angular frequency difference causes the field lines to be dragged "backwards" at $r > R_{\rm co}$. This causes twisting of the field lines and it thus creates a toroidal field component B_ϕ out of the poloidal field $B_{\rm z}$. The effect of the twisting is to increase the magnetic pressure above the disc, which acts to inflate the field lines (see Lovelace et al. 1995). However, it turns out that there is a critical magnetic twist of $\gamma_{\rm c} = B_\phi / B_{\rm z} \sim 1$, after which the increased magnetic pressure causes the field lines to open up (see Aly & Kuijpers 1990; Lovelace et al. 1995; Uzdensky et al. 2002a,b and Uzdensky 2004, for review).

The result is that two distinct regions appear; the closed field line region connecting the accretion disc and the NS and the open line region. In this thesis (as in Paper II), I define the magnetospheric radius $R_{\rm m}$ as the radius separating these two distinct regions. In AMP literature the magnetospheric radius $R_{\rm m}$ and the truncation radius $R_{\rm t}$ are commonly referred as the same radius, but here I make a clear distinction between them. I refer $R_{\rm t}$ as the innermost radius where the gas is lifted out of the disc plane, whereas I reserve $R_{\rm m}$ as the outermost radius where the NS magnetic field is still connected to the disc. Several authors use $R_{\rm t}$ and $R_{\rm m}$ to mean the same thing, as they generally assume that the width of the disc-magnetic field coupling region is so small that these two radii are essentially the same. In this thesis, I challenge that view. I argue that $R_{\rm m}$ and $R_{\rm t}$ are substantially different and that $R_{\rm m}$ can vary irrespectively of the mass accretion rate $\dot{M}$ (whereas $R_{\rm t}$ is determined by it), thus rendering the commonly used Equation (3.4) useless for estimations of the torques during X-ray outbursts of AMPs.

3.3 Energy spectra of AMPs

Before I go deeper into the pulsations of AMPs, I must discuss the radiative processes that produce the observed X-rays. As mentioned above, the X-ray emitting hotspots of AMPs are located at the stellar magnetic poles. The exact geometry of the emission regions is not known and such investigations must be done using MHD simulations (as in Romanova et al. 2004). Observationally, we know that the energy spectra of all AMPs are always similar, regardless of emitted luminosity (Gilfanov et al., 1998; Gierliński et al., 2002; Falanga et al., 2005; Ibragimov & Poutanen, 2009). Phenomenological description would be a power-law like spectrum with a cut-off at around 30–100 keV. In addition to this power-law like component, the model fits are improved if additional ~ 1 keV temperature black body component is added. From these considerations a Comptonization model has been developed to explain the observed spectra.

When the gas impacts the stellar surface, it decelerates very rapidly from close to speed of light to have zero translational velocity. Therefore, an accretion shock forms immediately above the stellar atmosphere. In the shock, the kinetic energy of the accretion flow is converted into thermal energy of the particles. Partly, the generated heat goes to heat the atmosphere below the shock and it emits black body radiation with about 1 keV temperature. When these soft X-ray photons pass through the shock region, which has an Thomson optical depth of $\tau_{\rm T} \sim 1$, some of them get Compton up-scattered by the hotter ~ 30–50 keV electrons in the shock, producing a power-law like Comptonized spectrum. With this physical picture, one can explain the time-averaged and time-resolved spectra of AMPs (see Figure 3.1).

In addition to the pulsating black body and Comptonized components, additional non-pulsating spectral components are present in AMPs. In time resolved and time-averaged energy spectra, one clearly sees the accretion disc with a low inner disc temperature $T_{\rm disc} \sim 0.2$ keV (see e.g., Gierliński & Poutanen 2005; Patruno et al. 2009a; Paper I; Paper II). Also clear indications of X-ray irradiation of the accretion disc are visible; spectral hardening above ~ 10 keV can be associated with a Compton reflection bump (Gierliński et al., 2002; Ibragimov & Poutanen, 2009) and at around 6.4 keV a fluorescent iron emission line(s) is(are) present, which may or may not be relativistically broadened (see Papitto et al. 2009; Cackett et al. 2009 and Ng et al. 2010, respectively).

This spectral model does not only explain the observed X-ray spectrum of AMPs but also the same components are thought to be responsible for another observed feature of the AMP pulsations. It turns out that if one extracts pulses at different energies, the soft X-ray photon band (e.g. 2.1–3.7 keV, see Paper I) pulses appear to be lagging the hard band pulses (e.g. 9.7–23.1 keV, see Paper I). These energy dependent pulse phase lags (Cui et al., 1998) – which are related to the time lags as $\Delta\phi = 2\pi\nu_{\rm s}\Delta t$ – can be understood in the same Comp-

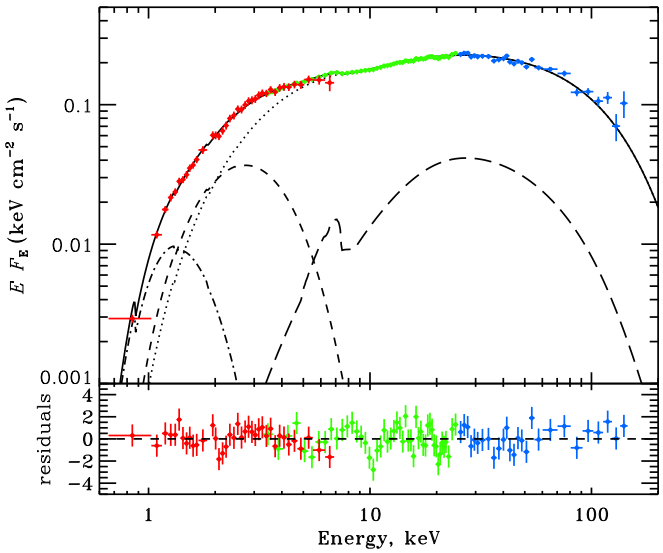

Figure 3.1. The time-averaged spectrum of IGR J17511–3057. Red, green and blue data points represent *Swift*/XRT, *RXTE*/PCA and *RXTE*/HEXTE spectra, respectively. Solid, dotted, long-dashed, dashed and dot-dashed curves represent the total model spectrum, Comptonization continuum, reflection and iron line, blackbody emission from the hotspot and the disc blackbody, respectively. The lowers panel shows the residuals of the fit. Figure from Paper I.

tonization model, which was originally proposed by Gierliński et al. (2002). The determining factor causing the lags is the difference between the angular pattern of radiation from the Comptonized shock emission and from the black body emission: the Comptonized emission is emitted in a broad, fan-like pattern, whereas the black body emission is emitted preferentially towards the surface normal in a pencil-like emission pattern (Poutanen & Gierliński, 2003). This model naturally explains why the lags increase from 2–7 keV rather monotonically and then saturates around the energy where emission from the black body component becomes negligible compared to the Comptonized emission (see Figure 3.1 and Figure 3.2). The fact that the AMP spectra, pulse shapes and phase lags can all be naturally explained with the same physical picture makes the Comptonization model a great success.

3.4 Timing noise in AMPs

The pulsar recycling scenario suggests that millisecond radio pulsars are spun-up by accretion torques during mass exchange episodes between the NS and the companion star, i.e. during X-ray outbursts when they appear as AMPs.

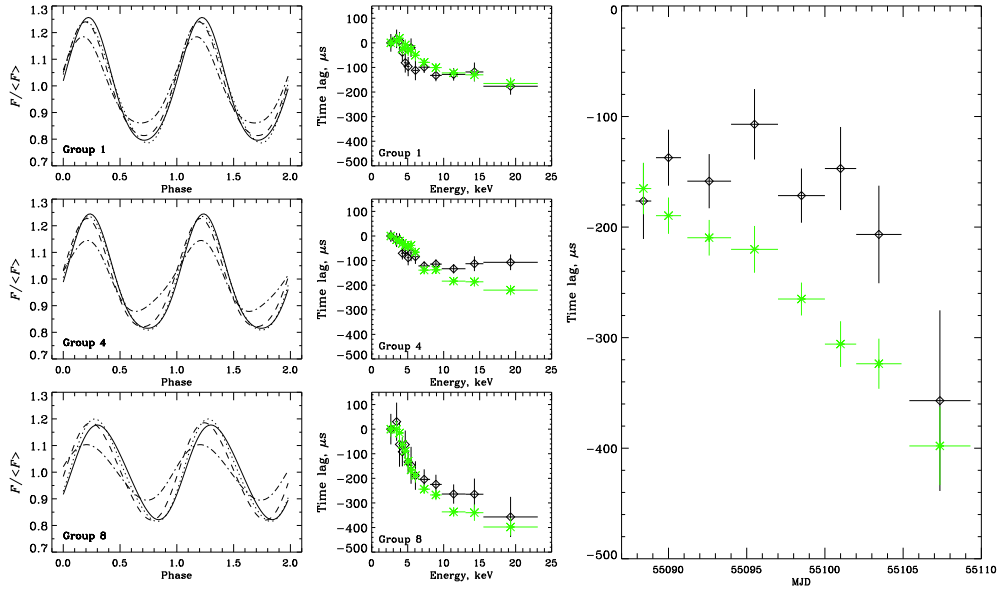

Figure 3.2. Left panels: pulse profile fits for various stages of the 2011 IGR J17511–3057 outburst with Equation (3.6) for energies 3.3–3.7 keV, 4.5–4.9 keV, 6.5–8.1 keV and 15.5–23.1 keV (solid, dotted, dashed and dash-dotted lines, respectively). Middle panels: pulse maximum lags (stars) and the lags of the fundamental (diamonds). Right panel: evolution of the lags between 2.1–3.7 keV and 15.5–23.1 keV energy bands of the pulse maximum and of the fundamental. The evolution of the time lags can be caused by a change in the anisotropy parameter h (see Paper I and Section 3.5). Figure from Paper I.

However, the measurement of spin-up (and thus the torque) is currently challenging because of the presence of X-ray timing noise.

If we fold the observed light curve with the NS spin period, we obtain a *pulse profile*. A naïve expectation would be that the pulse profiles are sinusoidal. As the star rotates about its axis the apparent size of the hotspots change and, therefore, the emitted flux towards us change. However, this picture is an oversimplification. The measured pulse profiles are not always sinusoidal and sometimes even double peaked pulse profiles are detected (Hartman et al., 2008, 2009; Ibragimov & Poutanen, 2009). The key is to understand which processes cause the pulse profiles to be non-sinusoidal. The main motivation is that the NS mass and radius are two important parameters that have a considerable effect on the shape of the pulse profiles. Therefore, the mass and radius – the two parameters we are so keen to measure – are hidden in the pulse profiles. By a good understanding of processes that influence the pulse profiles, we

can indirectly measure these most important stellar parameters.

Because the pulse profiles are non-sinusoidal, it has become common to describe them using multiple harmonics of the measured fundamental pulse frequency. Typically, only two harmonics are needed – the fundamental and the second harmonic – so that the observed flux in a selected band can be expressed as

$$F(\phi) = \bar{F}\{1 + a_1 \cos[2\pi(\phi - \phi_1) + a_2 \cos[4\pi(\phi - \phi_2)]\}, \tag{3.6}$$

where a_1, a_2 are the amplitudes and ϕ_1, ϕ_2 are the phases of the fundamental and the second harmonic, respectively.[2]

The observed pulse phases $\phi(t)$ are not stable for many reasons. In general, we can decompose the various physical causes for these pulse phase changes as follows (see Patruno & Watts 2012, for a review)

$$\phi(t) = \phi_{\rm L} + \phi_{\rm Q} + \phi_{\rm Orb} + \phi_{\rm A} + \phi_{\rm M} + \phi_{\rm N}. \tag{3.7}$$

The first term in the r.h.s. of Equation (3.7) $\phi_{\rm L}$ is the linear term and it comes from the constant spin of the NS. The second term $\phi_{\rm Q} = \frac{1}{2}\dot{\nu}t^2$ is the quadratic term caused by the constant spin-up (or spin-down) of the NS. The third term $\phi_{\rm Orb}$ is caused by the binary orbital motion; the pulse phases wander as a function of the orbital period, the semi-major axis and the inclination of the orbit. To a very high accuracy, binary orbits of AMPs are circular and a simple relation can be derived to compute these effects (see Patruno & Watts 2012, and references therein). The fourth term $\phi_{\rm A}$ describes the effect of uncertainty in the astrometric position of the AMP. The astrometric errors cause spurious pulse frequency and pulse frequency derivative offsets. For AMPs for which an optical counterpart has been detected, the astrometric position errors are small (the order of $0\farcs1$) and, therefore, the resulting offsets are negligible. However, for those AMPs without known optical counterparts, one must rely on X-ray astrometry, where the astrometric errors range from $0\farcs6$ for *Chandra* source localizations up to $3\farcs5$ for *Swift*/XRT. The fifth term $\phi_{\rm M}$ takes into account the phase fluctuations due to measurement errors. The sixth term $\phi_{\rm N}$, which is the source of the greatest uncertainty, describes the residual phase variations that cannot be explained with any of the previous terms. This term is called X-ray timing noise.

The reason why all these noise components are relevant to this thesis is that we have found evidence that part of the X-ray timing noise could be caused by changes in the way the NS magnetic field interacts with the accretion disc. However, in order to make the case, let us first look at the origins of other X-ray timing noise components so we can get a proper perspective. X-ray timing noise

[2]Note that in AMP literature, there is no consistent manner to call the harmonics, which can create confusion. Some authors call the fundamental first harmonic. Also, the second harmonic can be called first harmonic or the overtone.

actually turns out to be very important problem in AMP research. The reason for the importance is related to spurious pulse frequency and pulse frequency derivatives that can be induced by X-ray timing noise. In fact, it has been recently shown that most (if not all) reported spin frequency derivatives may actually be spurious (Patruno et al., 2009b; Patruno & Watts, 2012). Only the fastest AMP IGR J00291+5934 seems to be an exception (Falanga et al., 2005; Patruno et al., 2009b; Patruno & Watts, 2012). Therefore, it is of utmost importance to determine the root causes for the timing noise and much progress has been made in this respect in recent years.

The first indications that a change in the mass accretion rate is partially responsible for timing noise came from observations of XTE J1814–338 (Papitto et al., 2007) and XTE J1807–294 (Riggio et al., 2008). It was found that the pulse phase residuals were clearly correlated with the X-ray flux (and hence the mass accretion rate). These correlations suggest that the observed pulse frequency derivatives are not the same as the NS spin frequency derivatives: the X-ray timing noise may be almost entirely responsible for the measured pulse frequency derivatives (Patruno et al., 2009b; Patruno & Watts, 2012). This finding is most unfortunate, as we hope to see the spin-up to confirm the pulsar recycling scenario.

The reason why changes in X-ray flux can cause the pulse phase to change is actually rather easy to understand. As the flux is roughly proportional to the mass accretion rate $\dot{M}$, an increase in $\dot{M}$ would change the truncation radius (see Equation 3.3). Therefore, the gas taps onto different magnetic field lines that channel the accretion flow onto a different location of the NS surface. This causes the emitting hotspot to move on the NS surface and, therefore, the "moving hotspot model" is a natural explanation to the observed $\dot{M}$-dependent pulse phase variations (Papitto et al., 2007; Hartman et al., 2008; Patruno et al., 2009b; Lamb et al., 2009).

There are, however, several AMPs where this picture cannot explain the observations. For example, during the intensively monitored 2002 outburst of SAX J1808.4–3658 there was a drastic jump in the fundamental pulse phase in the "rapid drop" stage of the outburst, while the second harmonic phase remained constant (Burderi et al., 2006; Hartman et al., 2008; Ibragimov & Poutanen, 2009). This type of timing noise cannot be explained with the moving hotspot model. Instead, these observations were explained using a model where the secondary hotspot, that is assumed to be partially blocked from view by the accretion disc, became more visible as the truncation radius responds to the decrease of mass accretion rate (Ibragimov & Poutanen, 2009; Poutanen et al., 2009). This interpretation is also supported by analysing the time resolved spectra of AMPs (see Ibragimov & Poutanen 2009 for SAX J1808.4–3658 and Paper I for IGR J17511–3057). In both of these AMPs, we see a decline in the Compton reflection amplitude and of the iron line equivalent width (EW) when

the observed flux (and hence $\dot{M}$) drops during the outburst. These findings are consistent with the interpretation that the truncation radius $R_{\rm t}$ increases with decreasing $\dot{M}$.

Both of these timing noise components are related to variations in the mass accretion rate $\dot{M}$. However, these two components cannot fully explain the observations. The origin of $\dot{M}$-independent X-ray timing noise has lacked an explanation before our analysis of the 2008 outburst of SAX J1808.4–3658 (Paper II). In Paper II we showed that this type of timing noise could be related to $\dot{M}$-independent variations in the size of the disc-magnetosphere interaction region.

3.5 Neutron star masses and radii from AMP pulse profiles

We can obtain the masses and radii of neutron stars from the pulse profiles. As mentioned earlier, pulse profiles are extracted by folding the observed data with the stellar spin period (or with the best fitting timing solution). Typically the pulse profile is separated into 16 or 32 phase bins and we fold segments lasting one *RXTE* satellite orbit. If the pulse profile is found to be stable between the different orbits (if pulse phases and amplitudes are similar), then we co-add data from different orbits (or even from observations separated by several days) to increase the signal-to-noise ratio.

Once we have the pulse profile we need to use a physical model to describe the emission region and we need to take general and special relativistic effects into account. We have used the model developed by J. Poutanen that simulates pulse profiles with the so-called Schwarzschild-Doppler (S+D) approximation (see Miller & Lamb 1998; Poutanen & Gierliński 2003). The S+D approximation is accurate for NS spin frequencies below ~ 400 Hz and for small NS radii (see Cadeau et al. 2007; Morsink et al. 2007, for discussion). This method involves three main steps (see e.g. Poutanen & Gierliński 2003; Poutanen & Beloborodov 2006). First, one specifies the radiation spectrum and its angular dependence in a frame co-rotating with the star. Then in the second step, one makes a Lorentz transformation to obtain the radiation intensity in the non-rotating frame at the immediate vicinity of the stellar surface. Then in the third step, the photon trajectories are followed from the NS surface to the observer (located at infinity) by assuming that the space-time around the NS can be described with the Schwarzschild metric. These three steps involve special and relativistic effects and to illustrate how they influence the pulse profiles, I make use of the approximations derived by Poutanen & Beloborodov (2006) and refer the reader to Poutanen & Gierliński (2003); Cadeau et al. (2005); Poutanen & Beloborodov (2006); Cadeau et al. (2007); Ibragimov & Poutanen (2009) for the accurate formulation of these effects and for the accuracy of the used

approximations.

For very rapidly spinning stars light travel time delays become important in shaping the pulse profile. The time delays can be approximated by $\Delta t = (1 - \cos\psi)R/c$ (Poutanen & Beloborodov, 2006), where ψ is the angle between the emission region surface normal and the observers line of sight (see Figure 3.3). In Schwarzschild metric, the angle ψ can be related to the angle that the photon was actually emitted α (with respect to the local stellar surface normal) through Beloborodov's gravitational light bending approximation as (Beloborodov, 2002)

$$\cos\alpha \approx R_{\rm s}/R + (1 - R_{\rm s}/R)\cos\psi \tag{3.8}$$

and it is related to the binary inclination i, hotspot latitude θ and the pulsar phase ϕ as $\cos\psi = \cos i\cos\theta + \sin i\sin\theta\cos\phi$ (see e.g. Poutanen & Beloborodov 2006). The effect of gravitational light bending is significant on the pulse profiles as well, especially on the pulse amplitudes, which is illustrated in Figure 3.3 (compare dotted and dashed lines). Light bending alters the viewing angle of the emission region especially at phases around $\phi = 0.5$ when it would otherwise be hidden behind the star, thus decreasing the pulse amplitude.

However, the biggest effect altering the pulse profile shape comes from the special relativistic effects (Doppler shifts and aberration, see Figure 3.3). The Doppler factor δ can be approximated as (Poutanen & Beloborodov, 2006)

$$\delta \approx 1 - \beta_{\rm eq}\sqrt{1 - R_{\rm s}/R}\sin i\sin\theta\sin\phi \tag{3.9}$$

where $\beta_{\rm eq} = 2\pi R\nu/(c\sqrt{1 - R_{\rm s}/R})$ is the equatorial velocity. These relativistic effects can be taken into account to compute the emitted flux from a hotspot surface element (Poutanen & Beloborodov, 2006)

$$F_E = (1 - R_{\rm s}/R)^{\Gamma/2}\delta^{\Gamma+3} I'_E(\alpha')\cos\alpha \frac{{\rm d}\cos\alpha}{{\rm d}\cos\psi}\frac{{\rm dS}'}{D^2}, \tag{3.10}$$

where Γ is the power-law photon index (AMPs have $\Gamma \approx 2$), $I'_E(\alpha')$ is the specific intensity in the frame co-moving with the spot (primes denote values at the co-rotating frame), α' is the emission angle with respect to the surface normal in the co-moving frame (which is related to α through the aberration formula $\cos\alpha' = \delta\cos\alpha$), ${\rm dS}'$ is the spot area in the co-rotating frame and D is the distance to the AMP. In Equation (3.10), the angular dependence of the intensity can be approximated as $I(E,\alpha) = I_0(1 - h\cos\alpha)E^{-(\Gamma-1)}$, where h is the anisotropy parameter (see, Sunyaev & Titarchuk 1985; Poutanen & Gierliński 2003). For isotropically emitting source $h = 0$, whereas for the accretion shock (for a Comptonized spectrum) $h \sim 0.5$–0.8 is more appropriate (see Poutanen & Gierliński 2003; Viironen & Poutanen 2004; Poutanen 2008; Ibragimov & Poutanen 2009; Paper I; Paper II).

In addition to the relativistic effects, another important factor affecting the pulse profiles is accretion disc screening (Ibragimov & Poutanen, 2009). The antipodal hotspot can be hidden from the observer by the accretion disc. Also, an important additional factor is the shape of the NS. In our work, we have assumed that the NS is spherical. This assumption becomes less accurate with increasing NS spin frequency and radius because the rapid rotation coupled with a large radius makes the NS oblate (Morsink et al., 2007). NS oblateness affects the pulse profiles mostly because it alters the hotspot visibility and the viewing angle. NS oblateness is, however, a very tricky effect to take into account as it depends on the NS EOS, the unknown factor we are attempting to determine.

The first thing that comes to mind after looking at the equations (and the other factors) is that there are many parameters that affect the pulse profiles. The NS mass and radius are just two parameters among many and this is what I meant earlier by the forest of unknown factors. The good thing is that in several AMPs, the pulse profiles vary substantially during X-ray outbursts. These variations cannot be explained by changes in NS mass, radius nor in inclination i. Instead, the only parameters that can change during AMP outbursts are the hotspot latitude θ, the anisotropy parameter h (although AMP spectra are rather stable and, therefore, h should not vary by a large factor), the truncation radius $R_{\rm t}$ (affecting the visibility of the antipodal hotspot) and the shape and size of the emission region (see Paper II). Therefore, only by understanding the reasons for pulse profile variability in AMPs, can we improve the current M–R estimates. This is why our result in Paper II is so important as we have found one such cause. Pulse profiles are variable because of variations in the size of the disc–magnetic field coupling region, which alters the way the accretion flow is channelled onto the NS surface, causing variations in the hotspot size and possibly its shape.

3.6 Discovery of simultaneous spectral and pulse profile transition

The evidence for $\dot{M}$-independent variations in the size of the disc-magnetosphere interaction region comes from the discovery of a simultaneous spectral and pulse profile transition that was observed in the 2008 outburst of SAX J1808.4–3658 (Paper II). However, given that there is still no clear consensus of the nature of the disc-magnetosphere interaction (see e.g. Uzdensky 2004, for various plausible alternatives), let us first go through the assumptions.

Let us assume that the NS magnetic field is a dipole (so that we can make use of the equations in Section 3.2) and that the magnetic inclination – the angle between the rotational axis, which is assumed to perpendicular to the

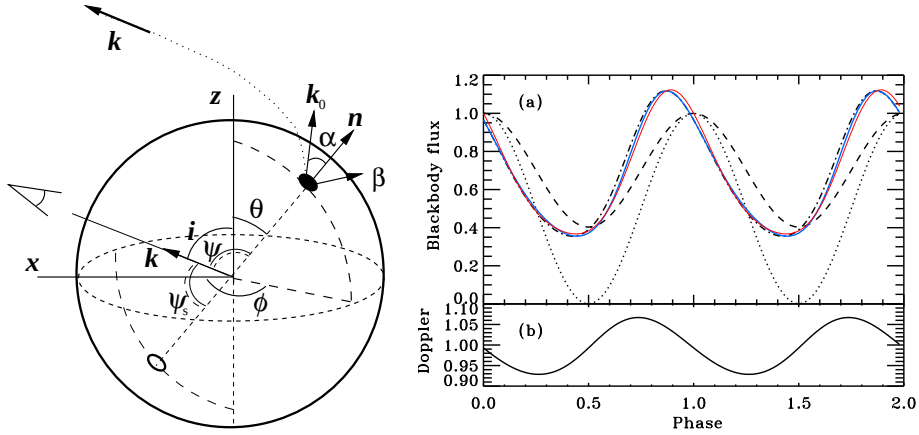

Figure 3.3. Left: Illustration of the geometrical parameters for one hotspot element. The dotted curve shows the photon trajectory, which is affected by light bending. Right: (a) The bolometric flux for an isotropically emitting hotspot as a function of the observed pulse phase for $i=\theta=45^{\rm o}$, $R_{\rm ns}=2.5R_{\rm s}$ and $M_{\rm ns}=1.4{\rm M}_{\odot}$. The dotted curve is for a slowly rotating star ignoring all relativistic effects. The pulse profile where gravitational light bending is accounted for is shown by the dashed curve. The dot-dashed curve gives the pulse profile modified by the Doppler boost and aberration for a NS rotational frequency $\nu=600$ Hz. The solid curve accounts also for the time delay. The thin solid curve is produced using the approximate formulae derived in Poutanen & Beloborodov (2006). (b) Doppler factor δ as a function of the observed pulse phase. Figures from Poutanen & Beloborodov (2006).

binary orbit and the magnetic axis – is θ (see Figure 3.4). Let us further assume that the hotspot is a ring around the magnetic pole – which is a good approximation for AMPs with small θ (Romanova et al., 2004) as in SAX J1808.4–3658 (Ibragimov & Poutanen, 2009) – and that the angles made by the inner and outer hotspot edges with respect to the magnetic axis are denoted by $\rho_{\rm in}$ and $\rho_{\rm out}$, respectively. Therefore, the gas from the accretion disc truncation radius $R_{\rm t}$ is channelled through the dipole field lines to the outer hotspot edge given by $\rho_{\rm out}$ and a relation can be derived between $R_{\rm t}$, $\rho_{\rm out}$ and θ (and analogously for $R_{\rm m}$, $\rho_{\rm in}$ and θ, see Frank et al. 2002; Poutanen et al. 2009; Paper II)

$$\sin\rho_{\rm in}=\cos\theta\sqrt{R_{\rm ns}/R_{\rm m}},\quad \sin\rho_{\rm out}=\cos\theta\sqrt{R_{\rm ns}/R_{\rm t}}. \tag{3.11}$$

Let us then assume that the radial width of the disc-magnetosphere region is substantial, extending from truncation radius $R_{\rm t}<R_{\rm co}$ up to the magnetospheric radius $R_{\rm m}\gtrsim R_{\rm co}>R_{\rm t}$. The disc-magnetic field coupling tends to bring the gas in the accretion disc to co-rotate with the stellar spin frequency in the interaction region, so that the angular frequency in the disc is similar to the angular frequency of the NS, i.e. $\omega(r)\approx\omega_*$ (Lovelace et al., 1995; Romanova

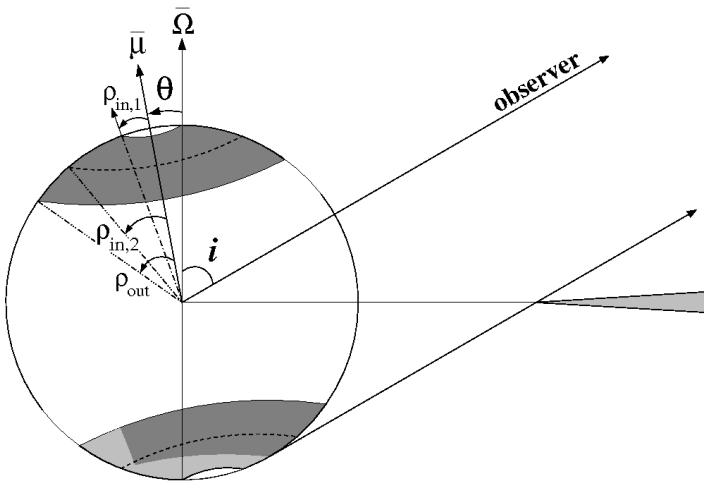

Figure 3.4. Assumed geometry of the hotspots. The magnetic dipole is inclined by angle θ to the spin axis and the co-aligned hotspots are assumed to be ring-shaped. The inner edges of the hotspots are displaced from the magnetic poles by angle $\rho_{\rm in}$ and the outer edges by $\rho_{\rm out}$. The accretion disc truncation radius, that determines which part of the secondary hotspot is hidden from view, is related to $\rho_{\rm out}$ using Equation (3.11). The pulse profile variations seen in the 2008 outburst of SAX J1808.4–3658 (see Paper II) can be modelled simply by changing $\rho_{\rm in}$, which is a function of $R_{\rm m}$ (see text). Figure from Paper II.

et al., 2002; Uzdensky, 2004). Therefore, the viscous dissipation ($\propto (r\,{\rm d}\omega/{\rm d}r)^2$, see Frank et al. 2002) within the accretion disc between $R_{\rm t} < R < R_{\rm m}$ is strongly depressed because ${\rm d}\omega/{\rm d}r$ tends to zero. Furthermore, as the Ohmic dissipation in the interaction region is also negligible for typical AMP parameters (see Paper II and Lovelace et al. 1995), we can assume that the gas in the accretion disc at radii $R_{\rm t} < R < R_{\rm m}$ does not emit much radiation. Thus, the inner disc radii we obtain from spectral fitting should correspond to $R_{\rm m}$ rather than $R_{\rm t}$.

These claims are supported by the spectral transition seen in the 2008 outburst of SAX J1808.4–3658 (reported in Paper II). In these data, we saw a substantial increase of the accretion disc luminosity at constant bolometric luminosity during the middle of the outburst, i.e. we saw that the relative fraction of the disc luminosity $L_{\rm disc}/L_{\rm bol}$ increased. The apparent inner disc radius $R_{\rm disc}$ obtained from the spectral fits decreased substantially (see Figure 3.5) and the inner disc temperature $T_{\rm disc}$ increased. As this transition happened at constant bolometric luminosity (see Figure 3.5, top panel), the increase of the disc component luminosity could not have been caused by increase of mass accretion rate $\dot{M}$ as it would have increased the bolometric luminosity.

We proposed that the sudden increase of $L_{\rm disc}$ was caused by opening of the field lines that connect the NS magnetic field to the accretion disc at $R_{\rm m}$.

All variations in the spectral parameters can be explained through this physical picture.

I. If the modelled inner disc radii correspond to $R_{\rm disc} \sim R_{\rm m}$ (rather than $R_{\rm t}$) then the substantial decrease of $R_{\rm disc}$ seen during the transition is naturally explained by opening of the field lines, i.e. a decrease of $R_{\rm m}$.

II. Similarly, an increase of $T_{\rm disc}$ seen in the transition is consistent, given that a standard accretion disc has a radial temperature dependence $T(r) \propto r^{-3/4}$ (Frank et al., 2002).

III. The increase of $L_{\rm disc}/L_{\rm bol}$ in the transition is also consistent with the interpretation. Initially, when $R_{\rm m}$ is higher, the gas within the magnetosphere does not cool efficiently and thus this energy must be released at the NS surface. When $R_{\rm m}$ decreases then $L_{\rm disc}/L_{\rm bol}$ should increase, as observed.

IV. The apparent hotspot radius $R_{\rm spot}$ also decreased, which is a natural consequence of opening of the field lines (this point is elaborated more below).

V. An increase of $T_{\rm bb}$ is also consistent with the physical picture. If $R_{\rm spot}$ decreases while $\dot{M}$ remains constant, then mass accretion rate per unit hotspot surface area increases, which leads to higher equilibrium black body temperature.

Therefore, the spectral data alone is already a rather strong argument for the proposed physical picture. However, we realised that the spectral transition occurred at the same time as the pulse profile transition (see Figures 3.5–3.7). As these transitions happened simultaneously, they must have had a common origin. The proposed field line opening can explain the simultaneous change in the pulse profile as well.

As the spectral data presented in Figure 3.5 indicates, the size of the disc-magnetic field interaction region changes, i.e. $R_{\rm m}$ decreases from $R_{\rm m} \sim 50$ km to about $R_{\rm m} \sim 30$ km. Such a drastic change can alter the way the accretion flow is channelled onto the NS surface. In fact, the field lines that connect to the accretion disc at $R_{\rm m}$ are the ones that channel the accretion flow to the inner hotspot edge, determined by $\rho_{\rm in}$ (see Equation 3.11). Therefore, in this physical picture, any variation of $R_{\rm m}$ should be reflected in a simultaneous change in $\rho_{\rm in}$, which explains the observed decrease in the apparent hotspot area (i.e. a decrease of $R_{\rm spot}$, see Figure 3.5). For a proper "test" of the proposed scenario we needed to model pulse profile transition to see whether the data supported our interpretation. We therefore investigated this in Paper II.

The pulse profiles were initially modelled using two harmonics using Equation (3.6) and the pulse amplitudes and harmonic phases were computed. From

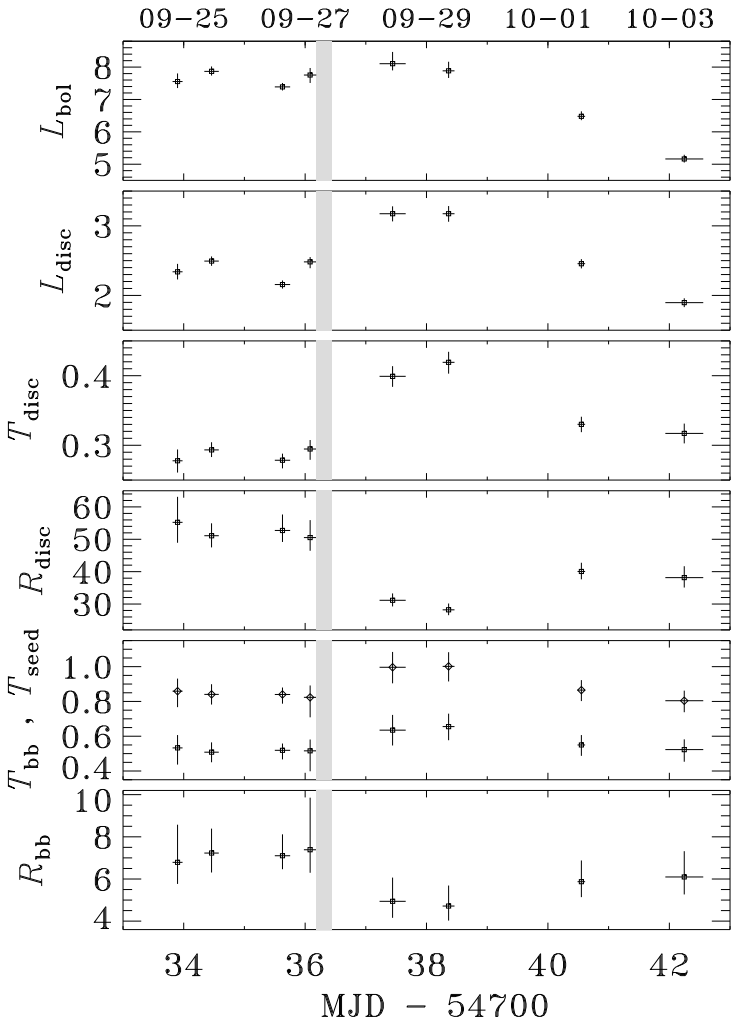

Figure 3.5. Time evolution of the spectral parameters during the 2008 outburst of SAX J1808.4–3658. Luminosities are given in units of $10^{36}\,\mathrm{erg\,s^{-1}}$, temperatures in keV and radii in km. The error bars in time axis denote the time between *Swift* and *RXTE* pointings. The grey area denotes the time period when the spectral and timing transition must have occurred (see Paper II and Figure 3.6). The spectral transition stands out as an increase of the inner disc temperature $T_{\rm disc}$, a decrease of $R_{\rm disc}$ and a change in the hotspot radius and temperature. The bolometric luminosity remains roughly constant at $L_{\rm bol} \approx 8 \times 10^{36}\,\mathrm{erg\,s^{-1}}$, which indicates a constant mass accretion rate $\dot{M}$ through the transition. Note also that the values of $R_{\rm disc}$ and $R_{\rm bb}$ are affected by systematic uncertainties. Figure from Paper II.

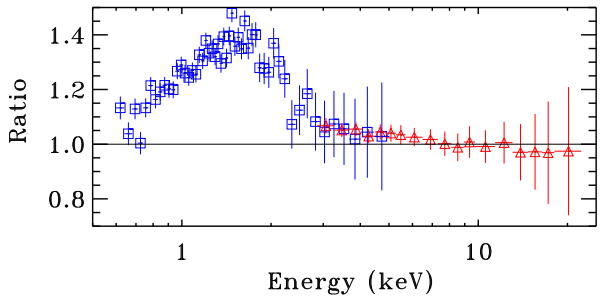

Figure 3.6. Ratio of the spectra from observations after and before the timing transition during the 2008 outburst of SAX J1808.4–3658. The increase of the flux is most evident below ~ 3 keV, where the accretion disc component dominates (see Patruno et al. 2009a and Fig. 3.8). Figure from Paper II.

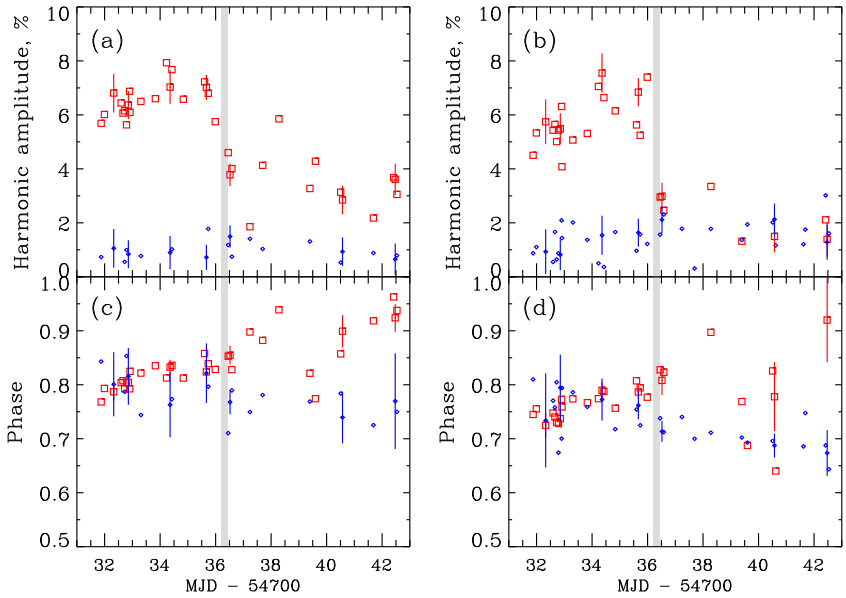

Figure 3.7. Change of the pulse profile parameters during the 2008 outburst of SAX J1808.4–3658. Left panels are for the 3.7–5.7 keV band, while the right panels are for the 9.8–23.2 keV band. Upper panels present amplitudes of the fundamental (red squares) and of the first harmonic (blue diamonds). Lower panels correspond to the pulse phases shown by the same symbols. The time of the spectral transition is marked with the grey shaded strip (see Fig. 3.6). Figure from Paper II.

these model fits we could easily see that the timing transition occurred simultaneously to the spectral transition (see Figure 3.7, and also Paper II). We extracted the pulse profiles from *RXTE*/PCA data before and after the transition in the 9.8–23.2 keV band, where only the Comptonized component contributes to the emission. As $\dot{M}$ was constant, we used the assumption that $R_{\rm t}$ was constant for both pulses. We made several tests to make sure that the anisotropy parameter h did not vary substantially during the transition. This was expected as the spectral shape – which fundamentally determines h – did not vary during the transition and, therefore, we assumed that h did not vary during the transition. We also assumed that the hotspot shape is a ring around the magnetic axis and assumed that the hotspot centroid did not vary (so that the magnetic inclination θ was constant). The former assumption is most probably valid for small value of $\theta \lesssim 15^{\rm o}$ (Romanova et al., 2004) and the latter is consistent with the fact that pulse phases remained constant during the transition (see Figure 3.7). The accretion disc screening (Ibragimov & Poutanen, 2009) is crucial to model the pulse profile after the transition: I could not produce the correct pulse profile shape without it. I suspect that this is most likely the reason why Morsink & Leahy (2011), who do not take disc screening into account in their analysis, chose not to use the 2008 outburst pulse profiles of SAX J1808.4–3658 in their analysis.

The results of the pulse profile modelling fully supported the proposed physical picture. We found that the pulse profile transition can be produced only by varying the inner hotspot edge from $\rho_{\rm in} < 12^{\rm o}$ to $\rho_{\rm in} = 31^{\rm o} \pm 2^{\rm o}$ during the transition. This is exactly what is expected in the proposed physical picture. The field lines that connect the gas in the accretion disc at $R_{\rm m}$ channel the accretion flow to the surface of the star given by $\rho_{\rm in}$. Furthermore, the parameters for the other unknown variables were consistent with the previous constraints. The inclination was roughly $i \approx 60^{\rm o}$, which was consistent with previous independent estimations (Deloye et al., 2008; Ibragimov & Poutanen, 2009). The anisotropy parameter $h \approx 0.57$ was consistent with the value expected for a Comptonized spectrum of optical depth $\tau \approx 1$ (Poutanen 2008; Paper II), which was observed in the time averaged spectra. The magnetic inclination was $\theta \approx 10^{\rm o}$, which is consistent with the assumption that the hotspots are ring-shaped (Romanova et al., 2004) and it was also similar to previous constraints (Ibragimov & Poutanen, 2009). Finally, the results showed that the truncation radius was $R_{\rm t} \approx 20$ km, which is within the co-rotation radius of $R_{\rm co} \approx 31$ km for SAX J1808.4–3658.

Therefore, our results suggest that the size of the interaction region between the magnetic field and the accretion disc in SAX J1808.4–3658 is substantial. Furthermore, our results indicate that the size of this region is variable in time and the changes occur irrespectively of changes in the mass accretion rate. In my view, these results give the first observational evidence that the disc-

magnetosphere interaction in AMPs is highly dynamic.

3.7 Discussion

In Paper II, we also speculated why the field lines opened during the outburst. According to Rappaport et al. (2004), $R_{\rm m}$ can exceed the co-rotation radius only by 30 per cent before accretion is stopped by the centrifugal barrier. We speculated that this might provide the limiting value for $R_{\rm m} \sim 50$ km before the transition. Then, the sudden opening of the field lines (decrease of $R_{\rm m}$) could be caused by a change in the properties of the accretion flow. In the Lovelace et al. (1995) model, the location of $R_{\rm m}$ is fundamentally determined by the critical twist $\gamma_{\rm c} = B_\phi/B_z = -Hr(\omega(r) - \omega_*)/\eta_{\rm t}$, where H is the disc height and $\eta_{\rm t}$ is the magnetic diffusivity. As $\gamma_{\rm c} \approx 1$ is thought to be a constant (e.g. Uzdensky et al. 2002a,b), a change in the magnetospheric radius $R_{\rm m}$ – for a fixed $\dot{M}$ – could be caused by a change of $\eta_{\rm t}$ in the accretion disc. Furthermore, as the diffusivity $\eta_{\rm t}$ is most likely caused by the same MHD turbulence that produces the viscosity $\nu_{\rm t}$ (so that $\eta_{\rm t} \sim \nu_{\rm t}$, Fromang & Stone 2009) we speculated that the observed spectral- and pulse profile transition were related to changes of viscosity in the accretion disc. Recent MHD simulations have shown that if the magnetic Reynolds number ($= c_{\rm s}H/\eta_{\rm t}$) is below a certain critical value, the MRI (Balbus & Hawley, 1998) that is believed to be responsible for the angular momentum transport in the accretion disc might quench, possibly causing high- and low viscosity states (Simon et al., 2011). Perhaps, the magnetic field configuration therefore responded to changes in the viscosity of the disc. However, these are mere speculations and they must be investigated through MHD models, but such investigations are well beyond the scope of this thesis.

The results that we obtained in Paper I and especially in Paper II have many interesting consequences. For future studies, the most important result is the identification that hotspot size and shape variations – caused by the dynamic disc-magnetosphere interaction during AMP outbursts – can lead to pulse profile changes. Clearly, many follow-up investigations and re-analysis of archived data of SAX J1808.4–3658 and other AMP outbursts can be performed to look for similar events. In fact, during the 2011 outburst of SAX J1808.4–3658, we triggered a *Swift* target of opportunity (ToO) observations to complement the already triggered *RXTE* ToO program, in order to see if a simultaneous spectral-timing transition could be seen as in the 2008 outburst. Unfortunately, because of observing constraints (SAX J1808.4–3658 was too close to the Sun during the outburst for *Swift*), our ToO observations could only cover the beginning of the outburst and a pulse profile transition (seen in *RXTE*/PCA data) occurred only 2 days after our last *Swift* observation (Kajava et al., in preparation). We

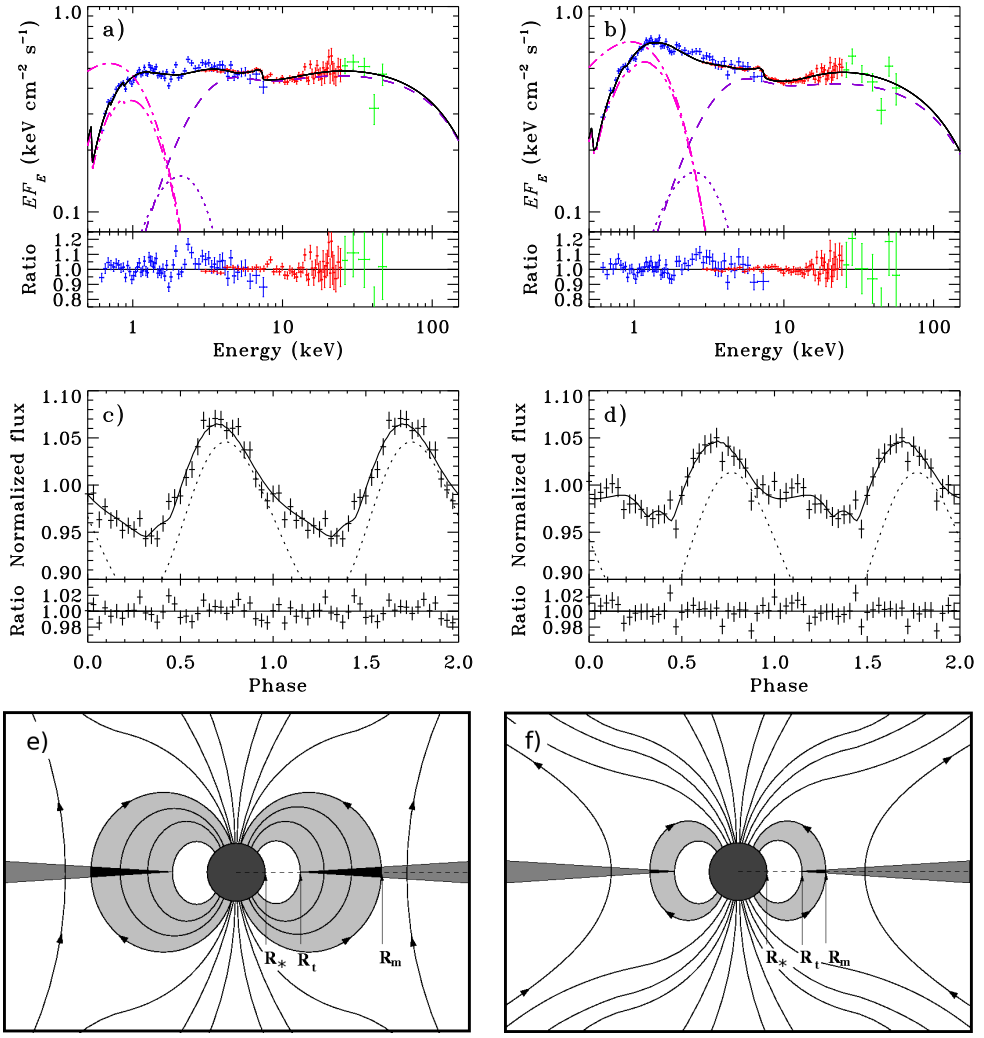

Figure 3.8. Photon spectra before the transition and after the timing transition during the 2008 outburst of SAX J1808.4–3658 are shown in the top panels (a) and (b), respectively. The blue, red and green data points are for *Swift*/XRT, *RXTE*/PCA and *RXTE*/HEXTE, respectively. The solid black line shows the model spectrum. The pink dot-dashed line is the unabsorbed disc component and the three-dot-dashed line the absorbed disc component. The purple dotted line is the NS blackbody component, whereas the dashed line is the Comptonized component. The weak Compton reflection and the iron line components are below the plotting range. Pulse profiles before the transition and after the transition are shown in the middle panels (c) and (d), respectively. The solid line is the contribution from both spots, whereas the dotted line shows the contribution of the "main" spot. Lower panels illustrate the geometry of the disc–magnetosphere interaction region before (panel e) and after (panel f) the transition. Figures from Paper II.

could not therefore investigate if the pulse profile transition (Patruno et al., 2012) was accompanied by a similar spectral transition below ~ 3 keV as in the 2008 outburst. However, there are clear indications of similar spectral and timing transitions in archived *RXTE*/PCA data. In the very beginning of the 2002 outburst of SAX J1808.4–3658, there was a clear pulse profile transition, which Ibragimov & Poutanen (2009) marked as a transition from the "peak" outburst stage to the beginning of the "slow-decay" stage. If one compares their figures 2, 6 and 7, a clear spectral hardening is present below ~ 4 keV during the pulse profile transition. Ibragimov & Poutanen (2009) proposed that this pulse profile transition was caused by a change in the absorption of the hotspot radiation by the "accretion stream" (at higher $\dot{M}$, the stream can be marginally optically thick, see Ibragimov & Poutanen 2009), but I instead suggest here that it was caused by a change in the disc-magnetosphere coupling. However, the transition seems to occur in the opposite way compared to the 2008 outburst, in the sense that the pulse profile becomes more sinusoidal (second harmonic amplitude drops while fundamental increases, see figure 6 in Ibragimov & Poutanen 2009). I therefore speculate, that this event was caused by a major reconnection event of the open field lines back to the accretion disc, i.e. a large increase of the magnetospheric radius $R_{\rm m}$. Furthermore, during the 2005 outburst of SAX J1808.4–3658 one sees a similar looking event as in the 2002 data (see figure 1 and 3, in Hartman et al. 2008). During the peak of this outburst, the pulse profile changes in a very similar fashion to the 2008 outburst. However, as Hartman et al. (2008) did not analyse the energy spectra, it cannot be confirmed whether a spectral softening was present in these data. A curious similarity between these sudden $\dot{M}$-independent pulse profile transitions during SAX J1808.4–3658 outbursts is that they seem to occur at very comparable luminosities in all 2002, 2005, 2008 and 2011 outbursts (see Hartman et al. 2008; Ibragimov & Poutanen 2009; Paper II; Patruno et al. 2012). It is not presently clear if this is only a coincidence or if there is some physics behind it.

The identification of other similar events to the 2008 outburst transition is very important. If many similar cases are identified and confirmed, the strength of the argument presented in this thesis (and in Paper II) is substantially increased. The downside in analysing the previous outbursts is that there is no *Swift*/XRT data to see the emission below ~ 3 keV (except during the end of the 2005 SAX J1808.4–3658 outburst, see Campana et al. 2008), where the spectral transition is expected to be the most prominent. However, *RXTE* calibration has been improving towards the end of the mission (Shaposhnikov et al., 2012) so perhaps with the new improved calibration data, the spectral transition are not only seen in the lowest spectral channels of *RXTE*/PCA, but that the results are also believed by the community!

By re-analysing the data from these events, we will most certainly obtain better NS M–R constraints. By having the physical picture obtained in Paper

II, we can make use of these data sets to simultaneously fit them. The pulse profiles seem to be considerably different (see Hartman et al. 2008; Ibragimov & Poutanen 2009), so by having more data sets in the fitting, only certain values of the other unknown parameters (i, θ, h) will be valid for all the pulses. Therefore, uncertainties in M and R parameter confidence intervals will be greatly reduced and perhaps we will get already meaningfully tight constraints, so that we can infer the correct NS model. In Paper II, we did not try to constrain M and R, but our initial tests already indicated that only by using the two pulse profiles, low NS radii below ~ 10 km could be excluded (result not published). For this reason we used $R_{\rm ns} = 11$ km and $M_{\rm ns} = 1.4\ {\rm M}_{\odot}$ for the pulse profile modelling. For NS masses larger than $1.4\ {\rm M}_{\odot}$, the NS radii was always seen to increase, up to the point where for a $2\,{\rm M}_{\odot}$ NS (which is the mass of the most massive neutron star known, see Demorest et al. 2010) radii of about $R_{\rm ns} \approx 14 \pm 1$ km were needed. The increase of NS radius for a larger mass is understandable as many relativistic effects affecting the pulse profiles, such as light bending, depend on M/R. However, before making the important M–R constraints, we need to first properly establish that our assumptions and interpretations are valid. Otherwise, if we make such strong claims on not that solid basis, the main message – that the disc magnetosphere coupling in AMPs seems to be variable during outburst – could be ignored by the interested community. Therefore, the upcoming aim of our work is to fully establish the proposed scenario for SAX J1808.4–3658 and other AMPs and later on to make use of these results to place constraints on the NS EOS.

Although the M–R constraints must be left to future work, the present results already have several interesting consequences on our understanding of X-ray timing noise. As mentioned earlier, X-ray timing noise makes the spin-up torque measurements currently challenging, because the observed pulse frequency derivatives differ from the NS spin frequency derivative $\dot{\nu}_{\rm s}$ (Patruno et al., 2009b; Patruno & Watts, 2012). Although the currently available models for X-ray timing noise – the moving hotspot model (e.g. Patruno et al. 2009b; Lamb et al. 2009) and changes in the disc screening (Ibragimov & Poutanen, 2009; Poutanen et al., 2009) – can explain the $\dot{M}$-dependent X-ray timing noise, these models cannot explain the $\dot{M}$-independent timing noise. The $\dot{M}$-independent changes in the disc magnetosphere coupling – and the resulting changes in the accretion flow onto the NS – can, in my view, change the size and the shape of the emitting hotspots and, therefore, cause X-ray timing noise. Even small changes in the hotspot latitude can cause large phase jumps (see Lamb et al. 2009; Paper II, for discussion). This mechanism might be responsible for the X-ray timing noise not only for SAX J1808.4–3658, but for other AMPs too. Especially the $\dot{M}$-independent timing noise for IGR J17511–3057 (Paper I), XTE J1807–294 and XTE J0929–314 (see figure 3 in Patruno et al. 2009b) might well be caused by the disc-magnetospheric interaction mecha-

nism. However, the high Galactic extinction towards IGR J17511–3057 (and some other AMPs) causes most of the disc radiation to be absorbed in the ISM, severely hampering the detection of disc variations. Now, in the post-*RXTE* era, the best hope for future detections simultaneous spectral- and pulse profile transitions is the Indian *ASTROSAT* mission (which has been about to be launched for many years now), which host two instruments (SXT and LAXPC) that have very similar capabilities than *Swift*/XRT and *RXTE*/PCA. Hopefully, this satellite is launched before the next anticipated SAX J1808.4–3658 outburst during 2013–2014.

Another very interesting AMP for future studies is Swift J1749.4–2807 (Markwardt & Strohmayer, 2010; Ferrigno et al., 2011; Altamirano et al., 2011). This is the first eclipsing AMP, for which inclination has been determined very accurately ($i \approx 75^{\rm o}$–$77^{\rm o}$). This constraint is a lot more restrictive than for SAX J1808.4–3658, for which inclination of $i = 36^{\rm o}$–$67^{\rm o}$ has been determined from optical observations (Deloye et al., 2008). However, the spin frequency of Swift J1749.4–2807 is about $\nu_{\rm s} \approx 518$ Hz. For such rapidly spinning AMPs, the accuracy of our S+D approximation is less accurate than for SAX J1808.4–3658, because the rapid spinning can cause the NS to be oblate (Cadeau et al., 2007; Morsink et al., 2007). The oblateness of the NS is not accounted for in our simulations and thus accuracy of any M and R constraint would be compromised for this rapidly spinning AMP. Furthermore, recent results from X-ray burst observations (see Suleimanov et al. 2011; Kajava et al., in preparation; Poutanen et al., in preparation) seem to favour high NS radii of $R_{\rm ns} \gtrsim 14$ km for masses below $M_{\rm ns} \lesssim 2\,{\rm M}_{\odot}$. This compounds the oblateness problem even further, as NS become more oblate for higher NS radii (Cadeau et al., 2007; Morsink et al., 2007).

Another important consequence of our results is related to accretion torque estimates during X-ray outbursts of AMPs. It is popular to use a modified version of Equation (3.4), where the accretion torque is simply multiplied by yet another fudge factor to hide the uncertainties in the disc-magnetosphere interaction (see e.g. GL; Psaltis & Chakrabarty 1999; Hartman et al. 2008). This type of technique is appealing, as one hides all the relevant physics into one small parameter. However, if the disc-magnetosphere interaction region is variable during AMP outbursts – as our results seem to indicate – then this type of approach loses its purpose. It makes no sense to try to find the value of the small fudge factor parameter, if it is not a constant over time. Very similar criticism has been put forward by Li & Wickramasinghe (1998) and Agapitou & Papaloizou (2000), who also suggest that a dynamic disc–magnetosphere interaction region is needed to explain the spin-up and spin-down phases of X-ray pulsars. Thus, our results support the arguments that spin-up torques are not simple functions of the mass accretion rate. However, a big difference between the slowly spinning X-ray pulsars and AMPs is that in the latter case we can

actually see the accretion disc emitting in the soft X-ray band, whereas in the X-ray pulsars we can only measure the pulse phase evolution and the flux emitted by the hotspots. Therefore, AMPs should provide better test cases to investigate these disc–magnetosphere variations than X-ray pulsars in future studies.

Chapter 4

Ultraluminous X-ray sources

4.1 Nature of ULXs: is black hole mass the key factor?

An ultra-luminous X-ray source (ULX) is by definition a point-like (unresolved) extragalactic X-ray source, located outside the host galaxy nucleus – so that active galactic nuclei (AGN) are excluded from the definition – with the observed (isotropic) X-ray luminosity in excess of $L_{\rm x} \sim 10^{39}\,{\rm erg\,s^{-1}}$ (see Figure 4 and Feng & Soria 2011, for review). The most common interpretation is that ULXs are accreting black holes, because of the relatively fast variability detected in them (Okada et al., 1998), which suggests that the emission region is compact. The limiting luminosity is not well defined by the ULX community: different authors use values between $L_{\rm x} = 1-3\times10^{39}\,{\rm erg\,s^{-1}}$. The luminosity of $L_{\rm x}=3\times10^{39}\,{\rm erg\,s^{-1}}$ is probably the most natural limiting definition value, as it is close to the Eddington limit for the most massive stellar-mass black hole (StMBH) $M_{\rm bh}\sim30\,{\rm M_\odot}$ confirmed by dynamical mass measurements (Prestwich et al., 2007; Silverman & Filippenko, 2008).[1] Although ULXs have been detected already since the *Einstein* mission, operational from November, 1978 to April, 1981 (Long & van Speybroeck 1983; Fabbiano 1989), we do not know why they are so luminous.

The reason why ULX are called the way they are is rather obvious, if we write the observed ULX luminosity as in Feng & Soria (2011)

$$L \approx \frac{1.3\times10^{38}}{b}\dot{m}\left(\frac{M}{\rm M_\odot}\right)\,{\rm erg\,s^{-1}}\,,\ \dot{m}\lesssim1 \qquad (4.1)$$

$$L \approx \frac{1.3\times10^{38}}{b}\left(1+\frac{3}{5}\ln\dot{m}\right)\left(\frac{M}{\rm M_\odot}\right)\,{\rm erg\,s^{-1}}\,,\ 1\lesssim\dot{m}\lesssim100 \qquad (4.2)$$

(see Shakura & Sunyaev 1973; Poutanen et al. 2007), where b is the beaming

[1] Note also that the maximum possible BH mass that can be formed from a collapse of a massive star having solar metallicity is also similar to this value (Belczynski et al., 2010).

Figure 4.1. False-colour image of the Antennae galaxies (NGC 4038/4039). Optical emission is shown in yellow colours, which comes from billions of stars in the two colliding galaxies. The infra-red emission taken with the *Spitzer* space telescope tracks the dust emission. The blue haze is X-ray emission and it originates partly from the heated interstellar gas, emission from coronae of billions of low-luminosity stars and from other low-luminosity X-ray emitting objects. The brightest, blue, point-like objects are ultra-luminous X-ray sources. Credits, X-ray: NASA/CXC/SAO/J.DePasquale; IR: NASA/JPL-Caltech; Optical: NASA/STScI.

factor (King et al., 2001; King, 2009) and $\dot{m} \equiv \eta \dot{M} c^2 / L_{\rm Edd}$ is the Eddington normalized accretion rate (here $\eta \sim 0.1$ is the accretion efficiency and $L_{\rm Edd}$ is the Eddington limit, see Equation 1.4). Therefore, from Equation (4.1) and Equation (4.2) we can see that if ULXs are powered by accretion onto typical $\sim 10\,{\rm M}_{\odot}$ StMBHs they must be super-Eddington with $\dot{m} > 1$ and this is why ULXs are called ultra-luminous X-ray sources. This realisation bothers many astronomers, as a spherically symmetric star that is powered by spherical accretion must obey the Eddington limit. Therefore, many argue that ULXs are powered by sub-Eddington ($\dot{m} < 1$) accretion onto intermediate-mass black holes (IMBHs, see e.g. Colbert & Mushotzky 1999) with masses in the range between $\sim 100\,{\rm M}_{\odot}$ and $\sim 10^5\,{\rm M}_{\odot}$. However, it must be kept in mind that the Eddington limit is a "flexible limit" for disc accretion in a binary system, partly because the accretion disc (by definition) is not spherically symmetric. Therefore, ULXs might as well be powered by super-critical (i.e. super-Eddington) accretion onto typical StMBHs (with masses $\sim 10\,{\rm M}_{\odot}$), where heat advection (Abramowicz et al., 1988) and massive accretion disc winds/outflows (Shakura & Sunyaev, 1973) can simultaneously play key roles in shaping the accretion flow and the observed spectrum, capable of producing super-Eddington luminosities (as seen from Equation (4.2); Poutanen et al. 2007). Because for a given ULX it is difficult to determine from X-ray data alone which of these two interpretations is correct, this StMBH vs. IMBH debate has been going on for a long time (see e.g. Komossa & Schulz 1998).

If ULXs were IMBHs, they would be the missing link between the $M_{\rm bh} \sim 10\,{\rm M}_{\odot}$ StMBHs population seen in the Galaxy (McClintock & Remillard, 2006) and the super-massive black hole (SMBH; $M_{\rm bh} \sim 10^6 - 10^{10}\,{\rm M}_{\odot}$) population in the centres of galaxies (e.g. Ferrarese & Ford 2005). IMBHs are thought to be population III stars, meaning that they have been formed with (or from) the first stars in the universe (Madau & Rees, 2001). Alternatively, IMBHs can be formed by runaway collisions (or mergers) of stars in dense star clusters (Portegies Zwart et al., 2004). Potentially, therefore, if ULXs are indeed IMBHs, they could help us understand how the more massive SMBHs have grown to have their large masses during the evolution of the universe (Ebisuzaki et al., 2001). As SMBHs have strong influence in the formation and evolution of entire galaxies through various feedback mechanisms (Di Matteo et al., 2005), understanding the formation and mass growth of IMBHs has also significant cosmological importance.

Alternative models to these two scenarios exist though. ULX may not be intrinsically as luminous as they seem, i.e. the emission may be beamed toward our line of sight by a relativistic jet, much like in blazars (Ghisellini et al., 1993) and, therefore, the observed luminosity would not represent the true intrinsic luminosity. However, these relativistic beaming models (Reynolds et al., 1997; Okada et al., 1998; Körding et al., 2002) have been shown to be incon-

sistent with observational properties in some well-studied ULXs (see following Sections). Other possible explanations for the high luminosities of ULXs include that they are young pulsars (Perna et al. 2008; Medvedev & Poutanen, in preparation), or extraordinarily luminous X-ray supernovae (Immler & Lewin, 2003). Although the majority of ULXs are most likely not these latter type systems – as X-ray supernovae fluxes should decay in time, contrary to what is observed (Kajava & Poutanen 2008; Feng & Kaaret 2009; Paper III) and no coherent pulsations are detected in ULXs (with one possible exception, see Trudolyubov 2008)[2] – it must be kept in mind that some ULXs might be these exotic objects, some ULX might be IMBHs while others are StMBHs and, therefore, as a class ULXs are most likely a heterogeneous group of systems.

The ULX research field has exploded with the launch of *Chandra* and *XMM-Newton* at the turn of the millennium. These two satellites have detected hundreds of ULXs in nearby galaxies (Liu, 2011; Walton et al., 2011; Swartz et al., 2011) – more than a factor of five increase compared to the *Rosat* satellite ULX candidate detections (Liu & Bregman, 2005) – having luminosities up to staggering $L_{\rm x} \sim 10^{42}\,{\rm erg\,s^{-1}}$ (Farrell et al., 2009), i.e. the luminosity of hundreds of millions of Suns!

Our interest in ULXs comes from the potential of finding the most massive BHs that can be formed from evolution of stars. But because ULXs reside in distant galaxies and therefore they are observationally faint both in X-ray- and optical bands, the more traditional mass measurement techniques cannot be applied to them. Only very recently, unsuccessful optical spectroscopic campaigns to measure the mass function through radial velocity changes were attempted on two ULX optical counterparts (Roberts et al., 2011). Therefore, astronomers are desperately searching for alternative BH mass proxies, preferably utilising observations in the X-ray band where ULXs are most easily observable. One approach is to find similarities between Galactic black holes binaries (BHB), AGNs and ULXs, and then use some spectral or timing property that scales with the BH mass to infer the nature of ULXs.

In this section, I will present our results on ULXs that were published in three articles, referred as Paper III, Paper IV and Paper V. In our investigations, we concentrated on looking for these aforementioned similarities between ULXs, BHBs and to some extent, AGNs. Much like in our AMP work, our aim was to find ways to estimate masses of the BHs that power ULXs in the hopes of finding the best IMBHs candidates and, at the same time, to find observational signatures of super-Eddington accretion onto StMBHs.

[2]It is possible that the object found by Trudolyubov (2008) is a low luminosity foreground system instead of an ULX located within the putative host galaxy NGC 1313.

4.2 Optical observations of the ULX population

4.2.1 Optical counterparts of ULXs

Although in our work we have concentrated on X-ray studies of ULXs, many important clues to the nature of ULXs have been obtained from optical observations of the ULX population. As mentioned earlier, optical counterparts of ULXs are all very faint with optical magnitudes ranging from $m \sim 21$ to $m \sim 24$ (see Ptak et al. 2006; Tao et al. 2011, and references therein). Although some of these counterparts are in the reach of the 10 meter class telescopes for optical spectroscopic radial velocity measurements, one needs to first identify orbital periods before time-consuming campaigns are ever granted for these telescopes. What seems to be discouraging is that the best candidate ULX for such measurements, NGC 1313 X-2, had more than 6σ detection of ~ 6 day periodicity (Liu et al., 2009), which subsequently reduced to a 3σ detection when more data was added (Zampieri et al., 2012), suggesting that the proposed orbital period might be spurious. If the optical emission does not come from a companion star – but instead from an irradiated accretion disc (Patruno & Zampieri, 2010; Impiombato et al., 2011; Tao et al., 2011) or alternatively from an optically thick disc outflow (Poutanen et al., 2007) – it is no wonder why Roberts et al. (2011) did not find any signs of the putative orbital modulation in their spectroscopic data.

Another ULX, NGC 5408 X-1, showing clear 115 day X-ray modulations – which Strohmayer (2009) tentatively identified as the orbital period – is a good target for optical observations. It is not clear, however, if the 115 day modulation is the orbital period. An alternative interpretation by Foster et al. (2010) suggests that the periodicity could be instead super-orbital in nature, making NGC 5408 X-1 similar to the Galactic SS 433 system, the only Galactic binary believed to be accreting well in excess of the Eddington rate (see Fabrika 2004; Medvedev & Fabrika 2010, and references therein). The results from the spectroscopic study by Cseh et al. (2011) are also suggestive that NGC 5408 X-1 cannot at the same time have a 115 day orbital period and host a $\sim 1000\,\mathrm{M}_\odot$ IMBH, contrary what has been proposed by Strohmayer & Mushotzky (2009) and Strohmayer (2009). Thus further observations of this object in the optical band can provide very interesting results, but the 115 day periodicity means that an observational campaign lasting many years is needed. Such campaign would be very valuable, as the results could have the potential to provide the BH mass powering this particular ULX.

Perhaps the most fascinating source is also the most luminous ULX, ESO 243–49 HLX-1, reaching stupendous luminosities of $L_\mathrm{x} \sim 10^{42}\,\mathrm{erg\,s^{-1}}$ (Farrell et al., 2009).[3] This system also shows clear ~ 370 day X-ray modulation,

[3] This source is called hyper-luminous X-ray source and therefore it is named HLX-1. However,

which is most likely the orbital period of the system.[4] The discovery of the optical counterpart of ESO 243–49 HLX-1 raised an interesting question: the optical colours and X-ray spectral properties could have been also explained as a foreground X-ray binary with a low-mass late type star orbiting a neutron star primary (Soria et al., 2010). If this alternative interpretation were to be correct, ESO 243–49 HLX-1 would have been downgraded from being the most luminous X-ray binary ever detected to being perhaps one of the least interesting systems for which the discovery was published in the Nature magazine. Fortunately, however, the red-shift measurement from the Hα emission line placed the optical counterpart strictly to the host galaxy (Wiersema et al., 2010), thus confirming that the source is indeed a ULX. Further optical observations using both VLT and HST showed that the $m_v \sim 24 - 25$ optical counterpart is variable: the results indicated that the emission comes mainly from an irradiated accretion disc, with an additional contribution from an unresolved cluster young stars and the host galaxy (Farrell et al., 2012; Soria et al., 2012). Therefore, given that the optical emission is contaminated (Farrell et al., 2012; Soria et al., 2012), any optical spectroscopic campaigns will be even more "risky" than for NGC 5408 X-1.

Even though many interesting results from optical observations of ULXs have been obtained, these observations have not yet provided any clear answers to the question of what are the BH masses powering ULXs. However, only one clear radial velocity measurement determining the mass of an IMBH would be enough and I believe that future studies of ULXs in the optical band will most certainly resolve the StMBH vs. IMBH debate. In the meanwhile, other BH mass estimation methods must be used.

4.2.2 Emission line nebulae around ULX

In addition to the unresolved optical counterparts, some ULX also have spectacular extended emission line nebulae around them (Pakull & Mirioni, 2002, 2003). Some of these ULX nebulae are powered by photo-ionisation from the UV/X-ray emission of the ULX itself, whereas other ULX nebulae are shock-ionised by outflows and/or jets from the central source (Pakull & Mirioni, 2002, 2003; Kaaret et al., 2004; Abolmasov et al., 2007). Some of these nebulae produce radio emission as well (Kaaret et al., 2003) and their properties closely

in this thesis I call it a ULX to avoid confusion.

[4]The credit for the discovery of the ~ 370 day periodicity is problematic to give, mostly because of the NASA policy of not having a proprietary period for *Swift* data. The first hints of the periodicity were visible already in 2010 (Godet et al., 2010) and the confirmation came when the 2011 outburst started. The discovery was first reported by Kong (2011) using the data from the observing program organized by Godet et al. (2011) who reported the discovery a day later.

resemble the Galactic SS 433 system (see Dubner et al. 1998; Abolmasov 2011; Cseh et al. 2012), which is thought to be a super-Eddington accreting StMBH. As the super-Eddington StMBH models for ULXs predict strong disc outflows (Poutanen et al., 2007), the presence of shock-ionised ULX nebulae is naturally explained in this context. Because IMBHs are not expected to launch strong outflows at sub-Eddington accretion rates, these ULX nebulae therefore favour the StMBH scenario at least for those ULXs that have detectable nebulae around them (Poutanen et al., 2007; Abolmasov, 2011).

The ULX nebulae that are powered by photo-ionisation are equally important in determining the nature of ULXs. The main result from analysis of these nebulae has been to exclude the relativistic beaming models for ULXs. For these ULX nebulae can be used as "calorimeters", meaning that one can use the optical emission line fluxes to estimate the photo-ionising UV/X-ray flux from the central source. One of the best diagnostic is the He II λ4686 emission line. Kaaret et al. (2004) and Lehmann et al. (2005) used this technique on the extended He II λ4686 nebula around the famous ULX Holmberg II X-1. They determined that the isotropic X-ray luminosity needed to produce the emission line luminosity must be larger than $L_{\rm x} \gtrsim 5 \times 10^{39}\,{\rm erg\,s^{-1}}$. This effectively rules out strong beaming because the observed X-ray luminosity is comparable to the one needed to produce the line emission (see e.g. Paper III). Another excellent example is NGC 5408 X-1 for which the same argument can be used to exclude strong beaming (Kaaret & Corbel, 2009). Also, similar conclusions have been reached using infra-red emission line diagnostics (Berghea et al., 2010) for Holmberg II X-1 and also for the ULX NGC 6946 X-1 (Berghea & Dudik, 2012).

Therefore, the ULX nebulae observations show that the X-ray emission from ULXs is truly ultra-luminous and that most their properties are better explained in the context of strong outflows from super-Eddington StMBHs rather than sub-Eddington IMBHs. However, it must be realised that these results are mere suggestions and that they are by themselves highly inconclusive. The BH masses powering ULX must clearly be inferred in some other way.

4.2.3 Population studies link ULXs to star formation

Further clues to the masses of BHs powering ULXs can be inferred from population studies (see Fabbiano 2006, for review). The main result from these studies has been that ULXs are connected to star formation within the galaxies and, more specifically, ULXs are linked to high mass X-ray binaries (HMXB).

By comparing the Galactic LMXB and HMXB populations (Grimm et al., 2002) to the extragalactic populations, Grimm et al. (2003) showed that a "universal" X-ray luminosity function (XLF) exists for HMXBs (XLF is the luminosity distribution of X-ray sources within the galaxy). They found that the XLFs of

HMXBs in all galaxies have the same slope and normalization if they are scaled with the galaxy's star formation rate (SFR, $[\mathrm{M}_\odot\,\mathrm{yr}^{-1}]$). This finding is not a surprising one, as the high mass companions in HMXBs are young, short-lived, stars. Therefore, a correlation between formation of HMXBs and the SFR of the host galaxy is a natural one and this finding allows to use the integrated X-ray luminosity of HMXBs to be used as a SFR proxy (Grimm et al., 2003; Gilfanov et al., 2004; Swartz et al., 2004; Mineo et al., 2012).

The connection of the universal XLF of HMXBs to the ULX population is very interesting. What the aforementioned authors found was that the same universal XLF of HMXBs extends from $L_\mathrm{x} \sim 10^{36}\,\mathrm{erg\,s^{-1}}$ to the ULX regime with no difference in the slope and normalization up to luminosities of about $L_\mathrm{x} \sim 10^{40}\,\mathrm{erg\,s^{-1}}$, where a cut-off in the slope was recently detected (Swartz et al., 2011; Mineo et al., 2012). This connection clearly tells us that most ULXs having luminosities between $L_\mathrm{x} \sim 10^{39}\,\mathrm{erg\,s^{-1}}$ and $L_\mathrm{x} \sim 10^{40}\,\mathrm{erg\,s^{-1}}$, are in fact part of the same HMXBs population (Grimm et al., 2003; Gilfanov et al., 2004; Swartz et al., 2004; Mineo et al., 2012).

However, the cut-off in the XLF also suggests that ULX above $L_\mathrm{x} \gtrsim 10^{41}\,\mathrm{erg\,s^{-1}}$ are not part of the HMXB population (Swartz et al., 2011) and, therefore, the most luminous ULXs, like M82 X-1 (also known as M82 X41.4+60; $L_\mathrm{x} \sim 10^{41}\,\mathrm{erg\,s^{-1}}$; Kaaret et al. 2001) and ESO 243–49 HLX-1 ($L_\mathrm{x} \sim 10^{42}\,\mathrm{erg\,s^{-1}}$, Farrell et al. 2009), are the best candidates to host IMBHs.[5] It is therefore not surprising that these two ULXs show similar spectral components and spectral states as Galactic StMBHs (Godet et al., 2009; Feng & Kaaret, 2010; Servillat et al., 2011), but with luminosities and spectral properties consistent with an IMBH (see Section 4.3).

Swartz et al. (2009) also found a correlation between star formation regions (HII regions and young star clusters) and locations of ULXs within the galaxies. However, many ULXs tend to be located near, but not within, the young clusters (see e.g. Portegies Zwart et al. 2004; Kaaret et al. 2004; Kong et al. 2007 and Poutanen et al., in preparation). Although these young clusters are ideal sites for formation of IMBHs and for the IMBH to capture a companion star from which to accrete (Portegies Zwart et al., 2004), simulations by Mapelli et al. (2011) indicate that the IMBHs should be bound to these clusters, whereas a large fraction of StMBHs should be ejected from them. Therefore, the ULXs that are located close to, but not within, these young clusters are most likely StMBHs and not IMBHs.

Although the results from population studies provide perhaps the strongest evidence that the majority of ULXs are in fact StMBHs in HMXBs (and not IMBHs), these results have one major drawback. We cannot use the results from

[5]Note that the super-Eddington StMBH model of Poutanen et al. (2007) does not predict apparent luminosities above $L_\mathrm{x} \gtrsim 10^{41}\,\mathrm{erg\,s^{-1}}$ either.

the population studies, if we observe one particular ULX and aim to estimate the BH mass powering it. The population studies do not offer a way to distinguish between the the various possibilities for a given ULX in the $L_{\rm x} \sim 10^{39}\,{\rm erg\,s^{-1}}$ to $L_{\rm x} \sim 10^{41}\,{\rm erg\,s^{-1}}$ range. Therefore, the BH mass scaling techniques utilizing X-ray timing- and spectral properties are currently the only viable techniques to infer the nature of ULXs.

4.3 X-ray mass scaling methods for ULXs

4.3.1 Mass scaling from ULX timing analysis

Detection and analysis of short term flux variations is a very good approach to probe the nature of ULXs. A very graphic example comes from the detection of X-ray dips from NGC 55 ULX (Stobbart et al., 2004). From light-crossing-time arguments, these 100–300 second time-scale flux variations support the compact nature of ULXs (i.e. emitting size must be less than 1 AU). Tight constraints for the size of the emission region came also with the discovery of milli-Hertz QPOs in ULXs (Strohmayer & Mushotzky, 2003).

Perhaps the most complete study of short term ULX variability study was performed by Heil et al. (2009). In addition to confirmation of the low frequency QPO detections in two ULXs (M82 X-1 and NGC 5408 X-1, see Strohmayer & Mushotzky 2003; Strohmayer et al. 2007; Dheeraj & Strohmayer 2012) and detection of ULXs with "break frequencies" in the power spectrum, they also found that some ULX – including Holmberg II X-1 – are "under-variable". The reason for this detected under-variability is not yet clear, but it suggests that the accretion flow in these ULX is somehow different from BHBs. Perhaps the lack of variability is a sign of a new accretion state in ULXs?

The most useful mass scaling method between BHBs and AGNs, the so called "variability plane" of compact objects, has been derived by McHardy et al. (2006) and Körding et al. (2007). This method utilises an empirical correlation between a BH mass, its bolometric luminosity and the break frequency. Alternatively, the break frequency can be associated with an observed QPO frequency and an analogous empirical correlation can be derived (Casella et al., 2008). The fact that QPOs have been now detected in AGNs as well (Gierliński et al., 2008), brings much hope in utilizing this method for ULXs. These techniques could be extremely powerful tools for rough ULX BH mass estimations, as luminosity and a QPO/break frequency (if present) are quantities that are easy to obtain from the X-ray data. Two ULXs were weighed using this method by Casella et al. (2008) and the results indicated that both of them (M82 X-1 and NGC 5408 X-1) were IMBHs. Similar constraints for NGC 5408 X-1 were also obtained by Soria et al. (2004), even before the aforementioned empirical cor-

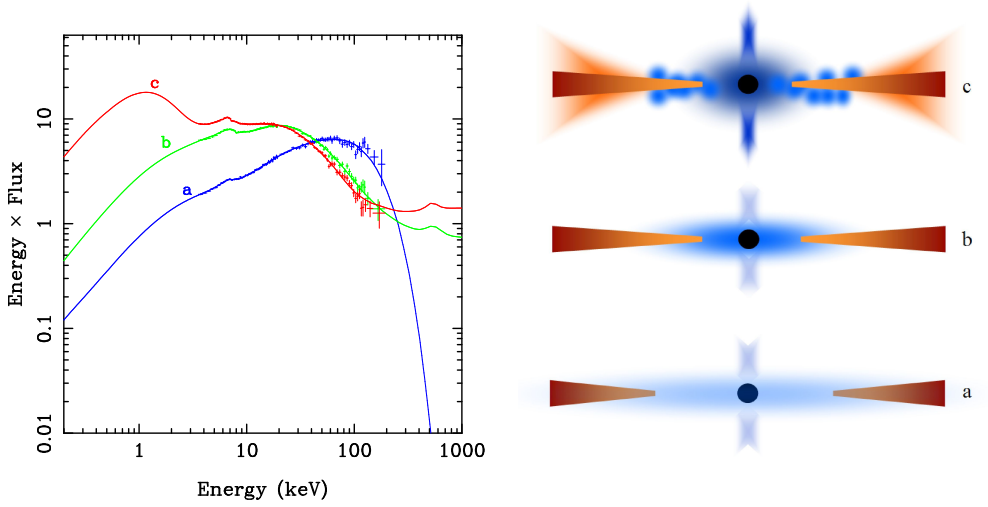

Figure 4.2. Left: hard-state spectrum (a) of the BHB XTE J1550–564 merging onto less Comptonized very high state spectrum (b) and then into an extreme very high-state spectrum (c). This spectral behaviour is seen in transient BHBs during the initial rise to X-ray outburst. Right: A range of possible accretion disc geometries which are thought to represent the hard-state and extreme very high-state. Figure from Done et al. (2007).

relation was found. However, it still remains to be shown whether the observed QPOs are analogous to the ones seen in BHBs (see e.g. Dheeraj & Strohmayer 2012). For example, the Galactic BHB Cygnus X-1 also shows low-frequency QPOs in its power spectrum (Vikhlinin et al., 1994), but we know for sure that this source is not an IMBH. Therefore if the QPOs seen in BHBs and ULXs are not analogous, then the scaling cannot be used and the IMBH evidence for these ULXs loses its strength. The analogy could be confirmed if a QPO in the ULX NGC 5408 X-1 were to be detected in the hard spectral state (Dheeraj & Strohmayer, 2012). However, this particular ULX has had a soft spectrum with $\Gamma \approx 2.5$ in all *XMM-Newton* observations (see Paper III; Dheeraj & Strohmayer 2012). A possible way forward would be to propose a joint *Swift/XMM-Newton* observing program, where *Swift*/XRT monitors the X-ray flux and spectral hardness and then if the NGC 5408 X-1 goes into a hard spectral state, *XMM-Newton* triggers and hopefully detects the QPO.

4.3.2 Mass scaling from spectral properties

In the absence of other viable alternatives, the BH mass scaling techniques using spectral properties have become the most promising approach. The spec-

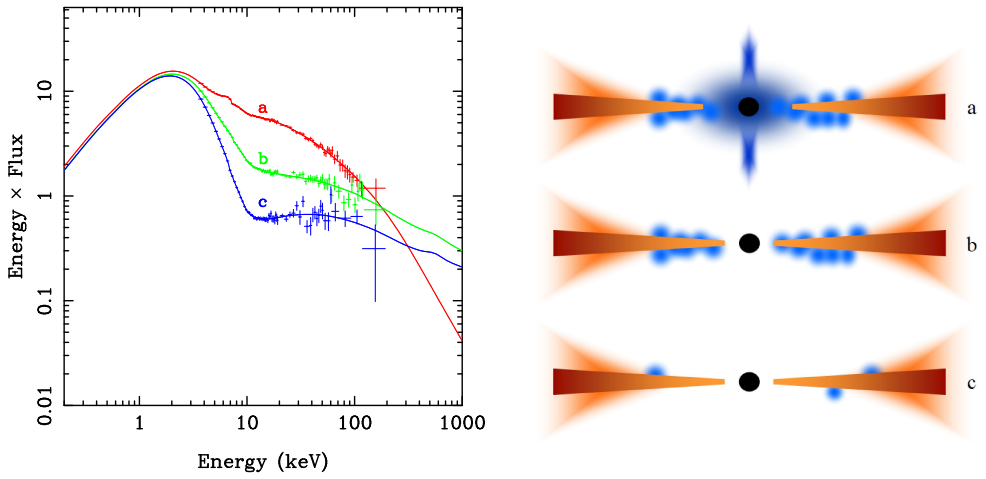

Figure 4.3. Left: Extreme very high-state spectrum (a) of the BHB XTE J1550–564 merging onto less Comptonized very high state spectrum (b) and then into a soft-state spectrum (c). Right: A range of possible accretion disc geometries which are thought to represent the very high states and soft states. Note how the edge of the geometrically thin disc is thought to reach ISCO only in soft spectral states. Figure from Done et al. (2007).

tral BH mass estimation techniques aim to find similarities in the observed spectral states in BHB and ULX (and to an extent, AGNs) and then use those continuum spectral components that scale with the BH mass to infer the nature of ULXs. In Paper III, Paper IV and Paper V, we have solely concentrated on these techniques.

The standard accretion disc model developed by Shakura & Sunyaev (1973) predicts that – for luminosities below the Eddington limit – the disc around a BH is geometrically thin but optically thick all the way down to the innermost stable circular orbit (ISCO). As briefly mentioned in the introduction, the ISCO is determined by the BH mass and its spin, such that for non-spinning BH it is located at $R_{\rm isco} = 3R_{\rm s}$, whereas for the most extreme BH spins $R_{\rm isco} = R_{\rm s}/2$ (Frank et al., 2002). Therefore, if the geometrically thin, optically thick disc extends all the way down to the ISCO and it emits black body radiation at each radius, we would expect that the emitted luminosity should scale as $L_{\rm disc} \propto T_{\rm disc}^4$ (simply because of the Stefan-Boltzmann law, see Section 1.3), where $T_{\rm disc}$ is the disc temperature at (or close) to the ISCO. The $L_{\rm disc} \propto T_{\rm disc}^4$ relation can be written in a slightly more meaningful way (Gierliński et al., 1999)

$$L_{\rm disc} = C M_{\rm bh}^2 T_{\rm c,max}^4, \tag{4.3}$$

where $T_{\rm c,max}$ is the maximum observed colour temperature, C =

$(\pi\sigma_{\rm sb}G^2)/(6c_0^4 f_{\rm col}^4 c^4)$ is a proportionality constant, $f_{\rm col}$ is the colour correction factor (describing the difference between the observed colour temperature and the effective temperature, i.e. $T_{\rm c,max} = f_{\rm col}T_{\rm eff}$) and $c_0 \approx 0.1067$. Using Equation (4.3), we can estimate the BH mass because both $L_{\rm disc}$ and $T_{\rm c,max}$ can be obtained by modelling the observed X-ray spectra.

The method is not without its caveats though, because of the assumptions that go into the scaling law in Equation (4.3). For BH accretion discs the colour correction factor $f_{\rm col} \sim 1.7 - 1.8$ has been computed by Shimura & Takahara (1995), but the exact value is not certain (Merloni et al., 2000; Davis et al., 2005). Because of the strong $f_{\rm col}^4$ dependence in Equation (4.3), not knowing this parameter accurately can cause large errors in the BH mass estimates. Furthermore, the scaling computed by Gierliński et al. (1999) uses the so called Pseudo-Newtonian potential approximation (Paczyński & Wiita, 1980) and it assumes that the inner disc is at $R_{\rm isco} = 3\,R_{\rm s}$, i.e. that the BH is non-rotating. The scaling also assumes that the maximum dissipation (per unit area) in the accretion disc does not coincide with the inner disc edge (because of an assumed zero-stress inner disc boundary condition), but instead at slightly larger radius. However, simulations by Krolik et al. (2005) seem to indicate that this boundary condition might be incorrect, which casts doubt on the exact dissipation profile at the very vicinity of ISCO where most of the X-ray radiation is released (see also Abramowicz et al. 2010, for discussion). If the zero-stress boundary condition is not taken into account – as in the simple spectral model DISKBB (Mitsuda et al., 1984) that is commonly used to obtain the colour temperature – the error should approximately 4 per cent (Gierliński et al., 1999; Gierliński & Done, 2004). However, despite all these uncertainties, in no way are they large enough to prevent us from applying the BH mass scaling in Equation (4.3) to differentiate between a $10\,{\rm M}_\odot$ StMBH and a $1000\,{\rm M}_\odot$ IMBH. But before we apply the scaling to ULXs, we must make sure that we are not comparing apples with oranges. Much like with the BH mass scaling from timing properties, we must make sure that spectral states are similar in BHBs and ULXs before we use the scaling.

The Galactic BHBs show two main spectral states – the soft state and the hard state – and these two states can be further divided into several sub-states (see Figure 4.2, Figure 4.3 and Done et al. 2007, for review). As similar spectral states are also found in AGNs which host up to $10^{10}\,{\rm M}_\odot$ SMBHs (see Zdziarski et al. 1999; Veledina et al. 2011), then if ULXs really are powered by sub-Eddington accretion onto IMBHs, there would be no reason to expect that the spectral states were substantially different in ULXs. It is generally believed that in the soft state – which is characterized by an energetically dominant disc (emitting ~ 1 keV black body spectrum) plus a weaker non-thermal spectral tail up to hundreds of keV – the geometrically thin (and optically thick) disc extends down to the ISCO. On the contrary, in the hard state, the the geometri-

cally thin disc is most likely truncated at some larger radius and the inner-most regions of the disc are thought to be replaced by a hotter, quasi-spherical flow (Done et al., 2007). In the hard state, the observed emission is produced in the hot flow by Comptonization from ~ 100 keV electrons: the seed photons for Comptonization come either from the disc photons or alternatively from synchrotron emission from the hot flow itself (Poutanen & Vurm, 2009; Malzac & Belmont, 2009). There are some signs of non-thermal electrons in the hard state, whereas in the soft state the entire hard X-ray tail is believed to be produced by non-thermal electrons in some active regions above the accretion disc (Haardt et al., 1994; Poutanen & Svensson, 1996; Poutanen & Vurm, 2009). Although there are many observational pieces of evidence that support the aforementioned picture, there are still claims that the optically thick disc extends to the ISCO in the hard state as well (see e.g. Reis et al. 2011 and references therein).

At the time we started to work on Paper III (at the beginning of 2008), it was not clear if the spectral states in ULXs were similar to those in BHBs. Although ULX spectra were known to have similar components as BHB spectra (see Figure 4.4), it was not clear if these components (and the spectra overall) varied anything like BHBs, simply due to lack of repeated observations of one particular ULX. The observations typically involved only 2 observations (Kubota et al., 2001) or very few ULXs (Feng & Kaaret, 2006, 2007). If ULXs hosted IMBHs, then the only difference between StMBHs would be that the inner disc temperatures had to be almost 10 times cooler than in the ~ 1 keV discs around StMBHs (Gierliński & Done, 2004), as can been seen from Equation (4.3). Therefore, the discovery of "soft excesses" in several ULX spectra – which could be modelled as a 0.1–0.4 keV thermal disc emission – seemed to suggest that ULXs really were IMBHs (e.g. Miller et al. 2003; Zampieri et al. 2004; Miller et al. 2004). However, spectral variability studies of ULXs were desperately needed, because we knew from experience that even though the scaling technique works extremely well for BHBs (Gierliński & Done, 2004), there are clear deviations from the $L_{\rm disc} \propto T_{\rm disc}^4$ relation especially at higher luminosities (Gierliński & Done, 2004; Done & Kubota, 2006). A good example is XTE J1550-564 (Done & Kubota, 2006), which shows clear deviations from the $L_{\rm disc} \propto T_{\rm disc}^4$ relation at the so called very high state (see Figure 4.3): the disc even seemed to become cooler at higher luminosities. Very interestingly, two ULXs in the NGC 1313 galaxy, showed very similar behaviour as XTE J1550-564 (see Feng & Kaaret 2006, 2007 and Soria 2007). This suggested that the cool ~ 0.2 keV accretion disc emission reported for ULXs does not originate from the disc and therefore cannot be used as a signature of an IMBH as had been proposed by several authors (e.g. Miller et al. 2003; Zampieri et al. 2004; Miller et al. 2004). An alternative hypothesis, that the cool ~ 0.2 keV thermal emission originates from a disc outflow (Poutanen et al., 2007) started to look more and

more probable, because the model predicts cooler thermal components with increasing luminosity. At the time we started working on Paper III, this was the state of art.

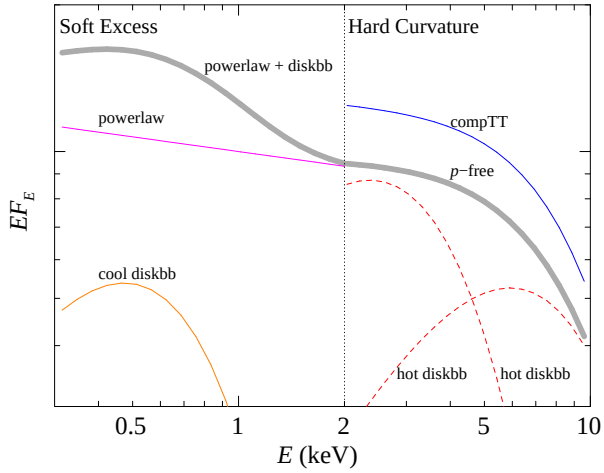

Figure 4.4. A schematic view of ULX spectral shapes and components in the 0.3–10 keV spectral band as proposed by Feng & Soria (2011). The main spectral features seen (with respect to simple power-law emission) are the soft excesses below 2 keV and spectral curvature above 2 keV. The soft excess can be modelled by a cool thermal component, which could rise from the inner disc around IMBHs, or alternatively from a disc outflow around a StMBH (Poutanen et al., 2007). The spectral curvature above 2 keV can be fitted with advective disc models, like the p-free model DISKPBB of Mineshige et al. (1994) where the radial temperature follows $T(r) \propto r^{-p}$, having $p \approx 0.5$ or with 2–3 keV temperature, optically thick Comptonization models. For comparison, Feng & Soria (2011) plotted two standard disc models that follow the $T(r) \propto r^{-3/4}$ temperature dependence, with inner disc temperatures $T_{\rm disc} = 1.0$ keV and 2.5 keV, respectively. They are typically more strongly curved than the data and cannot fit the energy spectrum over the 0.3–10 keV band. Figure from Feng & Soria (2011).

4.4 Results

4.4.1 Spectral variability of ULXs

As the name of Paper III suggested, our first goal was to understand the "spectral variability of ULXs". Up to the publication this paper no one had look for the existence of spectral variations in a large sample of ULXs that had been observed repeatedly over the ~ 8 year period that both *XMM-Newton* and

Chandra had been observing ULXs.[6] We therefore used a sample of 11 ULXs to study their spectral properties in order to investigate if the ULX spectral states were similar to BHBs. Furthermore, we were also interested to see if these ULXs had these putative cool ~ 0.1 keV thermal components and we wanted to investigate if they really followed the $L \propto T^4$ relation, expected if the emission came from the ISCO of an IMBH accretion disc.

In order to study the spectral states, our initial modelling was performed using simple absorbed POWERLAW spectral fits. In some cases, the observational data quality (and in some cases the lack of any spectral features) meant that this simple model was already statistically acceptable (Paper III), thus excluding the need to consider more complex models. In the majority of cases, however, this model was not statistically acceptable and the fits were improved by adding cool thermal components that had been already reported for some of the ULXs in the sample (see Miller et al. 2003; Zampieri et al. 2004; Miller et al. 2004 and especially the studies of Feng & Kaaret 2006, 2007). The model residuals of high signal-to-noise ratio observations also indicated that spectral curvature was present above ~ 5 keV in some sources (e.g. Holmberg II X-1), or that other subtle features around ~ 1 keV led to poor fit statistics (e.g. NGC 5408 X-1), but we chose to ignore those features as they could only been seen in a very few observations.

From these absorbed POWERLAW model spectral fits we discovered a new spectral variability pattern in ULXs (see Figure 4.5). Several ULX showed spectral pivoting in the observed band, meaning that the spectral flux was constant at a particular pivoting energy and the spectra then softened (Γ increased) with increasing luminosity. This behaviour led to the observed $L_{\rm x}$–Γ correlation for these sources, although the results are affected somewhat if additional spectral components were added to the model (Feng & Kaaret 2006; Paper III; Feng & Kaaret 2009). Three of the four ULXs – Holmberg II X-1, NGC 1313 X-1 and NGC 5204 X-1 – that showed spectral pivoting also had one occasion each, where clear deviations from these patterns occurred: the luminosity dropped and the spectra softened substantially from the pivoting trends, transitioning the ULXs into anomalous "low/soft state", which is never seen in BHBs (see Dewangan et al. 2004 and also Feng & Kaaret 2006; Roberts et al. 2006). Another feature was that some ULXs showed $L_{\rm x}$–Γ anti-correlation (see Figure 4.5). For these ULXs, the spectra were better fitted with a simple absorbed accretion disc model (DISKBB in XSPEC) than the absorbed POWERLAW model. Thus, the observed $L_{\rm x} - \Gamma$ anti-correlation was most likely spurious for these ULXs. By plotting the disc luminosities and inner disc temperatures in the same diagram as the Galactic BHBs from Gierliński & Done (2004), we

[6] It must be noted that at the same time we published Paper III, very similar results were published by Feng & Kaaret (2009) using almost the same ULXs as we did.

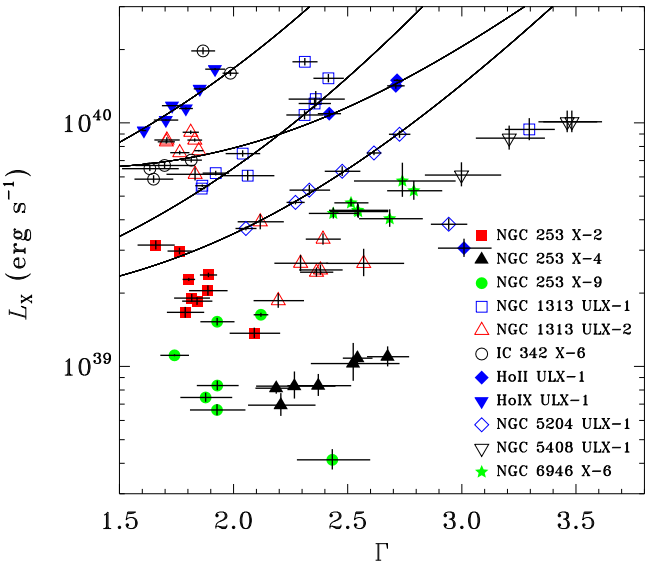

Figure 4.5. The intrinsic 0.4–10 keV band luminosity versus the photon index Γ from the POWERLAW model fits for the ULX sample of Paper III. ULX showing spectral pivoting in the observed band are connected by a theoretical curve for pivoting (Zdziarski et al. 2003; Paper III). Some ULX have the $L_{\rm x}$–Γ correlation, but no spectral pivoting and some others even show anti-correlation. The ULX with $L_{\rm x}$–Γ anti-correlation are better fitted with alternative spectral models (see Paper III). Figure from Paper III.

detected a striking similarity between these ULXs and BHBs (see Figure 4.6). Especially all the NGC 253 ULXs – having luminosities at the edge of ULX definition $L_{\rm x} \sim 10^{39}\,{\rm erg\,s^{-1}}$ – followed similar tracks in the $L_{\rm disc}$–$T_{\rm disc}$ diagram. NGC 253 X-2 follows the $L_{\rm disc} \propto T_{\rm disc}^4$ track and seems to be like a high luminosity extension to the behaviour seen in XTE J1550–564 and LMC X-3. NGC 253 X-4 clearly does not follow the $L_{\rm disc} \propto T_{\rm disc}^4$ track, but instead follows exactly the same pattern as LMC X-1 with cooler thermal component with increasing luminosity, which might be a sign of an outflow in these systems. NGC 253 X-9 is clearly a hybrid of these two aforementioned ULXs, as at lower luminosities this ULX seems to follow the $L_{\rm disc} \propto T_{\rm disc}^4$ track like NGC 253 X-2, but then at higher luminosities the trend seems to reverse like in NGC 253 X-4. However, strong conclusions and interpretations are not possible to be made, because of the limited amount of data available (6 observations).

The ULXs that could not be fitted with any purely thermal model, nor with simple absorbed POWERLAW model, were fitted with a POWERLAW+DISKBB model, that had been commonly used for ULXs and also for BHBs. These fits gave the most interesting result we obtained with respect to the nature of the soft excess, that had been taken as evidence of IMBH accretion discs by many authors (e.g. Miller et al. 2003; Zampieri et al. 2004; Miller et al. 2004. Our

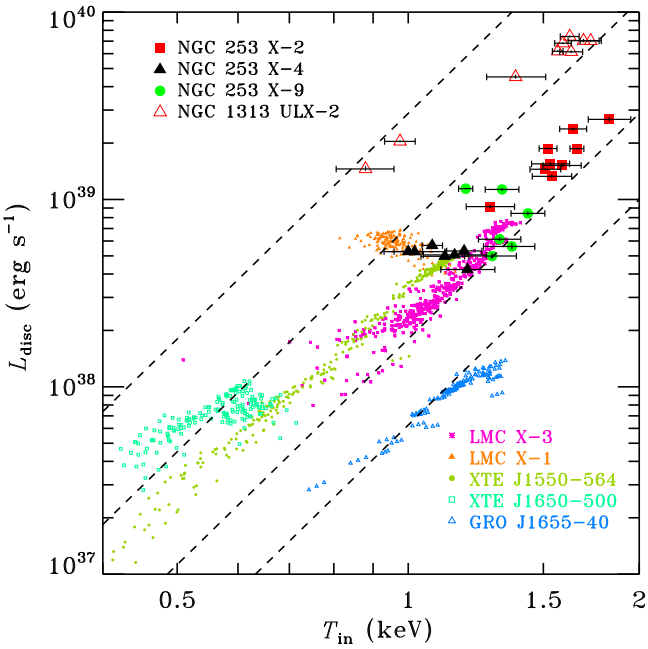

Figure 4.6. The luminosity-temperature diagram for ULXs that could be fitted with the DISKBB model. These ULXs follow the tracks of known BHBs shown by small symbols (BHB data adapted from Gierliński & Done 2004). Figure from Paper III.

spectral analysis did not support the conclusions of these earlier studies. We found that instead of following the $L_{\rm disc} \propto T_{\rm disc}^4$ track as the low-luminosity ULXs in the sample, these ULXs had roughly a $L_{\rm disc} \propto T_{\rm disc}^{-3.5\pm0.2}$ scaling. This is totally inconsistent with the earlier assumption that these systems follow $L_{\rm disc} \propto T_{\rm disc}^4$ track and thus the BH mass scaling cannot be used at all for these ULXs. We proposed that the thermal emission comes from the outflow and thus these ULXs might be super-Eddington StMBHs instead of sub-Eddington IMBHs.

The preliminary results of Paper III were already published in a conference proceeding (Kajava & Poutanen, 2008) and King (2009) used the result to obtain a rough scaling between the beaming factor and the mass accretion rate $b \propto \dot{m}^{-2}$. However, this scaling must be taken with extreme caution, because of the inherent problems in the determination of the *intrinsic* luminosity and the temperature of the cool thermal component. The problem arises because the observed temperatures are so cool that we only see the exponentially cut-off tail of the black body emission at the lowest energy instrument channels, which are always the least well calibrated. Furthermore, the cool thermal emission comes in the spectral region where the (unknown) interstellar absorption is the strongest and, therefore, the results depend on the way the absorption

is taken into account. Even more alarmingly, in some cases the results depend slightly on the (somewhat arbitrary) selection of the low-energy fitting boundary (which explains the small differences in our results to those published by Feng & Kaaret 2009). Although the King (2009) scaling is tempting – as it could be potentially helpful to make mass accretion rate estimates in ULXs (assuming they truly are StMBHs) – one must keep in mind that the spectral modelling related uncertainties give large systematic errors.

In any case, our results are not in favour of the IMBH interpretation at least for the ULXs that were in our sample. However, given the large uncertainties in the discovered $L_{\rm disc} \propto T_{\rm disc}^{-3.5\pm0.2}$ scaling, the results do not entirely follow the predictions of the Poutanen et al. (2007) model, unless the beaming factor is as extreme as King (2009) proposed. Now, in terms of using the ULXs to find the few IMBHs in the haystack filled with StMBHs, these results can provide very interesting constraints. Namely, if the ULXs in our sample were all StMBHs, then perhaps they all share some similar spectral property that sets them apart from the IMBH candidates. A potential discriminator between these two alternatives could be the discovery of spectral curvature (or "spectral breaks") in most of these ULXs (Stobbart et al., 2006) that might be a sign of a new "ultra-luminous state" (Gladstone et al., 2009).

4.4.2 Spectral variability in the ULX Holmberg II X-1

One of the best sources to study spectral variations are the closest, luminous ULXs, because for them we can detect the biggest number of photons in the shortest amount of observing time. If we want to look for weak spectral components (such as the soft excesses at around ~ 1 keV) or spectral shapes at energies above ~ 5 keV, we need to observe bright ULXs such as Holmberg II X-1 ($D = 3.4$ Mpc, Karachentsev et al. 2002), which are known to be intrinsically variable (Dewangan et al. 2004; Paper III).

As mentioned earlier, *Swift* observers do not have a proprietary period for their data. In spring 2010 (while making preparatory work for Paper I), I happened to stumble on the *Swift* observing schedule and found that a monitoring program of Holmberg II X-1 was ongoing and out of curiosity I had a closer look. I immediately saw that this ULX was at a historically low luminosity level (see Figure 4.8) and we therefore started a collaboration and triggered an *XMM-Newton* target-of-opportunity observation to obtain a more detailed spectrum and time-series than was possible to get from the *Swift*/XRT data. We wanted to trigger the *XMM-Newton* observation of this ULX when it was below $L_{\rm x} \sim 10^{39}\,{\rm erg\,s^{-1}}$, because at these low luminosities we could have directly compared the source to Galactic systems such as GRS 1915+105 that reach these luminosity levels (Done et al., 2004). However, the initial goal of our observation was not reached because the ULX underwent a minor flare just

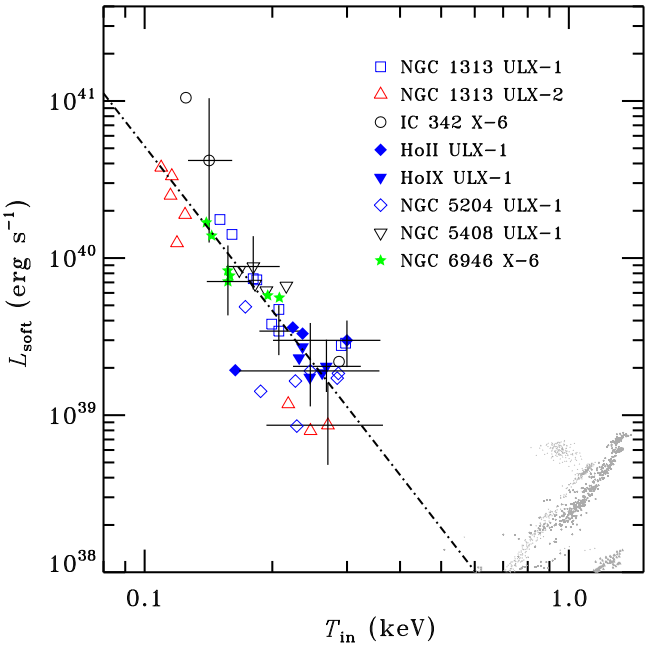

Figure 4.7. The luminosity-temperature diagram of the soft excess from the POWERLAW+DISKBB model fits. All the ULX follow roughly a $L_{\rm disc} \propto T_{\rm disc}^{-3.5}$ scaling. Note however that this scaling is subject to some modelling uncertainties (see text and Paper III). This result contradicts previous claims of IMBHs in these ULXs, because these earlier estimations relied on the assumption that the $L_{\rm disc} \propto T_{\rm disc}^{4}$ scaling applies. Figure from Paper III (BHB data adapted from Gierliński & Done 2004).

prior to the *XMM-Newton* observation. Although we were slightly unfortunate, the *XMM-Newton* spectrum we obtained was still the highest quality ever taken from this source in such a low luminosity state. The *Swift*/XRT monitoring and *XMM-Newton* target-of-opportunity observation led to two publications, Paper IV and Paper V, respectively.

Holmberg II X-1 showed very strong flaring during the 2009/2010 *Swift*/XRT monitoring. The luminosity was seen to fluctuate from less than the ULX definition limit of $L_{\rm x} \lesssim 10^{39}\,{\rm erg\,s^{-1}}$, up to $L_{\rm x} \sim 2\times10^{40}\,{\rm erg\,s^{-1}}$ (Paper IV). The flaring itself was not periodic. It was very interesting to note that the spectrum was very soft throughout the monitoring with $\Gamma \sim 3$. The luminosity went up and down by an order of magnitude without major changes in spectral hardness (see Figure 4.8. left panel). This variability pattern is not common in BHBs in their soft spectral states. Instead, this type of behaviour is only seen while BHBs are in hard spectral states with $\Gamma \approx 1.6$–1.8 (e.g. Done et al. 2007). Furthermore, in 2006 – when this ULX was in a hard spectral state with $\Gamma \approx 1.8$ – the luminosity was similar to that during the 2009/2010 soft state

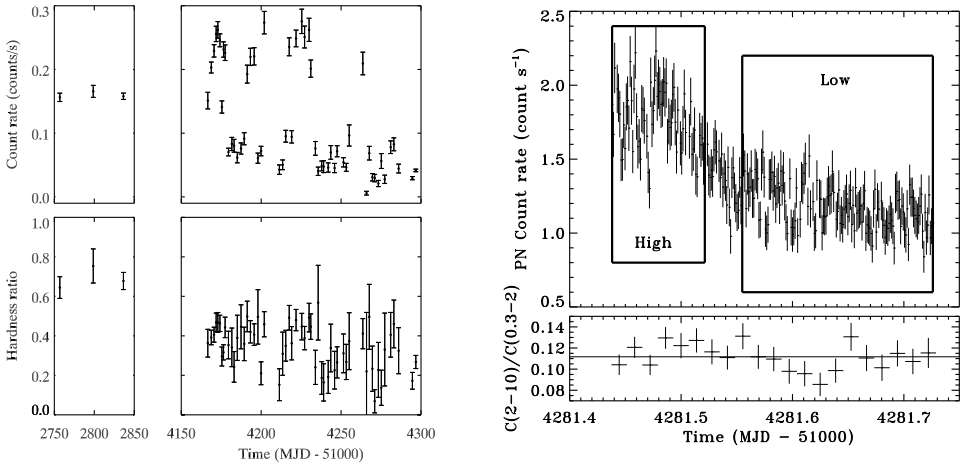

Figure 4.8. Left: X-ray light curve from *Swift* monitoring of Holmberg II X-1 in the 0.3–10 keV band (top panels) and corresponding spectral hardness ratio (1.5–10 keV band count rate divided by 0.3–1.5 keV count rate, bottom panels). Figure from Paper IV. Right: *XMM-Newton*/EPIC-pn light curve in the 0.3–10 keV band and the spectral hardness ratio (2–10 keV band count rate divided by 0.3–2 keV count rate), which does not vary as the flux decays by ~ 50 per cent. Figure from Paper V.

monitoring. This behaviour is not typical in Galactic BHBs either (Dunn et al., 2010). In BHBs, the hard states are usually seen at lower luminosities than the soft states, which is also the reason these states are sometimes called low/hard and high/soft states (Done et al., 2007). Thus both the constant $\Gamma \sim 3$ during the soft state – and the fact that the spectral state does not depend on emitted luminosity – makes the variability patterns of this particular ULX considerably different compared to BHBs. Therefore, these differences make it unlikely that this ULX is powered by accretion onto an IMBH.

Further differences with this ULX and the BHBs can be seen also in the *XMM-Newton* observation we triggered (see Paper V). We saw a ~ 50 per cent decay in the flux from the beginning of the observation to the end and (like the *Swift*/XRT monitoring) the spectral hardness remained constant (see Figure 4.8, right panel). The spectrum showed both spectral components that are seen in high quality ULX spectral data. After fitting the data with a simple absorbed POWERLAW model (see Figure 4.9a), both the soft excess below 2 keV and the spectral curvature above 2 keV were needed to fit the data. By comparing our low-luminosity state *XMM-Newton* spectra of Holmberg II X-1 to the one taken at a high luminosity state in 2004, we found an interesting difference. We found that the spectral break energy $E_{\rm br}$ (in keV) – or alternatively the gas temperature – increased from 4 keV to 5.4 keV with increasing observed

luminosity between these two data sets. This behaviour is completely opposite to what had been previously seen for two other ULXs – Holmberg IX X-1 (Vierdayanti et al., 2010) and M33 X-8 (Middleton et al., 2011) – where $E_{\rm br}$ (or alternatively the temperature) was anti-correlated with luminosity. These authors suggested that the $E_{\rm br}$–$L_{\rm x}$ anti-correlation arises from the properties of the low-temperature corona that is thought to be located above the central parts of the accretion disc, much like in the very high states of BHBs (see Figure 4.3). The idea is that when the luminosity increases (due to increase in the mass accretion rate), the central parts of the accretion disc would launch an outflow, which increases the density in the corona. The increasing mass density causes the coronal energy to be shared with an increasing number of particles, thus leading to a lower equilibrium temperature of the emitting gas (Vierdayanti et al., 2010). This argument cannot explain the observed $E_{\rm br}$–$L_{\rm x}$ trend seen in Holmberg II X-1. What is instead more plausible is that the hot gas we are seeing in our spectral fits is in fact the accretion disc. The order of magnitude estimate for the inner disc radius we obtained by modelling the data with a simple phenomenological disc advection/outflow spectral model (see Figure 4.9) was roughly $R_{\rm disc} \sim 20$ km, which is in good agreement for an ISCO of a StMBH. What is possible is that the low-temperature corona is not always present in ULXs – much like the corona is not always present in BHBs – but it is still too early to make strong conclusions based on just a few observations. In order to see any underlying trends, we need frequent monitoring programs of a few, bright ULXs like Holmberg II X-1 or Holmberg IX X-1. Alternatively, we should analyse the spectra of all ~ 500 ULX candidates and to search if there are any trends with luminosities and spectral breaks in the whole ULX population.

4.5 Discussion

The results we have obtained all argue against the idea that the majority of ULXs are powered by accretion onto IMBHs. The ULXs we have studied all show large discrepancies between the spectral states and variability patterns as compared to BHBs, for which we know for sure that they host $\sim 10\,{\rm M}_{\odot}$ StMBHs. If ULXs were truly powered by sub-Eddington accretion onto IMBHs, there would be no reason to believe that the spectral states and variability patterns should be any different, given that the more massive SMBHs at the centres of galaxies share common properties with BHBs. Therefore, the differences between ULXs and BHBs clearly indicate that the accretion flows between these sources are different and a natural explanation of these differences is that the ULX are powered by super-Eddington accretion onto StMBHs. In these cases, the accretion flows are affected by advection and outflows, which together can

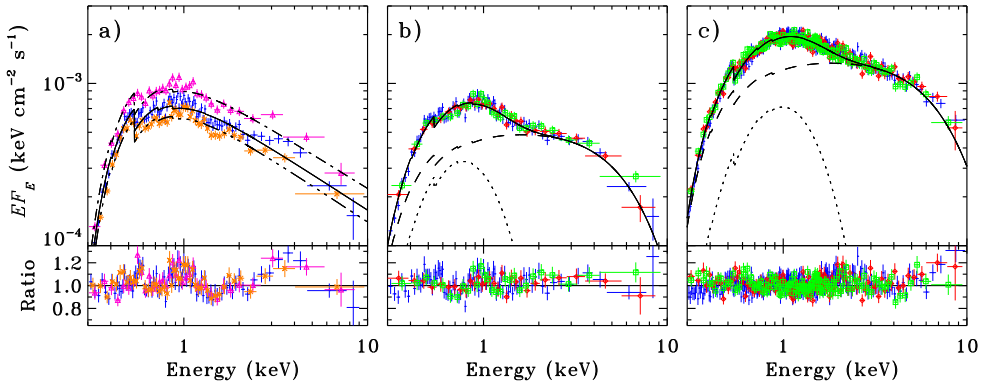

Figure 4.9. a) The high state (pink triangles), time-averaged (blue crosses) and low state (brown diagonal crosses) EPIC-pn EF_E spectra for the 2010 *XMM-Newton* observation of Holmberg II X-1, modelled with an absorbed POWERLAW (see also Figure 4.8). The dot-dashed, solid and three-dot-dashed lines show the model spectrum for high, time-averaged and low flux states, respectively. The spectral residuals are very similar to the *Swift*/XRT low flux spectra (Grisé et al., 2010) and the shape of the residuals indicate that the chosen continuum is incorrect. It is also visibly by eye that there is a clear spectral curvature break at approximately 3–4 keV. b) The time averaged EF_E spectra of the 2010 *XMM-Newton* observation, modelled with BLACKBODY+DISKPBB (DISKPBB is the p-free model of Mineshige et al. (1994) that is appropriate for discs with advection or outflows, see Paper V); red diamonds and green squares denote EPIC-mos1 and mos2 spectra, respectively. The dotted and dashed lines show the BLACKBODY and DISKPBB model components, respectively. The spectral curvature/break can be described with this model. c) The time averaged EF_E spectra of the 2004 *XMM-Newton* observation of Holmberg II X-1. Figures from Paper V.

produce variability patterns that differ from the BHBs (Poutanen et al., 2007). However, although we obtained strong evidence that IMBHs do not fit with the observed data to these particular 11 ULXs we have studied, by no means can we generalise our results to the entire ULX population. In fact, very recently a few ULXs have been shown to behave as if they were IMBHs. For example, ESO 243-49 HLX-1 (Farrell et al., 2009; Davis et al., 2011), M82 X41.4+60 (Feng & Kaaret, 2010), M82 X37.8+54 (Jin et al., 2010) and the NGC 247 ULX (Jin et al., 2011) have all been detected in a soft state where the ~ 0.1 keV disc component contributes most of the flux below ~ 1 keV. Furthermore, two of these ULX – ESO 243-49 HLX-1 and M82 X41.4+60 – show similar spectral state transitions as in BHBs and the disc components follow the $L \propto T^4$ relation (see Godet et al. 2009; Servillat et al. 2011 and Feng & Kaaret 2010, respectively). Therefore, these ULXs are most likely IMBHs. It is perhaps no surprise to find the best evidence of ULXs from the most luminous ($L_{\rm x} \gtrsim 10^{41}\,{\rm erg\,s^{-1}}$) ULX, because the super-Eddington models do not predict such high luminosities

(Poutanen et al., 2007).

The spectral curvature in the 2–10 keV band in ULX spectra can perhaps be a feature that we can use to differentiate StMBHs and IMBH candidates. The spectral curvature is detected in most good quality observations of ULXs (Stobbart et al., 2006) and it might be a signature of a new "ultra-luminous state" (Gladstone et al., 2009). If it really turns out to be so, a simple spectral fit in the *XMM-Newton* band could be potentially used to separate StMBHs and IMBH candidates from each other. Further studies using larger samples of ULXs are required to investigate this possibility. Such a finding would provide a very powerful diagnostic tool, as only one X-ray observation would be needed to separate the super-Eddington StMBHs into their own group. This would be observationally much more efficient than using the ~ 0.2 keV soft excess variability analysis, as it now looks that both super-Eddington StMBHs and sub-Eddington can explain these spectral components, as thus we need multiple observations to look for the $L_{\rm disc}$–$T_{\rm disc}$ dependency to differentiate between the alternatives. But the jury is still out with respect to the nature of the spectral curvature. We simply do not have enough data to make definite conclusions. The results we published in Paper V show that the variability of spectral break energy as function of luminosity is different in Holmberg II X-1 as compared to other ULXs Holmberg IX X-1 (Vierdayanti et al., 2010) and M33 X-8 (Middleton et al., 2011). This raises questions about what causes the break and further observations are needed to understand these differences. We speculated that the spectral curvature is caused by thermal accretion disc emission from the regions close to the ISCO, instead of a low-temperature corona covering the central parts of the disc. The central parts of the super-Eddington accretion disc may very well be overheated (Beloborodov, 1998), which can cause large increases of colour temperature (i.e. large colour correction factors). Perhaps this is the reason for the very high inner disc temperatures found by Gladstone et al. (2009) using the advective p-free disc model (Mineshige et al., 1994): the colour correction factor might have been very high.

These differences can be studied with great detail now after the June 2012 launch of NASA's *NuSTAR* mission, which can observe ULXs in the 5–80 keV band. Perhaps the first *NuSTAR* ULX observations are already published by the time this thesis goes to print. The potential of this mission to determine the harder spectral components of ULXs is enormous. Already from the *XMM-Newton* schedule one can see that simultaneous *XMM-Newton* and *NuSTAR* observations of galaxies such as NGC 1313, IC 342, Holmberg IX, NGC 1365 and NGC 5204 are already planned (although the launch delay of *NuSTAR* might affect the scheduling). Together, these two satellites provide a broad 0.2–80 keV band, which will allow to study the spectral breaks/curvature in great detail. Perhaps, we will finally get definite answers to the nature of the hard spectral component. This will most likely motivate us to look for these spectral breaks in

archived *XMM-Newton* observations as well. It would be very interesting to see whether the ULXs that *XMM-Newton* seems to see in the new "ultra-luminous state" (Gladstone et al., 2009) will follow the same spectral behaviour now that we have a broader spectral band. I suspect that we will see surprises. For example, with *NuSTAR* we could investigate if the spectral pivoting in ULXs (which we discovered in three ULXs in Paper III) is similar to that in the Galactic BHB Cyg X-1, which shows similar pivoting closer to ~ 100 keV, where the spectral curvature/cutoff is associated with the ~ 100 keV thermal electrons in the corona (Zdziarski et al., 2002). Perhaps the pivoting seen in ULXs and the associated spectral curvature is also related to a corona, but in the case of ULXs the temperatures are more than 10 times lower. With *NuSTAR*, this type of investigation will become very easy to perform.

Chapter 5

Summary and future prospects

5.1 Summary and future prospects

In this thesis I have studied properties of two types of X-ray emitting binary star systems that host compact stars: Galactic AMPs, which are accreting NSs and extra-galactic ULXs, which are thought to be powered by accretion onto BHs. I have discussed how compact star masses and radii can be inferred using X-ray spectroscopic- and X-ray timing methods. The results presented in this thesis have brought new information about AMPs and ULXs, which helps us to determine these important stellar parameters in future studies.

I have demonstrated how NS masses and radii can be constrained by modelling the pulse profiles of AMPs. However, current constraints are not accurate enough because the pulse profiles are affected also by other unknown factors such as binary inclination, hotspot location and size on the NS surface and the emission pattern of radiation. Fortunately, the pulse profiles of AMPs are variable during X-ray outbursts and these variations cannot be attributed to changes in binary inclination, NS mass nor the NS radius. The understanding of the physical origins of pulse profile transitions in AMPs is the key to unlock the problem, because the correct NS mass and radius must fit all the pulse profiles. Therefore, the most important result discussed in this thesis was the discovery that pulse profile variability in the AMP SAX J1808.4–3658 can be caused by dynamic interaction between the NS magnetosphere and the accretion disc. We obtained observational evidence that the magnetic interaction region from the truncation radius $R_{\rm t}$ up to the magnetospheric radius $R_{\rm m}$ can be extensive and that $\dot{M}$-independent variations of $R_{\rm m}$ (i.e. sudden opening of field lines connecting the NS to the accretion disc) can channel the accretion flow onto different places on the NS surface, thus causing the pulse profiles to suddenly change. With this physical picture we could explain the simultaneous spectral- and timing transition seen during the 2008 outburst of SAX J1808.4–3658. The

same physical mechanism can also be responsible for the $\dot{M}$-independent X-ray timing noise in AMPs and it can also cause the accretion torques that the NS experiences during X-ray outbursts to be $\dot{M}$-independent. This discovery will therefore provide a solid ground for future investigations. Similar events are seen in the previous 2002 and 2005 outbursts, and also during the 2011 outburst of SAX J1808.4–3658. With the result obtained during this thesis work, we can now go back to re-analyse these data and use these similar events to confirm the result. Furthermore, we can make use of the developed physical picture and model all the pulse profile variations of SAX J1808.4–3658 simultaneously. By having 4 or 5 different "before/after-transition" pulse profile pairs, we can put stronger mass and radius constraints than was possible by using only the 2008 data. I am confident that the constraints will already become meaningfully tight, so that we can finally start to exclude some NS EOSs and thus, we can use AMPs to probe properties of ultra-dense matter in NS cores. By obtaining tighter constraints of NS masses and radii – as a "by-product" – we can infer the minimum masses of BHs.

The results presented in this thesis can also help to uncover the higher end of the stellar BH mass distribution that can be formed from stellar evolution. Although our results suggest that the majority of ULXs are not massive $\sim 1000\,\mathrm{M}_{\odot}$ IMBHs, but rather $\sim 10\,\mathrm{M}_{\odot}$ StMBHs accreting at super-Eddington rates, the results also suggest that there might be a way of separating the StMBH ULXs from IMBH candidates. We have observed that some ULXs have completely different variability patterns than those seen in Galactic BHBs. We have shown that the ~ 0.1 keV cool thermal components do not follow the $L_{\mathrm{disc}} \propto T_{\mathrm{disc}}^{4}$ relation, which had been a key assumption in arguments trying to invoke IMBHs with optically thick accretion discs extending down to the ISCO. As in the IMBH scenario one expects that spectral variability patterns should be similar to those in BHBs, these differences can be used to separate IMBH candidates from the super-Eddington StMBHs. In our investigations, we also focused on one bright ULX Holmberg II X-1. For this particular ULX, we have found that the long term variability patterns are also substantially different than what is observed for BHBs and we found evidence of a spectral component that is atypical in BHBs. Therefore, instead of discovering the most massive BHs, we might have found a way of separating the StMBH ULXs from IMBH ULXs. Perhaps all StMBH ULXs that have atypical variability patterns all possess spectral break/curvature, which is not seen in BHBs. Thus, this spectral component might be a signature of super-Eddington accretion flows (Poutanen et al., 2007; Gladstone et al., 2009) and it can therefore be used to separate IMBHs from StMBH ULXs. Now that the NASA's *NuStar*-mission is observing ULXs, together with *XMM-Newton* it will together provide a broad 0.2–80 keV spectral band, which will allow to study the spectral properties of ULXs much better in the future. We are at the brink of new discoveries.

Bibliography

Abolmasov P., 2011, New Astron., 16, 138
Abolmasov P., Fabrika S., Sholukhova O., Afanasiev V., 2007, Astrophys. Bull., 62, 36
Abramowicz M. A., Czerny B., Lasota J. P., Szuszkiewicz E., 1988, ApJ, 332, 646
Abramowicz M. A., Jaroszyński M., Kato S., Lasota J.-P., Różańska A., Sądowski A., 2010, A&A, 521, A15
Agapitou V., Papaloizou J. C. B., 2000, MNRAS, 317, 273
Alpar M. A., Cheng A. F., Ruderman M. A., Shaham J., 1982, Nature, 300, 728
Altamirano D., et al., 2011, ApJ, 727, L18
Aly J. J., Kuijpers J., 1990, A&A, 227, 473
Arnaud K. A., 1996, in G. H. Jacoby & J. Barnes eds., ASP Conf. Ser. 101, ADASS V, p. 17
Arnaud K., Smith R., Siemiginowska A., 2011, in Handbook of X-ray Astronomy, R. Ellis et al. eds., Cambridge Univ. Press, Cambridge
Baade W., Zwicky F., 1934, Proceedings of the National Academy of Science, 20, 259
Backer D. C., Kulkarni S. R., Heiles C., Davis M. M., Goss W. M., 1982, Nature, 300, 615
Balbus S. A., Hawley J. F., 1998, Rev. Mod. Phys., 70, 1
Barthelmy S. D., 2004, K. A. Flanagan & O. H. W. Siegmund eds., Proc. SPIE, 5165, p. 175
Belczynski K., Bulik T., Fryer C. L., Ruiter A., Valsecchi F., Vink J. S., Hurley J. R., 2010, ApJ, 714, 1217
Beloborodov A. M., 1998, MNRAS, 297, 739
Beloborodov A. M., 2002, ApJ, 566, L85
Berghea C. T., Dudik R. P., 2012, ApJ, 751, 104
Berghea C. T., Dudik R. P., Weaver K. A., Kallman T. R., 2010, ApJ, 708, 364
Blackburn J. K., 1995, in R. A. Shaw, H. E. Payne, & J. J. E. Hayes eds., ASP Conf. Ser. 77, ADASS IV, p. 367
Bradt H. V., Rothschild R. E., Swank J. H., 1993, A&AS, 97, 355
Burderi L., Di Salvo T., Menna M. T., Riggio A., Papitto A., 2006, ApJ, 653, L133
Burrows D. N., et al., 2005, Space Sci. Rev., 120, 165
Cackett E. M., Altamirano D., Patruno A., Miller J. M., Reynolds M., Linares M., Wijnands R., 2009, ApJ, 694, L21
Cadeau C., Leahy D. A., Morsink S. M., 2005, ApJ, 618, 451
Cadeau C., Morsink S. M., Leahy D., Campbell S. S., 2007, ApJ, 654, 458
Campana S., Stella L., Kennea J. A., 2008, ApJ, 684, L99
Casella P., Ponti G., Patruno A., Belloni T., Miniutti G., Zampieri L., 2008, MNRAS, 387,

1707
Chadwick J., 1932, Royal Society of London Proc. Ser. A, 136, 692
Chakrabarty D., Morgan E. H., 1998, Nature, 394, 346
Chandrasekhar S., 1931, MNRAS, 91, 456
Chandrasekhar S., 1935, MNRAS, 95, 207
Colbert E. J. M., Mushotzky R. F., 1999, ApJ, 519, 89
Comella J. M., Craft H. D., Lovelace R. V. E., Sutton J. M., 1969, Nature, 221, 453
Cseh D., Grisé F., Corbel S., Kaaret P., 2011, ApJ, 728, L5
Cseh D., et al., 2012, ApJ, 749, 17
Cui W., Morgan E. H., Titarchuk L. G., 1998, ApJ, 504, L27
Davis S. W., Blaes O. M., Hubeny I., Turner N. J., 2005, ApJ, 621, 372
Davis S. W., Narayan R., Zhu Y., Barret D., Farrell S. A., Godet O., Servillat M., Webb N. A., 2011, ApJ, 734, 111
Deloye C. J., Heinke C. O., Taam R. E., Jonker P. G., 2008, MNRAS, 391, 1619
Demorest P. B., Pennucci T., Ransom S. M., Roberts M. S. E., Hessels J. W. T., 2010, Nature, 467, 1081
den Herder J. W., et al., 2001, A&A, 365, L7
Dewangan G. C., Miyaji T., Griffiths R. E., Lehmann I., 2004, ApJ, 608, L57
Dheeraj P. R., Strohmayer T. E., 2012, ApJ, 753, 139
Di Matteo T., Springel V., Hernquist L., 2005, Nature, 433, 604
Done C., Kubota A., 2006, MNRAS, 371, 1216
Done C., Diaz Trigo M., 2010, MNRAS, 407, 2287
Done C., Wardziński G., Gierliński M., 2004, MNRAS, 349, 393
Done C., Gierliński M., Kubota A., 2007, A&A Rev., 15, 1
Dubner G. M., Holdaway M., Goss W. M., Mirabel I. F., 1998, AJ, 116, 1842
Dunn R. J. H., Fender R. P., Körding E. G., Belloni T., Cabanac C., 2010, MNRAS, 403, 61
Ebisuzaki T., et al., 2001, ApJ, 562, L19
Fabbiano G., 1989, ARA&A, 27, 87
Fabbiano G., 2006, ARA&A, 44, 323
Fabrika S., 2004, Astrophys. and Space Phys. Rev., 12, 1
Falanga M., et al., 2005, A&A, 444, 15
Farrell S. A., Webb N. A., Barret D., Godet O., Rodrigues J. M., 2009, Nature, 460, 73
Farrell S. A., et al., 2012, ApJ, 747, L13
Feng H., Kaaret P., 2006, ApJ, 650, L75
Feng H., Kaaret P., 2007, ApJ, 660, L113
Feng H., Kaaret P., 2009, ApJ, 696, 1712
Feng H., Kaaret P., 2010, ApJ, 712, L169
Feng H., Soria R., 2011, New Astron. Rev., 55, 166
Ferrarese L., Ford H., 2005, Space Sci. Rev., 116, 523
Ferrigno C., et al., 2011, A&A, 525, A48
Foster D. L., Charles P. A., Holley-Bockelmann K., 2010, ApJ, 725, 2480
Frank J., King A., Raine D. J., 2002, Accretion Power in Astrophysics: Third Edition, Cambridge Univ. Press, Cambridge
Fromang S., Stone J. M., 2009, A&A, 507, 19
Fruscione A., et al., 2006, in Silva D. R. & Doxsey R. E. eds., Proc. SPIE, 6270, p. 60
Gabriel C., et al., 2004, in F. Ochsenbein, M. G. Allen, & D. Egret eds., ASP Conf. Ser.

314, ADASS XIII, p. 759
Galloway D. K., Cumming A., 2006, ApJ, 652, 559
Garmire G. P., Bautz M. W., Ford P. G., Nousek J. A., Ricker Jr. G. R., 2003, in J. E. Truemper & H. D. Tananbaum eds., Proc. SPIE, 4851, p. 28
Gehrels N., et al., 2004, ApJ, 611, 1005
Ghisellini G., Padovani P., Celotti A., Maraschi L., 1993, ApJ, 407, 65
Ghosh P., Lamb F. K., 1978, ApJ, 223, L83
Ghosh P., Lamb F. K., 1979a, ApJ, 232, 259
Ghosh P., Lamb F. K., 1979b, ApJ, 234, 296
Ghosh P., Pethick C. J., Lamb F. K., 1977, ApJ, 217, 578
Giacconi R., Kellogg E., Gorenstein P., Gursky H., Tananbaum H., 1971, ApJ, 165, L27
Gierliński M., Done C., 2004, MNRAS, 347, 885
Gierliński M., Poutanen J., 2005, MNRAS, 359, 1261
Gierliński M., Zdziarski A. A., Poutanen J., Coppi P. S., Ebisawa K., Johnson W. N., 1999, MNRAS, 309, 496
Gierliński M., Done C., Barret D., 2002, MNRAS, 331, 141
Gierliński M., Middleton M., Ward M., Done C., 2008, Nature, 455, 369
Gilfanov M., Revnivtsev M., Sunyaev R., Churazov E., 1998, A&A, 338, L83
Gilfanov M., Grimm H.-J., Sunyaev R., 2004, MNRAS, 347, L57
Gladstone J. C., Roberts T. P., Done C., 2009, MNRAS, 397, 1836
Godet O., Barret D., Webb N. A., Farrell S. A., Gehrels N., 2009, ApJ, 705, L109
Godet O., Barret D., Webb N., Farrell S., 2010, ATEL, 2821, 1
Godet O., Farrell S., Barret D., Webb N., Servillat M., 2011, ATEL, 3569, 1
Grimm H.-J., Gilfanov M., Sunyaev R., 2002, A&A, 391, 923
Grimm H.-J., Gilfanov M., Sunyaev R., 2003, MNRAS, 339, 793
Grisé F., Kaaret P., Feng H., Kajava J. J. E., Farrell S. A., 2010, ApJ, 724, L148
Gruber D. E., Blanco P. R., Heindl W. A., Pelling M. R., Rothschild R. E., Hink P. L., 1996, A&AS, 120, C641
Haardt F., Maraschi L., Ghisellini G., 1994, ApJ, 432, L95
Haensel P., Potekhin A. Y., Yakovlev D. G., 2007, Astrophysics and Space Science Library Vol. 326, Neutron Stars 1: Equation of State and Structure, Springer, New York
Hartman J. M., et al., 2008, ApJ, 675, 1468
Hartman J. M., Patruno A., Chakrabarty D., Markwardt C. B., Morgan E. H., van der Klis M., Wijnands R., 2009, ApJ, 702, 1673
Heil L. M., Vaughan S., Roberts T. P., 2009, MNRAS, 397, 1061
Hewish A., Bell S. J., Pilkington J. D. H., Scott P. F., Collins R. A., 1968, Nature, 217, 709
Ibragimov A., Poutanen J., 2009, MNRAS, 400, 492
Ibragimov A., Kajava J. J. E., Poutanen J., 2011, MNRAS, 415, 1864
Illarionov A. F., Sunyaev R. A., 1975, A&A, 39, 185
Immler S., Lewin W. H. G., 2003, in Lecture Notes in Physics Vol. 598, Weiler K. ed., Supernovae and Gamma-Ray Bursters, Berlin Springer Verlag, p. 91
Impiombato D., Zampieri L., Falomo R., Grisé F., Soria R., 2011, Astron. Nachr., 332, 375
Jahoda K., Markwardt C. B., Radeva Y., Rots A. H., Stark M. J., Swank J. H., Strohmayer T. E., Zhang W., 2006, ApJS, 163, 401

Jansen F., et al., 2001, A&A, 365, L1
Jin J., Feng H., Kaaret P., 2010, ApJ, 716, 181
Jin J., Feng H., Kaaret P., Zhang S.-N., 2011, ApJ, 737, 87
Kaaret P., Corbel S., 2009, ApJ, 697, 950
Kaaret P., Prestwich A. H., Zezas A., Murray S. S., Kim D.-W., Kilgard R. E., Schlegel E. M., Ward M. J., 2001, MNRAS, 321, L29
Kaaret P., Corbel S., Prestwich A. H., Zezas A., 2003, Science, 299, 365
Kaaret P., Alonso-Herrero A., Gallagher J. S., Fabbiano G., Zezas A., Rieke M. J., 2004, MNRAS
Kaaret P., Ward M. J., Zezas A., 2004, MNRAS, 351, 83
Kajava J. J. E., Poutanen J., 2008, in M. Axelsson ed., AIP Conf. Ser. 1054, p. 39
Kajava J. J. E., Poutanen J., 2009, MNRAS, 398, 1450
Kajava J. J. E., Ibragimov A., Annala M., Patruno A., Poutanen J., 2011, MNRAS, 417, 1454
Kajava J. J. E., Poutanen J., Farrell S. A., Grisé F., Kaaret P., 2012, MNRAS, 422, 990
Karachentsev I. D., et al., 2002, A&A, 383, 125
King A. R., 2009, MNRAS, 393, L41
King A. R., Davies M. B., Ward M. J., Fabbiano G., Elvis M., 2001, ApJ, 552, L109
Komossa S., Schulz H., 1998, A&A, 339, 345
Kong A. K. H., 2011, ATEL, 3564, 1
Kong A. K. H., Yang Y. J., Hsieh P.-Y., Mak D. S. Y., Pun C. S. J., 2007, ApJ, 671, 349
Körding E., Falcke H., Markoff S., 2002, A&A, 382, L13
Körding E. G., Migliari S., Fender R., Belloni T., Knigge C., McHardy I., 2007, MNRAS, 380, 301
Kramer M., et al., 2006, Science, 314, 97
Krolik J. H., Hawley J. F., Hirose S., 2005, ApJ, 622, 1008
Kubota A., Mizuno T., Makishima K., Fukazawa Y., Kotoku J., Ohnishi T., Tashiro M., 2001, ApJ, 547, L119
Lamb F. K., Pethick C. J., Pines D., 1973, ApJ, 184, 271
Lamb F. K., Boutloukos S., Van Wassenhove S., Chamberlain R. T., Lo K. H., Clare A., Yu W., Miller M. C., 2009, ApJ, 706, 417
Lattimer J. M., Prakash M., 2001, ApJ, 550, 426
Lattimer J. M., Prakash M., 2007, Phys. Rep., 442, 109
Leahy D. A., Morsink S. M., Cadeau C., 2008, ApJ, 672, 1119
Leahy D. A., Morsink S. M., Chung Y.-Y., Chou Y., 2009, ApJ, 691, 1235
Leahy D. A., Morsink S. M., Chou Y., 2011, ApJ, 742, 17
Lehmann I., et al., 2005, A&A, 431, 847
Levine A. M., Bradt H., Cui W., Jernigan J. G., Morgan E. H., Remillard R., Shirey R. E., Smith D. A., 1996, ApJ, 469, L33
Li J., Wickramasinghe D. T., 1998, MNRAS, 300, 1015
Liu J., 2011, ApJS, 192, 10
Liu J.-F., Bregman J. N., 2005, ApJS, 157, 59
Liu J., Bregman J. N., McClintock J. E., 2009, ApJ, 690, L39
Long K. S., van Speybroeck L. P., 1983, in Accretion-Driven Stellar X-ray Sources, Lewin W. H. G., van den Heuvel E. P. J., eds., Cambridge Univ. Press, Cambridge and New York, p. 117
Long M., Romanova M. M., Lovelace R. V. E., 2005, ApJ, 634, 1214

Lovelace R. V. E., Romanova M. M., Bisnovatyi-Kogan G. S., 1995, MNRAS, 275, 244
Madau P., Rees M. J., 2001, ApJ, 551, L27
Malzac J., Belmont R., 2009, MNRAS, 392, 570
Mapelli M., Ripamonti E., Zampieri L., Colpi M., 2011, MNRAS, 416, 1756
Markwardt C. B., Strohmayer T. E., 2010, ApJ, 717, L149
Mason K. O., et al., 2001, A&A, 365, L36
McClintock J. E., Remillard R. A., 2006, in Compact stellar X-ray sources, Lewin W. H. G. & van der Klis M. eds., Cambridge Univ. Press, Cambridge, p. 157
McHardy I. M., Koerding E., Knigge C., Uttley P., Fender R. P., 2006, Nature, 444, 730
Medvedev A., Fabrika S., 2010, MNRAS, 402, 479
Merloni A., Fabian A. C., Ross R. R., 2000, MNRAS, 313, 193
Middleton M. J., Sutton A. D., Roberts T. P., 2011, MNRAS, 417, 464
Miller J. M., Fabbiano G., Miller M. C., Fabian A. C., 2003, ApJ, 585, L37
Miller J. M., Fabian A. C., Miller M. C., 2004, ApJ, 607, 931
Miller J. M., Homan J., Steeghs D., Rupen M., Hunstead R. W., Wijnands R., Charles P. A., Fabian A. C., 2006, ApJ, 653, 525
Miller M. C., Lamb F. K., 1998, ApJ, 499, L37
Mineo S., Gilfanov M., Sunyaev R., 2012, MNRAS, 419, 2095
Mineshige S., Hirano A., Kitamoto S., Yamada T. T., Fukue J., 1994, ApJ, 426, 308
Misner C. W., Thorne K. S., Wheeler J. A., 1973, Gravitation, W.H. Freeman and Co., San Francisco
Mitsuda K., et al., 1984, PASJ, 36, 741
Morsink S. M., Leahy D. A., 2011, ApJ, 726, 56
Morsink S. M., Leahy D. A., Cadeau C., Braga J., 2007, ApJ, 663, 1244
Murray S. S., et al., 2000, in J. E. Truemper & B. Aschenbach eds., Proc. SPIE, 4012, p. 68
Naso L., Miller J. C., 2010, A&A, 521, A31
Naso L., Miller J. C., 2011, A&A, 531, A163
Ng C., Díaz Trigo M., Cadolle Bel M., Migliari S., 2010, A&A, 522, A96
Okada K., Dotani T., Makishima K., Mitsuda K., Mihara T., 1998, PASJ, 50, 25
Oppenheimer J. R., Volkoff G. M., 1939, Phys. Rev., 55, 374
Paczyński B., Wiita P. J., 1980, A&A, 88, 23
Pakull M. W., Mirioni L., 2002, arXiv:astro-ph/0202488
Pakull M. W., Mirioni L., 2003, in J. Arthur & W. J. Henney eds., Revista Mexicana de Astronomia y Astrofisica, 15, p. 197
Papitto A., di Salvo T., Burderi L., Menna M. T., Lavagetto G., Riggio A., 2007, MNRAS, 375, 971
Papitto A., Di Salvo T., D'Aì A., Iaria R., Burderi L., Riggio A., Menna M. T., Robba N. R., 2009, A&A, 493, L39
Papitto A., et al., 2012, MNRAS, 423, 1178
Patruno A., Zampieri L., 2010, MNRAS, 403, L69
Patruno A., Watts A. L., 2012, arXiv:1206.2727
Patruno A., Rea N., Altamirano D., Linares M., Wijnands R., van der Klis M., 2009a, MNRAS, 396, L51
Patruno A., Wijnands R., van der Klis M., 2009b, ApJ, 698, L60
Patruno A., Bult P., Gopakumar A., Hartman J. M., Wijnands R., van der Klis M., Chakrabarty D., 2012, ApJ, 746, L27

Perna R., Soria R., Pooley D., Stella L., 2008, MNRAS, 384, 1638
Portegies Zwart S. F., Baumgardt H., Hut P., Makino J., McMillan S. L. W., 2004, Nature, 428, 724
Poutanen J., 2008, in R. Wijnands, D. Altamirano, P. Soleri, N. Degenaar, N. Rea, P. Casella, A. Patruno, & M. Linares eds., AIP Conf. Ser. 1068, p. 77
Poutanen J., Svensson R., 1996, ApJ, 470, 249
Poutanen J., Gierliński M., 2003, MNRAS, 343, 1301
Poutanen J., Beloborodov A. M., 2006, MNRAS, 373, 836
Poutanen J., Vurm I., 2009, ApJ, 690, L97
Poutanen J., Lipunova G., Fabrika S., Butkevich A. G., Abolmasov P., 2007, MNRAS, 377, 1187
Poutanen J., Ibragimov A., Annala M., 2009, ApJ, 706, L129
Prestwich A. H. et al. 2007, ApJ, 669, L21
Pringle J. E., Rees M. J., 1972, A&A, 21, 1
Psaltis D., Chakrabarty D., 1999, ApJ, 521, 332
Ptak A., Colbert E., van der Marel R. P., Roye E., Heckman T., Towne B., 2006, ApJS, 166, 154
Rappaport S. A., Fregeau J. M., Spruit H., 2004, ApJ, 606, 436
Reis R. C., et al., 2011, MNRAS, 410, 2497
Reynolds C. S., Loan A. J., Fabian A. C., Makishima K., Brandt W. N., Mizuno T., 1997, MNRAS, 286, 349
Riggio A., Di Salvo T., Burderi L., Menna M. T., Papitto A., Iaria R., Lavagetto G., 2008, ApJ, 678, 1273
Roberts T. P., Kilgard R. E., Warwick R. S., Goad M. R., Ward M. J., 2006, MNRAS, 371, 1877
Roberts T. P., Gladstone J. C., Goulding A. D., Swinbank A. M., Ward M. J., Goad M. R., Levan A. J., 2011, Astron. Nachr., 332, 398
Romanova M. M., Ustyugova G. V., Koldoba A. V., Lovelace R. V. E., 2002, ApJ, 578, 420
Romanova M. M., Ustyugova G. V., Koldoba A. V., Lovelace R. V. E., 2004, ApJ, 610, 920
Roming P. W. A., et al., 2004, in K. A. Flanagan & O. H. W. Siegmund eds., Proc. SPIE, 5165, p. 262
Rothschild R. E., et al., 1998, ApJ, 496, 538
Servillat M., Farrell S. A., Lin D., Godet O., Barret D., Webb N. A., 2011, ApJ, 743, 6
Shakura N. I., Sunyaev R. A., 1973, A&A, 24, 337
Shaposhnikov N., Jahoda K., Markwardt C., Swank J., Strohmayer T., 2012, ApJ, 757, 159
Shimura T., Takahara F., 1995, ApJ, 445, 780
Silverman J. M., Filippenko A. V., 2008, ApJ, 678, L17
Simon J. B., Hawley J. F., Beckwith K., 2011, ApJ, 730, 94
Soria R., 2007, Ap&SS, 311, 213
Soria R., Motch C., Read A. M., Stevens I. R., 2004, A&A, 423, 955
Soria R., Hau G. K. T., Graham A. W., Kong A. K. H., Kuin N. P. M., Li I.-H., Liu J.-F., Wu K., 2010, MNRAS, 405, 870
Soria R., Hakala P. J., Hau G. K. T., Gladstone J. C., Kong A. K. H., 2012, MNRAS, 420, 3599

Staelin D. H., Reifenstein III E. C., 1968, Science, 162, 1481
Stobbart A.-M., Roberts T. P., Warwick R. S., 2004, MNRAS, 351, 1063
Stobbart A.-M., Roberts T. P., Wilms J., 2006, MNRAS, 368, 397
Strohmayer T. E., 2009, ApJ, 706, L210
Strohmayer T. E., Mushotzky R. F., 2003, ApJ, 586, L61
Strohmayer T. E., Mushotzky R. F., 2009, ApJ, 703, 1386
Strohmayer T. E., Zhang W., Swank J. H., Smale A., Titarchuk L., Day C., Lee U., 1996, ApJ, 469, L9
Strohmayer T. E., Mushotzky R. F., Winter L., Soria R., Uttley P., Cropper M., 2007, ApJ, 660, 580
Strüder L., et al., 2001, A&A, 365, L18
Suleimanov V., Poutanen J., Revnivtsev M., Werner K., 2011, ApJ, 742, 122
Sunyaev R. A., Titarchuk L. G., 1985, A&A, 143, 374
Swartz D. A., Soria R., Tennant A. F., Yukita M., 2011, ApJ, 741, 49
Swartz D. A., Ghosh K. K., Tennant A. F., Wu K., 2004, ApJS, 154, 519
Swartz D. A., Tennant A. F., Soria R., 2009, ApJ, 703, 159
Tao L., Feng H., Grisé F., Kaaret P., 2011, ApJ, 737, 81
Tauris T. M., 2012, Science, 335, 561
Thorne K. S., 1994, Black holes and time warps: Einstein's outrageous legacy, Commonwealth fund book program, New York
Tolman R. C., 1939, Physical Review, 55, 364
Trudolyubov S. P., 2008, MNRAS, 387, L36
Turner M. J. L., et al., 2001, A&A, 365, L27
Uzdensky D. A., 2004, Ap&SS, 292, 573
Uzdensky D. A., Königl A., Litwin C., 2002a, ApJ, 565, 1191
Uzdensky D. A., Königl A., Litwin C., 2002b, ApJ, 565, 1205
van der Klis M., 2000, ARA&A, 38, 717
van der Klis M., Swank J. H., Zhang W., Jahoda K., Morgan E. H., Lewin W. H. G., Vaughan B., van Paradijs J., 1996, ApJ, 469, L1
Veledina A., Vurm I., Poutanen J., 2011, MNRAS, 414, 3330
Vierdayanti K., Done C., Roberts T. P., Mineshige S., 2010, MNRAS, 403, 1206
Viironen K., Poutanen J., 2004, A&A, 426, 985
Vikhlinin A., et al., 1994, ApJ, 424, 395
Walton D. J., Roberts T. P., Mateos S., Heard V., 2011, MNRAS, 416, 1844
Wang Y.-M., 1987, A&A, 183, 257
Warner B., 1995, Cataclysmic variable stars, Cambridge Astrophysics Series 28, Cambridge Univ. Press, Cambridge
Weisskopf M. C., Brinkman B., Canizares C., Garmire G., Murray S., Van Speybroeck L. P., 2002, PASP, 114, 1
Wiersema K., Farrell S. A., Webb N. A., Servillat M., Maccarone T. J., Barret D., Godet O., 2010, ApJ, 721, L102
Wijnands R., 2006a, in Trends in Pulsar Research, J. A. Lowry ed., p. 53
Wijnands R., 2006b, Adv. in Space Res., 38, 2684
Wijnands R., van der Klis M., 1998, Nature, 394, 344
Wolter H., 1952a, Annalen der Physik, 445, 94
Wolter H., 1952b, Annalen der Physik, 445, 286
Zampieri L., Mucciarelli P., Falomo R., Kaaret P., Di Stefano R., Turolla R., Chieregato

M., Treves A., 2004, ApJ, 603, 523
Zampieri L., Impiombato D., Falomo R., Grisé F., Soria R., 2012, MNRAS, 419, 1331
Zdziarski A. A., Lubiński P., Smith D. A., 1999, MNRAS, 303, L11
Zdziarski A. A., Poutanen J., Paciesas W. S., Wen L., 2002, ApJ, 578, 357
Zdziarski A. A., Lubiński P., Gilfanov M., Revnivtsev M., 2003, MNRAS, 342, 355

ISBN 978-952-62-0027-9
ISBN 978-952-62-0028-6 (PDF)
ISSN 1239-4327